High Precision Measurement of the ^{19}Ne Lifetime

by

Leah Jacklyn Broussard

Department of Physics
Duke University

Date: _____

Approved:

_____
Albert Young

_____
Calvin Howell

_____
Kate Scholberg

_____
Berndt Mueller

_____
John Thomas

Dissertation submitted in partial fulfillment of the requirements for the degree of
Doctor of Philosophy in the Department of Physics
in the Graduate School of Duke University
2012

Abstract

(Nuclear physics)

High Precision Measurement of the ^{19}Ne Lifetime

by

Leah Jacklyn Broussard

Department of Physics
Duke University

Date: _____

Approved:

_____
Albert Young

_____
Calvin Howell

_____
Kate Scholberg

_____
Berndt Mueller

_____
John Thomas

An abstract of a dissertation submitted in partial fulfillment of the requirements for the degree of Doctor of Philosophy in the Department of Physics in the Graduate School of Duke University
2012

Abstract

The lifetime of ^{19}Ne is an important parameter in precision tests of the Standard Model. Improvement in the uncertainty of experimental observables of this and other $T = \frac{1}{2}$ mirror isotopes would allow for an extraction of V_{ud} at a similar precision to that obtained by superallowed $0^+ \rightarrow 0^+$ Fermi decays. We report on a new high precision measurement of the lifetime of ^{19}Ne, performed at the Kernfysich Versneller Instituut (KVI) in Groningen, the Netherlands. A 10.5 $\frac{MeV}{A}$ ^{19}F beam was used to produce ^{19}Ne using inverse reaction kinematics in a H_2 gas target. Contaminant productions were eliminated using the TRIμP magnetic isotope separator. The ^{19}Ne beam was implanted into a thick aluminum tape, which was translated to a shielded detection region by a custom tape drive system. Collinear annihilation radiation from the emitted decay positrons were detected by two high purity germanium (HPGe) detectors. Event pulse waveforms were digitized and stored using a CAEN V1724 Digitizer. Systematic studies were performed to characterize rate-dependent data acquisition effects, diffusion, backgrounds, and contamination from the separator. We have obtained the result for the lifetime of $\tau = 24.9344 \pm 0.0073(stat) \pm 0.0083(sys)$ seconds.

Contents

List of Tables

List of Figures

Acknowledgements

I would like to thank the many people who made this work possible. First, I would like to thank my advisor, Albert Young, for the countless discussions and debates on seemingly impossible problems, for keeping me from getting lost in the finer details, and for pushing me to take on bigger challenges than I thought I could handle. I know that I am a better physicist today because you demanded it. I would also like to thank my co-advisor Calvin Howell, whose uncanny knack for seeing to the heart of the problem and careful attention to detail was more than welcome during this project's most difficult challenges.

I am grateful to everyone who helped to pull this project together. Robby Pattie Jr. was an essential part of this project, not only because of the countless hours spent on developing the data acquisition system, but also because he made sure I occasionally got out of the lab to enjoy Europe. I was able to sleep at night during shift-taking knowing that the experiment was in good hands. I also must thank Henning Back for his many contributions to this project, but especially for taking me under his wing when I was first getting started and hopelessly lost. Melissa Boswell paved the way for this project with her early work on the gas target and even returned to help take shifts during the measurement. Alex Crowell had many useful insights into our myriad of computing problems, and graciously performed many thankless tasks. I have the great pleasure of thanking my dear friend Mary Kidd, who worked shifts even though she was not a part of the project, and almost

certainly kept me from going insane.

I owe many thanks to the TUNL technical staff, especially Bret Carlin, John Dunham, Patrick Mulkey, and Richard O'Quinn, not only for their work creating a very snazzy tape drive interface, but for their cheerful guidance throughout the development of the project. I also want to thank Matthew Busch for his tremendous improvements to the tape drive system. On the other side of the globe, I am grateful to the many people at KVI who pushed to make this project happen. I appreciate the patience and professional guidance of Klaus Jungmann, Hans Wilschut, Lorenz Willmann, and Gerco Onderwater. Leo Huisman was infinitely helpful in the lab and is certainly the most pleasant person I have ever met. I want to thank the many students at KVI who signed up for shifts, especially Emil Traykov, Andrei Rogachevskiy, Moslem Sohani, and Praveen Shidling.

Introduction

The weak interaction in the Standard Model has already been extremely successful in its predictions. We can continue to refine the model by performing high precision tests of its assumptions. From studies of angular correlation measurements and lifetimes in beta decay, we can extract the ratio of the axial vector coupling to the vector coupling $\frac{g_A}{g_V}$ and the Cabibbo-Kobayashi-Maskawa mixing element V_{ud}.

The mixed, $\frac{1}{2}^+ \rightarrow \frac{1}{2}^+$ decay of ^{19}Ne to ^{19}F has been previously identified as an excellent candidate for these kinds of studies, as its small theoretical corrections and small experimental inputs such as the branching ratios and the angular correlation beta asymmetry allow us to access high precision more easily. The most precise measurements of the lifetime of the transition and the beta asymmetry were obtained from a series of experiments performed over the past several decades at Princeton under the direction of Frank Calaprice. Currently, the lifetime is a major contribution to the uncertainty in attempts to constrain matrix elements.

With the recent recalculation of all theoretical inputs to the $T = \frac{1}{2}$ mirror transitions, there is now a strong motivation to achieve a high precision result for the lifetime of ^{19}Ne. With significant improvement in the uncertainty of the lifetime and the beta asymmetry, the ^{19}Ne system can achieve the same precision of extraction of V_{ud} as superallowed $0^+ \rightarrow 0^+$ Fermi decays.

In this dissertation, I describe our experiment to measure the lifetime to the highest precision ever achieved. First, I review the state of the current theory and discuss

previous measurements using the ^{19}Ne system in Chapter 1. Then, in Chapter 2, I discuss the tape drive system, detectors, and data acquisition system. Chapter 3 covers the production of ^{19}Ne and elimination of contaminants in the separator. I review the analysis method, systematic effects, and their corrections in Chapter 4. Finally, the final result and its implications are presented in Chapter 5.

Because this measurement was the work of a collaboration between members of TUNL and the Kernfysich Versneller Instituut, it may be helpful to highlight my personal contributions to the experiment. I joined the project at its very early stages in 2005, and have been intimately involved with all facets since then. I performed the initial simulations of the TRIμP separator, participated in the first measurement of reaction products in late 2005, and analyzed the results for identification of observed particles and ^{19}Ne production rate estimates. I was responsible for the design, assembly, and testing of the prototype tape drive system and run programs, and aided in the design of the upgraded version. I co-developed the data acquisition system, including the custom components of the software (based on MIDAS). I was responsible for the preparation of the experimental apparatus ahead of each measurement, and developed and led the implementation of a data taking procedure to measure all relevant systematics and meet the statistical goals. Finally, I was solely responsible for building the completely custom analysis engine, and formulating the analysis strategy.

1

Motivation

To motivate the need for a new high-precision result for the lifetime of ^{19}Ne, we first must understand the questions that still remain in the very successful Standard Model. To that end, it is useful to review the relevant theory in the frame of precision studies using superallowed nuclear beta decay systems. Here, our goal is to outline some of the current tests of the Standard Model and proposed extensions, and demonstrate the viability of the ^{19}Ne decay system to push experimental limits of the model.

1.1 Theoretical Background

1.1.1 Weak interaction

In our current understanding, the weak interaction describes the interaction of the charged currents, mediated by the $W^{\pm}$ bosons, or neutral currents, mediated by the Z boson. An example of the charged weak interaction is the semileptonic transition of quarks. We can express the interaction of a charged weak hadronic current J^{μ}_{had}

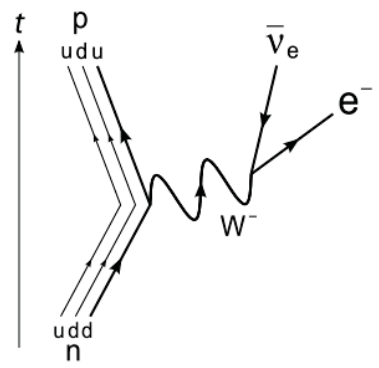

FIGURE 1.1: Feynman diagram for the quark transition $d \to u + e + \bar{\nu_e}$ in neutron decay.

and leptonic current J^{μ}_{lep} as

$$H = \frac{G_F}{\sqrt{2}} J^{\mu\dagger}_{lep} J_{\mu,had} \tag{1.1a}$$

$$J^{\mu}_{lep} = \bar{e}\gamma^{\mu}(1-\gamma_5)\nu_e \tag{1.1b}$$

$$J^{\mu}_{had} = V_{ud}\bar{u}\gamma^{\mu}(1-\gamma_5)d. \tag{1.1c}$$

The currents have the maximally parity-violating V-A form. The Feynman diagram for the quark transition $d \to u + e + \bar{\nu_e}$ is given in Fig. 1.1.

The quark eigenstates of the weak interaction are not the same as the mass eigenstates. The weak eigenstates include 3 generations of left-handed quark and corresponding leptonic doublets,

$$\begin{pmatrix} \nu_e \\ d' \end{pmatrix}_L, \qquad \begin{pmatrix} c \\ s' \end{pmatrix}_L, \qquad \begin{pmatrix} t \\ b' \end{pmatrix}_L, \tag{1.2a}$$

$$\begin{pmatrix} \nu_e \\ e \end{pmatrix}_L, \qquad \begin{pmatrix} \nu_\mu \\ \mu \end{pmatrix}_L, \qquad \begin{pmatrix} \nu_\tau \\ \tau \end{pmatrix}_L. \tag{1.2b}$$

The coefficient V_{ud} is the matrix element governing u↔d transitions in the quark-flavor mixing matrix, the Cabibbo-Kobayashi-Maskawa (CKM) matrix.

$$\begin{pmatrix} d' \\ s' \\ b' \end{pmatrix} = \begin{pmatrix} V_{ud} & V_{us} & V_{ub} \\ V_{cd} & V_{cs} & V_{cb} \\ V_{td} & V_{ts} & V_{tb} \end{pmatrix} \begin{pmatrix} d \\ s \\ b \end{pmatrix}. \tag{1.3}$$

1.1.2 Nuclear beta decay

Moving from quark decay to nuclear beta decay requires consideration of the perturbations from the strong force. The resulting form of the hadronic current must have vector or axial vector contributions, which can be constructed from the baryon spinors, the momentum transfer $\mathbf{q} = \mathbf{p_i} - \mathbf{p_f}$, and the γ matrices[24]. The only independent vectors and axial vectors that can be formed are shown in Eq. 1.4.

$$\langle B'|V^\alpha|B\rangle = \begin{cases} \bar{u}(B')\gamma^\alpha u(B) \\ \bar{u}(B')\sigma^{\alpha\nu}q_\nu u(B) \\ \bar{u}(B')u(B)q^\alpha \end{cases} \tag{1.4a}$$

$$\langle B'|A^\alpha|B\rangle = \begin{cases} \bar{u}(B')\gamma^\alpha\gamma_5 u(B) \\ \bar{u}(B')\sigma^{\alpha\nu}q_\nu\gamma_5 u(B) \\ \bar{u}(B')\gamma_5 u(B)q^\alpha \end{cases} \tag{1.4b}$$

A completely general Lorentz-invariant interaction is therefore

$$\langle B'|J^\alpha|B\rangle = V_{ij}\bar{u}(B')\big[\left(f_1(q^2)\gamma^\alpha + if_2(q^2)\sigma^{\alpha\nu}q_\nu + f_3(q^2)q^\alpha\right) - \left(g_1(q^2)\gamma^\alpha\gamma_5 + ig_2(q^2)\sigma^{\alpha\nu}q_\nu\gamma_5 + g_3(q^2)\gamma_5 q^\alpha\right)\big], \tag{1.5}$$

where the form factors $f_{1,2,3}$ and $g_{1,2,3}$ can only be a function of the kinematic scalar, q^2. There are some predictions for the values of the induced form factors. The Conserved Vector Current (CVC) hypothesis states that the polar vector component of the charged weak currents $V_\mu^{W\pm}$ (Eq. 1.4a) and the electromagnetic current, J_μ^{EM} form components of an isospin current. Given an isospin doublet which satisfies the Dirac equation,

$$\Psi = \begin{pmatrix} p \\ n \end{pmatrix}, \tag{1.6}$$

and the isospin matrices,

$$\tau_1 = \begin{pmatrix} 0 & 1 \\ 1 & 0 \end{pmatrix}, \qquad \tau_2 = \begin{pmatrix} 0 & -i \\ i & 0 \end{pmatrix}, \qquad \tau_3 = \begin{pmatrix} 1 & 0 \\ 0 & -1 \end{pmatrix}, \tag{1.7}$$

the current

$$J_\mu = \frac{1}{2}\bar{\Psi}\gamma_\mu\tau\Psi. \tag{1.8}$$

must be conserved. Noting that the electromagnetic and weak vector currents can be expressed as

$$J_\mu^{EM} = \frac{1}{2}\bar{\Psi}\gamma_\mu(1+\tau_3)\Psi, \tag{1.9a}$$

$$V_\mu^{W_\pm} = \frac{1}{2}\bar{\Psi}\gamma_\mu(\tau_1 \pm i\tau_2)\Psi, \tag{1.9b}$$

we can relate the isovector component of J_μ^{EM} and the polar vector part of the charged weak currents to an isospin current I_μ identical to Eq 1.8. This realization allows us to equate the form factors of $V_\mu^{W_\pm}$ to the form factors of the isovector part of J_μ^{EM}. The electromagnetic current can be expressed as

$$J_\mu^{EM} = \bar{u}\left[F_1(q^2)\gamma_\mu + iF_2(q^2)\sigma_{\mu\nu}q^\nu + F_3(q^2)q_\mu\right]u \tag{1.10a}$$

The conservation of the electromagnetic current, $\partial^\mu J_\mu^{EM} = 0$, requires that $F_3(q^2) = 0$. In the $q^2 \to 0$ limit, the form factors $F_1(0)$ and $F_2(0)$ are equated to the charge and anomalous magnetic moments. If we take the isovector components of the electromagnetic form factors, $F_{1,2,3}^V(q^2) = F_{1,2,3}^p(q^2) - F_{1,2,3}^n(q^2)$, we can produce a prediction for the weak form factors, $f_{1,2,3}$,

$$f_1(q^2) = F_1^V(q^2), \tag{1.11a}$$

$$f_2(q^2) = F_2^V(q^2), \tag{1.11b}$$

$$f_3(q^2) = 0. \tag{1.11c}$$

Therefore, CVC predicts that $g_V \equiv f_1(0) = 1$, that the "weak magnetism" term f_2 can be related to the magnetic moments of the initial and final states, and the induced scalar term f_3 vanishes.

Another prediction arises from consideration of the behavior of the form factors

under a G-parity transformation[84], which is a combination of the charge conjugation and an isospin rotation about the I_2 axis of π,

$$G = Ce^{i\pi I_2}. \tag{1.12}$$

Vector terms with G-parity $+1$ (f_1 and f_2) and axial-vector terms with G-parity -1 (g_1 and g_3) are termed "first-class" currents, and terms that transform oppositely, f_3 and g_2, are termed "second-class". As the f_3 and g_2 terms are induced by the strong force, a non-zero value has serious implications for the strong force, which is G-invariant.

Finally, the induced pseudoscalar term, g_3, is negligible in nonrelativistic nuclear β-decay, in the limit that the pion mass $m_\pi \to 0$, according to the Partially Conserved Axial Current (PCAC) hypothesis.

1.1.3 Superallowed decays

By considering a subset of nuclear beta decays in which the strong force-induced corrections are very small and well-understood, we can expose the fundamental parameters in the theory and perform high precision tests of the Standard Model. The superallowed transitions are characterized by selection rules related to the change in angular momentum and total isospin of the nuclei. Transitions in which the leptons carry away any orbital momentum are suppressed. In allowed transitions, $\mathbf{L} = 0$ and therefore parity must remain unchanged. Also, because the electron and neutrino are both spin $\frac{1}{2}$ particles, their total spin $\mathbf{S}$ must be 0 or 1. From the conservation of angular momentum in beta decay,

$$\mathbf{J} = \mathbf{L} + \mathbf{S}. \tag{1.13}$$

the nuclear spin $\mathbf{J}$ can only change by 0 or 1. The subset of "superallowed" decays are further encouraged. These are transitions between analog states, in which the total isospin $\mathbf{T}$ and configuration are the same.

Table 1.1: Selection rules for Fermi and Gamow-Teller decays.

Fermi		Gamow-Teller	
$\pi_i\pi_f$	$= +1$	$\pi_i\pi_f$	$= +1$
$\mathbf{J}_i$	$= \mathbf{J}_f$	$\mathbf{J}_i$	$= \begin{cases} \mathbf{J_f} & (\mathbf{J_f} \neq 0) \\ \mathbf{J_f} \pm 1 \end{cases}$
$\Delta\mathbf{T}$	$= 0$	$\Delta\mathbf{T}$	$= 0$

The nuclear beta decay transition amplitude can be expressed in the allowed approximation as

$$A_{fi} = \frac{G_F}{\sqrt{2}} V_{ud} \left[g_V M_F j_0(0) - g_A \mathbf{M_{GT}} \cdot \mathbf{j}(0) \right], \tag{1.14a}$$

$$M_F = \sum_{i=1}^{A} \int d^3\chi^{\dagger\prime}(\mathbf{x}) \tau_i^{\pm} \chi(\mathbf{x}), \tag{1.14b}$$

$$M_{GT} = \sum_{i=1}^{A} \int d^3\chi^{\dagger\prime}(\mathbf{x}) \boldsymbol{\sigma}_i \tau_i^{\pm} \chi(\mathbf{x}), \tag{1.14c}$$

where $\mathbf{j}_\mu$ are the components of the leptonic current, and we define $g_V = f_1(0)$ and $g_A = g_1(0)$. The interaction includes terms proportional to the matrix elements M_F and M_{GT}. The Fermi matrix element M_F does not allow for a change in nuclear spin $\mathbf{J}$, and the Gamow-Teller matrix element M_{GT} does not allow for a transition such that $\mathbf{J}_i = \mathbf{J}_f = 0$. These selection rules are summarized in Table 1.1.

From the amplitude of the transition, we can derive expressions which define our expectations for experimentally accessible terms. For example, from Fermi's golden rule, we obtain the transition probability

$$dW = (2\pi)^{-5} \delta(E_e + E_\nu - \Delta) |A_{fi}|^2 d^3\mathbf{p}_e d^3\mathbf{p}_\nu. \tag{1.15}$$

We must also include a correction factor F(Z,E) to correct the amplitude of the electron wavefunction,

$$|A_{fi}|^2 \to \frac{m_e}{E_e} \frac{m_\nu}{E_\nu} F(Z,E) |A_{fi}|^2. \tag{1.16}$$

By summing over final spins, we obtain the beta decay rate W of polarized nuclei, [44, 45],

$$d\omega = dE_e d\Omega_e d\Omega_\nu \frac{G_F^2 V_{ud}^2}{(2\pi)^5} F(\pm Z, E_e) p_e E_e (E_0 - E_e)^2 \xi$$
$$\times \left[\left(1 + a\frac{\mathbf{p_e} \cdot \mathbf{p}_\nu}{E_e E_\nu} + b\frac{m_e}{E_e} \right) + \frac{\mathbf{J}}{J} \cdot \left(A\frac{\mathbf{p_e}}{E_e} + B\frac{\mathbf{p}_\nu}{E_\nu} + D\frac{\mathbf{p_e} \times \mathbf{p}_\nu}{E_e E_\nu} \right) \right], \quad (1.17a)$$

$$\xi = (g_V^2 \mid M_F \mid^2 + g_A^2 \mid M_{GT} \mid^2). \quad (1.17b)$$

The half-life can be derived by integrating over the solid angles and energies of the neutrino and electron. The statistical rate function $f(Z, E_0)$ is defined to handle the integral over electron energy.

$$ft = f\frac{\ln 2}{\omega} = \frac{K}{(G_F V_{ud})^2 (g_V^2 \mid M_F \mid^2 + g_A^2 \mid M_{GT} \mid^2)} \quad (1.18a)$$

$$f(Z, E_0) = \frac{1}{m_e^5 c^7} \int F(\pm Z, E_e) p_e E_e (E^0 - E_e)^2 dE_e \quad (1.18b)$$

$$\frac{K}{(\hbar c)^6} = \frac{2\pi^3 \hbar \ln 2}{(m_e c^2)^5} \quad (1.18c)$$

In the event that there are multiple branches and/or an electron capture fraction P_{EC}, the partial half-life for the branch of interest can be extracted by making the correction

$$t = \ln 2 \tau \left(\frac{1 + P_{EC}}{BR} \right). \quad (1.19)$$

1.1.4 Theoretical corrections

Superallowed nuclear beta decays are subject to two classes of corrections: the radiative corrections and isospin symmetry-breaking corrections[74]. Radiative corrections originate from mostly undetected radiative processes. The "outer" radiative corrections δ_R depend on the nucleus, and "inner" radiative corrections Δ_R do

not. The nucleus-independent inner correction has recently been calculated to high precision[54],

$$\Delta_R = (2.361 \pm 0.038)\%, \tag{1.20}$$

but is still currently the limiting uncertainty in superallowed $0^+ \rightarrow 0^+$ beta decay. The outer correction δ_R has two components which are treated separately. The component δ'_R depends only on atomic charge Z and the maximum electron energy W_0. It is calculated from QED to the first three orders, α, $Z\alpha^2$, and $Z^2\alpha^3$, and includes the leading order log extrapolation of the low energy term in Δ_R, denoted δ_{α^2}, which is nucleus-dependent. The second component of δ_R requires a nuclear structure calculation, and is kept in δ_{NS}.

$$1 + RC = (1 + \delta'_R)(1 + \delta_{NS})(1 + \Delta_R) \tag{1.21a}$$

$$\delta'_R = \delta_1 + \delta_2 + \delta_3 + \delta_{\alpha^2} \tag{1.21b}$$

The isospin symmetry-breaking correction arises because isospin is not an exact symmetry in nuclei. The Fermi and Gamow-Teller matrix elements are subject to corrections

$$M_F^2 = |M_F^0|^2(1 - \delta_C^V), \tag{1.22a}$$

$$M_{GT}^2 = |M_{GT}^0|^2(1 - \delta_C^A). \tag{1.22b}$$

For Fermi transitions, δ_C^V can be precisely determined from calculations of the isospin Clebsch-Gordan coefficients. The correction can be split into two terms; δ_{C1}^V corrects for the charge-dependent configuration mixing, and δ_{C2}^V handles the difference between neutron and proton radial wave functions.

$$\delta_C^V = \delta_{C1}^V + \delta_{C1}^V. \tag{1.23}$$

With these considerations, we can write down an expression for the lifetime of a superallowed transition, noting that the statistical rate function f has different ex-

pressions for Fermi and Gamow-Teller transitions, f_V and f_A,

$$t = \frac{K}{G_F^2 V_{ud}^2} \frac{1}{(1+\delta_R')(F+GT)} \tag{1.24a}$$

$$F = f_V |M_F^0|^2 (1 + \delta_{NS}^V - \delta_C^V) g_V^2 (1 + \Delta_R^V) \tag{1.24b}$$

$$GT = f_A |M_{GT}^0|^2 (1 + \delta_{NS}^A - \delta_C^A) g_A^2 (1 + \Delta_R^A). \tag{1.24c}$$

If we define a mixing ratio,

$$\rho^2 = \frac{g_A^2 |M_{GT}^0|^2}{g_V^2 |M_F^0|^2} \frac{(1 + \delta_{NS}^A - \delta_C^A)(1 + \Delta_R^A)}{(1 + \delta_{NS}^V - \delta_C^V)(1 + \Delta_R^V)}, \tag{1.25a}$$

$$\approx \frac{g_A^2 |M_{GT}^0|^2}{g_V^2 |M_F^0|^2}, \tag{1.25b}$$

we can simplify the expression,

$$f_V t (1 + \delta_R')(1 + \delta_{NS}^V - \delta_C^V) = \frac{K}{G_F^2 V_{ud}^2} \frac{1}{|M_F^0|^2 g_V^2 (1 + \Delta_R^V)(1 + \frac{f_A}{f_V})\rho^2}. \tag{1.26}$$

This expression is usually referred to as the $\mathcal{F}$t value.

1.2 Tests of the Standard Model

1.2.1 CKM unitarity

Currently, there are many tests of the Standard Model and searches for new physics that are actively being pursued[73]. One of the most familiar to the general community is the status of the unitarity of the CKM matrix[31]. The most stringent test of unitarity is from the first row of the matrix,

$$V_{ud}^2 + V_{us}^2 + V_{ub}^2 = 1. \tag{1.27}$$

The element V_{ud} is the most accessible experimentally, as it contributes to all beta decays involving the u and d quarks. The most precise extraction of V_{ud} comes from the superallowed $0^+ \rightarrow 0^+$ Fermi decays[41]. The neutron and pion decay systems

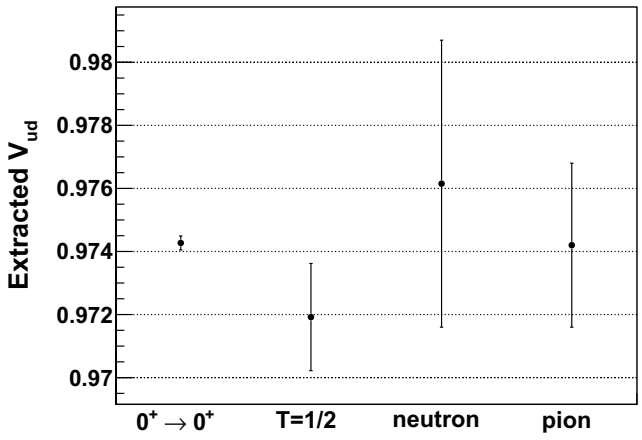

FIGURE 1.2: Results for the extraction of V_{ud} from independent decay systems.

provide independent checks at lower precision; however, some discrepancies in the experimental measurements of the lifetime of the neutron must still be resolved[81]. Recently, the class of superallowed $T = \frac{1}{2}$ mixed Fermi and Gamow-Teller decays have used to extract V_{ud} as well, with comparable precision to that of neutron decay[59]. The results for the extraction are shown in Fig. 1.2.

Using the currently recommended values by the Particle Data Group[30],

$$|V_{ud}| = 0.97425 \pm 0.00022, \tag{1.28a}$$

$$|V_{us}| = 0.2252 \pm 0.0009, \tag{1.28b}$$

$$|V_{ub}| = 0.230 \pm 0.011, \tag{1.28c}$$

we find that the sum in Eq. 1.27 is 0.9999 ± 0.0006, consistent with unitarity. A failure in unitarity would point to a gap in our understanding of physics in the Standard Model, and could indicate the existence of a new generation of fermions, non-V,A contributions, or new V,A contributions involving right-handed currents, due to possible right-handed charged bosons, exotic fermions with right-handed couplings to $W^{\pm}$, or leptoquark exchange[31].

1.2.2 CVC hypothesis

It is also possible to test the validity of the CVC hypothesis. The most precise test comes from the prediction that g_V is constant, and therefore, the $\mathcal{F}$t values for all superallowed transitions of a certain type must be constant. The superallowed $0^+ \to 0^+$ Fermi decays can be used to find an average $\mathcal{F}$t value of (3072.08 ± 0.79) s, with $\frac{\chi^2}{\nu} = 0.29$. This result verifies CVC at the 1.3×10^{-4} level[41]. The superallowed $T = \frac{1}{2}$ mixed Fermi and Gamow-Teller decays can also be used for this kind of test. A new verification of CVC was performed using the average $\mathcal{F}$t value of (6173 ± 22) s, with $\frac{\chi^2}{\nu} = 0.75$. CVC is verified using this system at the 3.6×10^{-4} level[59]. In addition, the presence of an induced scalar term f_3 affects the calculated statistical rate function f, with the most significant effect at low Z. A test of the curvature of the $\mathcal{F}$t values as a function of Z using $0^+ \to 0^+$ Fermi decays places a limit on the scalar term of $|f_S| \leq 0.0013$[40].

1.2.3 Left-Right symmetry

The left-handedness of the weak interaction is still not understood. The left-right symmetric models have been suggested as providing a mechanism for the observed parity violation[60, 56, 57, 71, 9]. The left-right symmetric model is based on a $SU(2)_L \times SU(2)_R \times U(1)$ gauge group, which introduces additional, predominantly weak bosons, denoted W_2 and Z_2, such that

$$W_L = W_1 \cos\zeta + W_2 \sin\zeta, \tag{1.29a}$$

$$W_R = e^{i\omega}(-W_1 \sin\zeta + W_2 \cos\zeta), \tag{1.29b}$$

where ζ is the mixing angle and ω is a CP-violating phase. The simplified limit of manifest left-right symmetry does not distinguish between possible left and right gauge coupling constants ($g_L = g_R$), quark mixing matrix elements ($V_{ud}^L = V_{ud}^R$), or the masses of left-handed and right-handed neutrinos, and also eliminates the

"extra" CP-violating phase ω. In this limit, the couplings from the generalized Hamiltonian[42]

$$H_{V,A} = \bar{e}\gamma_\lambda(C_V + C'_V\gamma_5)\nu\bar{p}\gamma_\lambda n - \bar{e}\gamma^\lambda\gamma_5(C_A + C'_A\gamma_5)\nu\bar{p}\gamma^\lambda\gamma_5 n \tag{1.30}$$

can be expressed as

$$C_V = \frac{G_F}{\sqrt{2}}V_{ud}g_V(1 - 2\zeta + \delta) \tag{1.31a}$$

$$C'_V = \frac{G_F}{\sqrt{2}}V_{ud}g_V(1 - \delta) \tag{1.31b}$$

$$C_A = \frac{G_F}{\sqrt{2}}V_{ud}g_A(1 + 2\zeta + \delta) \tag{1.31c}$$

$$C'_A = \frac{G_F}{\sqrt{2}}V_{ud}g_A(1 - \delta) \tag{1.31d}$$

where $\delta = \left(\frac{m_1}{m_2}\right)^2$ is the ratio of the masses of the W_1 and W_2 bosons.

In nuclear beta decay, limits can be placed on the values of ζ and δ from studies of the $\mathcal{F}$t values of superallowed $0^+ \rightarrow 0^+$ Fermi decays, the beta asymmetry parameter of mixed mirror transitions, angular correlations in neutron decay, and the longitudinal polarizations of betas emitted from polarized and unpolarized nuclei. While the limits on the mass of the right-handed boson are not competitive with results from proton-antiproton collisions or analysis of the charged and neutral sectors in the manifest left-right symmetric limit, the results are complementary in generalized theories.

Assuming the manifest symmetric model for now, the most precise limit on ζ from nuclear beta decay is obtained from the $\mathcal{F}$t values of superallowed $0^+ \rightarrow 0^+$ Fermi decays[80],

$$\mathcal{F}t = \frac{K}{2G_F^2V_{ud}^2(1 - 2\zeta)(1 + \Delta_R^V)}. \tag{1.32}$$

With the most up-to-date recommendations for the input parameters, and setting V_{ud} by assuming unitarity from V_{us} and V_{ub}, we find that

$$\zeta = 0.0001 \pm 0.0003. \tag{1.33}$$

One of the earliest attempts to constrain the left-right symmetric models using the beta-asymmetry parameter in $T = \frac{1}{2}$ systems was performed using the ^{19}Ne decay system[43], and the analysis was later extended for all $T = \frac{1}{2}$ transitions[58]. The quantities x and y are introduced, which are related to the ζ and δ parameters by

$$x = \frac{\delta(1+\tan\zeta) - \tan\zeta(1-\tan\zeta)}{1-\tan\zeta+\tan\zeta(1+\tan\zeta)} \approx \delta - \zeta, \tag{1.34a}$$

$$y = \frac{\delta(1-\tan\zeta) + \tan\zeta(1+\tan\zeta)}{1+\tan\zeta-\tan\zeta(1-\tan\zeta)} \approx \delta + \zeta, \tag{1.34b}$$

where the Standard Model requires $x = 0$ and $y = 0$. In this parameterization, the zero-momentum limit of the beta asymmetry of a $T = \frac{1}{2}$ transition can be expressed as

$$A_\beta(0) = \pm 2\frac{g_A(g_A \pm g_V) - y g_A(y g_A \pm x g_V)}{g_V^2 + 3g_A^2 + (x^2 g_V^2 + 3y^2 g_A^2)}. \tag{1.35}$$

The form factor g_A is eliminated by taking the ratio of the ft value of the transition to that of the $0^+ \to 0^+$ transitions.

$$R = \frac{\mathcal{F}t(0^+ \to 0^+)}{ft} = \frac{g_V^2 + 3g_A^2 + (x^2 g_V^2 + 3y^2 g_A^2)}{2(1+x^2)g_V^2} \tag{1.36}$$

The sensitivity of the mirror transitions to the parameters ζ and δ are explored by attempting to write the relations in the illuminating form

$$A_\beta(0) \approx A_0(1 + \alpha_{\delta\delta}\delta^2 + \alpha_{\zeta\delta}\zeta\delta + \alpha_{\zeta\zeta}\zeta^2), \tag{1.37a}$$

$$R \approx R_0(1 + \rho_{\delta\delta}\delta^2 + \rho_{\zeta\delta}\zeta\delta + \rho_{\zeta\zeta}\zeta^2). \tag{1.37b}$$

Examination of the matrix elements reveals that, to second order, R is only sensitive to the product $\zeta\delta$, and the coefficients in $A_\beta(0)$ can be expressed in terms of

$\alpha_{\zeta\zeta}$. Due to the very small beta asymmetry of the ^{19}Ne system, resulting from an accidental cancellation between form factors, this system is extremely sensitive to the $\alpha_{\zeta\zeta}$ parameter, as compared to other mirror transitions. Explicitly, for the ^{19}Ne system we can write

$$A_\beta(0) \approx 1 - 2\delta^2 + 48\zeta\delta + 24\zeta^2, \tag{1.38a}$$

$$R \approx \frac{1}{2Y^2}\left(1 + Y^2 + \delta\zeta\right) \tag{1.38b}$$

with Y as the mixing ratio $\frac{g_V M_F}{g_A M_{GT}}$. In order to obtain a limit competitive with current constraints from other systems, and sensitive to a right-handed boson mass of $300\frac{GeV}{c^2}$, an uncertainty of about 0.5% is needed on the experimental inputs.

In addition to these studies, the comparison of the beta asymmetry of mixed mirror transitions to pure Gamow-Teller transitions for a given isotope is sensitive to the products $\delta\zeta$ and ζ^2; but loses its sensitivity to right-handed currents in the limit of no mixing. Better experimental constraints similar to the $T = \frac{1}{2}$ case discussed previously are also required for competitive limits. The ratio of the longitudinal polarization of the emitted betas for pure Fermi and pure Gamow-Teller transitions with unpolarized nuclei is sensitive to the product $\delta\zeta$. The weighted average of these measurements results in a limit of $-4.0 < \delta\zeta \times 10^4 < 7.0$ at the 90% confidence level[16]. Better constraints come from studies of the asymmetry of the longitudinal polarization of the emitted betas compared to a polarized nucleus in pure Gamow-Teller of mixed $T = \frac{1}{2}$ transitions, which is sensitive to $(\delta + \zeta)^2$. Results from the beta asymmetries of ^{107}In, $(\delta + \zeta)^2 = 0.0021 \pm 0.0017$[72], ^{12}N, $(\delta + \zeta)^2 = -0.0005 \pm 0.0030$[79], and ^{21}Na, $(\delta + \zeta)^2 = 0.037 \pm 0.070$[69], are all in agreement. Finally, the beta asymmetry and neutrino asymmetry in neutron decay can be used to place sensitive limits on left-right symmetric models.

1.3 Status of the ^{19}Ne system

The superallowed $0^+ \rightarrow 0^+$ Fermi decays have already been measured to excellent precision, but there is not yet an independent system able to cross-check those results with the same precision. Severijns et al.[74] and Naviliat-Cuncic[59] have recently reviewed the status of $T = \frac{1}{2}$ systems, and have calculated the theoretical corrections required for precision tests of the Standard Model. The updated theoretical treatment demands higher precision experimental results. One of the most promising candidate systems is the ^{19}Ne $\frac{1}{2}^+ \rightarrow \frac{1}{2}^+$ decay to ^{19}F. The statistical rate function and nucleus-dependent corrections required to obtain the $\mathcal{F}t$ value and ultimately extract V_{ud} for the ^{19}Ne system are shown in Table 1.2.

The experimental inputs that have been identified as necessary for the precise extraction of the $\mathcal{F}t$ value of this system include the lifetime, the branching ratios and electron capture fraction, and the total transition energy. Currently, the uncertainty in the lifetime is the largest contribution to the overall uncertainty. In reviewing prior measurements of the lifetime (typically reported as a half-life), we follow the

Table 1.2: Theoretical corrections in ^{19}Ne system.

Correction	Value
f_V	98.532± 0.058
$\frac{f_A}{f_V}$	1.0143±0.0029
$\delta_1(\%)$	1.226
$\delta_2(\%)$	0.272
$\delta_3(\%)$	0.012
$\delta_{\alpha^2}(\%)$	0.022
$\delta'_R(\%)$	1.533±0.012
$\delta^V_{c1}(\%)$	0.140±0.030
$\delta^V_{c2}(\%)$	0.275±0.025
$\delta^V_{NS}(\%)$	-0.11±0.02
$\delta^V_C - \delta^V_{NS}(\%)$	0.52±0.04
Δ_R	2.361±0.038

lead of Severijns et al.[74] in considering only the measurements which produced results with an error bar up to 10 times higher than the most precise result, and rejecting the very strongly deviating results.

The least precise measurement considered was performed by Penning and Schmidt in 1957, in which the authors created ^{19}Ne by the (p,n) reaction on fluorine using a gaseous freon target[63]. Earwaker et al. improved the precision considerably with their experiment, which irradiated a MnF_3 with 4.8 MeV protons and counted the annihilation gammas in the 511 keV peak using a NaI detector[27]. Goss et al. used 5.5 MeV protons incident on a CeF_3 target to produce ^{19}Ne, and used two NaI detectors to count the annihilation radiation in coincidence[39]. Wilkinson and Alburger selected a BaF_2 target bombarded by 7 MeV protons for production, and counted the emitted betas in a plastic scintillator. This measurement was the first to perform a systematic check for diffusion, by epoxying a gold foil over the target[85]. The precision was considerably improved by Azuelos and Kitching, who used an LiF target irradiated with 13 MeV protons. These authors noted a small contaminant production of ^{15}O in their sample [6]. The most precise determination of ^{19}Ne was never published, and is the topic of a senior thesis at Princeton, in which a CaF_2 target was bombarded with 9 MeV protons. This experiment was the first to attempt to purify the produced ^{19}Ne using an isotope separator, and also included

Table 1.3: Previous ^{19}Ne half-life measurements.

Half-life (s)	Reference
17.7±0.1	[63]
17.43±0.06	[27]
17.36±0.06	[39]
17.36±0.06	[85]
17.219±.017	[6]
17.239±.010	[83]
17.237±.014	[64]

several studies to look for diffusion[83]. Finally, a more well-known, but somewhat less precise, result is from a Princeton doctoral dissertation[64]. The results from these measurements are summarized in Table 1.3.

In calculating the global average for the uncertainty, the statistical procedure typically used by the Particle Data Group is adopted[30]. The average and uncertainty $x_i \pm \delta x_i$ of the N independent measurements is given by

$$\overline{x} \pm \delta\overline{x} = \frac{\sum_i w_i x_i}{\sum_i w_i} \pm \left(\sum_i w_i \right)^{-\frac{1}{2}}, \tag{1.39a}$$

$$w_i = \frac{1}{(\delta x_i)^2}. \tag{1.39b}$$

The goodness of the fit is determined from the χ^2 test, where

$$\chi^2 = \sum_i \frac{(x_i - \overline{x})^2}{(\delta x)_i^2}. \tag{1.40}$$

is expected to be $\approx N$. If the fit is poor, the uncertainty from the weighted mean must be increased to account for the fact that the measurement uncertainties must have been underestimated. Quantitatively, if the scale factor S is greater than 1, where

$$S = \sqrt{\frac{\chi^2}{(N-1)}}, \tag{1.41}$$

then the uncertainties are scaled by a factor S. In the event that the uncertainties of the measurements differ greatly, only measurements for which

$$\delta x_i \lesssim 3\sqrt{N}\delta\overline{x} \tag{1.42}$$

holds are included in the calculation of S, as large uncertainties do not contribute to $\overline{x}$ and $\delta\overline{x}$ but can contribute significantly to S. Following this prescription, we can obtain the result for the half-life of ^{19}Ne of (17.244 $\pm$ 0.013) seconds (Fig. 1.3).

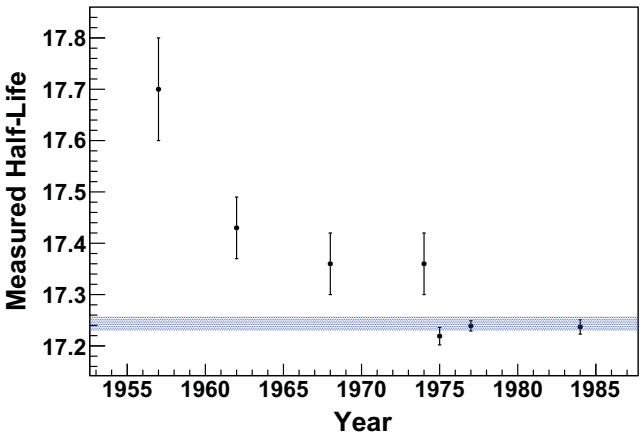

FIGURE 1.3: Measured half-lives of ^{19}Ne by previous experiments. The global average (shaded region) is (17.244 ± 0.013) seconds.

The 1957 result was excluded from the calculation of the scale factor S. There is presently an apparent discrepancy between recent results and those prior to 1975. We can compare this to the half-life used by Severijns[74] in their calculation of the $\mathcal{F}$t value, which does not include the Vitale measurement, of (17.248 ± 0.029) seconds. The uncertainty is a factor of two larger because of the increased scale factor without the Vitale measurement.

We are interested in the transition of ^{19}Ne to the ground state of ^{19}F, but there are two other small branches to the 110 keV and 1554 keV states (Fig. 1.4). Alburger used the (p,n) reaction to create ^{19}Ne, by bombarding CaF_2 and BaF_2 targets with protons, and measured the $\frac{1}{2}^+ \rightarrow \frac{3}{2}^+$ decay to the 1554 keV state of ^{19}F. A gamma-ray spectrum was produced with a Ge(Li) detector, and the branching ratio was determined by comparing the intensity of the 1357 keV gamma ray peak corresponding to the ^{19}F decay down to the 197 keV state, relative to the 511 keV annihilation peak[1]. To measure the $\frac{1}{2}^+ \rightarrow \frac{1}{2}^-$ branch to the 110 keV state of ^{19}F, ^{19}Ne was created by proton-bombardment of a SF_6 gas target, and a gas transport system transferred the irradiated gas to the detection station. Branch events were identified

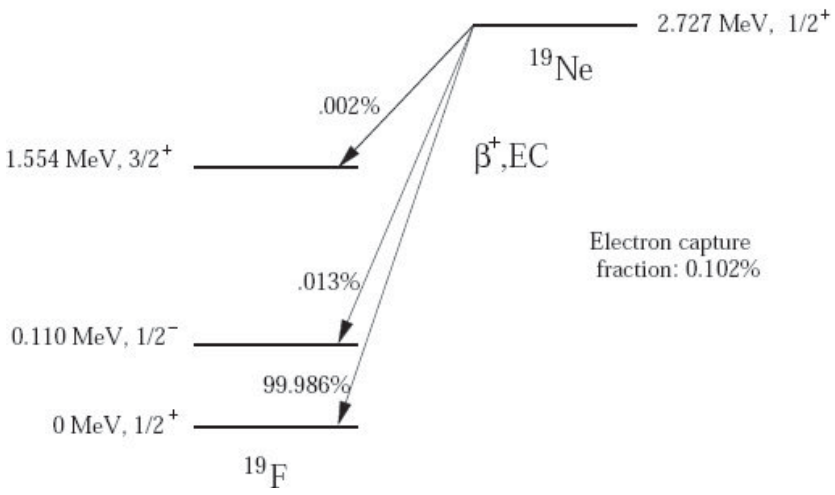

FIGURE 1.4: Level diagram for the ^{19}Ne decay to ^{19}F.

by a triple-coincidence between the annihilation gammas detected by back-to-back NaI detectors, and the excited state emissions detected by a Ge(Li) detector[2]. A second measurement of the 1554 keV state was extracted using the previous experimental setup, but with a Ge(Li) detector coaxial to the counting cell. The branching ratio was extracted by comparing the intensities of the 1357 keV and 511 keV peaks, as before[3]. The measurement of the 110 keV branch was improved by Saettler et al. in an experiment which also used a proton beam incident on an SF_6 gas target and collected the ^{19}Ne in an atom trap. The emission betas were collected by plastic scintillator detectors in coincidence with the emitted 110 keV gamma detected by a HPGe detector, and the branching ratio was extracted from the ratio of $\beta - \gamma$ coincidences to total β rate[68]. Other necessary experimental inputs include the total transition energy, Q_{EC}, which is taken from the mass excesses ΔM of the reaction participants, updated in advance of the 2013 NUBASE release by the Atomic Mass Data Center[5], and the electron capture fraction, P_{EC}[35]. These results are summarized in Table 1.4.

In order to access the interesting parameters in the Standard Model, a second observable must be available in order to set the form factor g_A. The original, and only

Table 1.4: Experimental inputs for calculating the $\mathcal{F}$t value in the ^{19}Ne system.

Input	Value	Reference
BR(1.55 MeV)	(0.0021±0.0003) %	[1]
BR(1.55 MeV)	(0.00234±0.00030) %	[3]
BR(0.11 MeV)	(0.012±0.002) %	[2]
BR(0.11 MeV)	(0.0113±0.0009) %	[68]
BR(0 MeV)	(99.9864±0.0022) %	calculated
P_{EC}	(0.101±0.001) %	[35]
$\Delta M(^{19}\mathrm{Ne})$	(1752.054±0.160) keV	[5]
$\Delta M(^{19}\mathrm{F})$	(-1487.44435±0.00086) keV	[5]
Q_{EC}	(3239.4983±0.160) keV	calculated

published, measurement of the beta asymmetry A_β was performed by Calaprice et al., who produced ^{19}Ne by bombarding SF_6 with 12 MeV protons, which were polarized in a Stern-Gerlach magnet and captured in a storage cell. The emitted positrons were detected by two plastic scintillators along the axis of the magnetic holding field, and the asymmetry in the detector rates gave the beta asymmetry[15]. This detection scheme was modified in a subsequent measurement by Schreiber, in order to reduce the uncertainty due to backscattered betas, and an improved precision was obtained[70]. A third measurement by Jones using that experimental setup intended to improve on the gain-shifts by instead using Si(Li) detectors, and a more accurate calculation of backscattering (though this systematic remained the largest source of uncertainty), and achieved a similar precision[47]. These results are summarized in Table 1.5. The beta asymmetry is related to the mixing ratio ρ,

$$A_\beta = \frac{\rho^2 - 2\rho\sqrt{J(J-1)}}{(1+\rho^2)(J+1)} \tag{1.43}$$

where J denotes the spin of the initial and final states of the nuclei; however, recoil order effects can produce a significant effect impact on the extraction of ρ. Naviliat-Cuncic and Severijns have calculated this effect and, omitting the unpublished doctoral dissertation results, obtained the value $\rho = 1.5995 \pm 0.0045$[59].

Table 1.5: Previous ^{19}Ne A_β measurements.

A_β	Source
-0.0391±0.0014	[15]
-0.03603±0.00083	[70]
-0.0360±0.0009	[47]

2

Experimental Method

This measurement is the culmination of efforts from a collaboration between the Triangle Universities Nuclear Laboratory (TUNL) and the Kernfysich Versneller Instituut (KVI). The experimental approach was based partly on a desire to take advantage of the capabilities of the Trapped Radioactive Isotopes: μicro-laboratories for fundamental Physics (TRIμP) dual-stage magnetic isotope separator at KVI. The team at KVI developed techniques for producing clean samples of ^{19}Ne using this separator. The separator target[82], and the experimental apparatus for collecting and transporting the samples and measuring the decay rates, were designed and constructed mainly by TUNL.

Several measurements were made at KVI as part of the collaboration's development of the experimental technique and instrumentation. The ^{19}Ne production mechanism and methods of eliminating radioactive isotope contamination were studied in October 2005. The experimental setup was developed in the following years and was used to attempt a first precision measurement of the lifetime in February 2008. Lessons learned in that attempt revealed aspects of the techniques and instrumentation where minor upgrades could reduce systematic errors and provide

methods for establishing the relative importance of systematic uncertainties in the lifetime determination. The upgrades to the experimental setup were performed for the final measurement in March 2009. In April 2009, we also attempted to measure the lifetimes of two more isotopes, ^{37}K and ^{21}Na.

The creation of isotopically pure samples of ^{19}Ne is discussed in detail in Chapter 3. In this chapter, the design and performance of the experimental setup beyond the separator are described. After summarizing the requirements of a high precision lifetime measurement, each component of the system is examined in detail. First, the motivation for our choice of implantation targets is given. The evolution of the design for the tape transport system and its performance are then discussed. Finally, the data acquisition system, including the detectors, electronics modules, and computer software, is described.

2.1 Method

By carefully reviewing the methodology of previous lifetime measurements, we can design a strategy to extract the lifetime of ^{19}Ne with minimal systematic effects. The most precise determination of a particle lifetime was obtained by the MuLan Collaboration with their recent measurement of the positive muon lifetime at the 10^{-6} level[29]. The collaboration's handling of rate-dependent data acquisition-related effects is of particular interest. This experiment used a detector array consisting of 170 stacked pairs of triangular plastic scintillators in a truncated icosahedron geometry to detect the positrons emitted in the decay. The corresponding 340 photomultiplier tube signals were recorded using waveform digitizers. Detected events were identified by fitting waveform pulse shapes to the pre-prepared average pulse shape. A minimum allowed pulse resolution was instituted to ensure consistent treatment of accidental event coincidences, and a variable-sized artificial deadtime was applied to all resolved pulses. The correction procedure was based on a statistical reconstruc-

tion of the accidental coincidence probability, performed by checking the relevant time window after each event in a separate measurement cycle for an accidentally coincident event.

In addition to the kind of rate-dependent systematics which plague any lifetime measurement, several effects are unique to the ^{19}Ne system. The first consideration is the production method and possible contamination. ^{19}Ne typically has been produced using the (p,n) reaction on ^{19}F in previous precision measurements of experimental observables. While several of these experiments noted the presence of an ^{15}O contaminant[6, 48], the first to attempt to purify the sample was the 1977 lifetime measurement by Vitale, by using an isotope separator[83]. Several experimenters took some precautions against diffusion of the ^{19}Ne out of the sample. Wilkinson and Alburger performed a comparison of the half-life obtained with and without a gold foil epoxied over their target[85]. Azuelos and Kitching[6] encapsulated their targets in beryllium cylinders. Vitale implanted several hundred atomic layers into an aluminum foil and sealed the foil with electrical tape, and compared measurements with and without sealing the target with electrical tape, and by implanting with half the particle energy in order to look for an effect due to diffusion.

In our experimental approach, we attempted to improve upon the techniques of these previous measurements. We developed our procedure with two goals in mind: first, to suppress any systematic effects which could affect the extracted lifetime, and second, to carefully characterize effects which could not be rendered negligible. A lifetime measurement is sensitive to any effects which change the apparent decay rate, particularly effects that change over time. The result can be skewed by any variation in efficiency for counting decays, changes in the ^{19}Ne population due to diffusion, and backgrounds from ambient radiation in the room or radioactive contaminants in the sample.

An overview cartoon of our general experimental approach is depicted in Figure

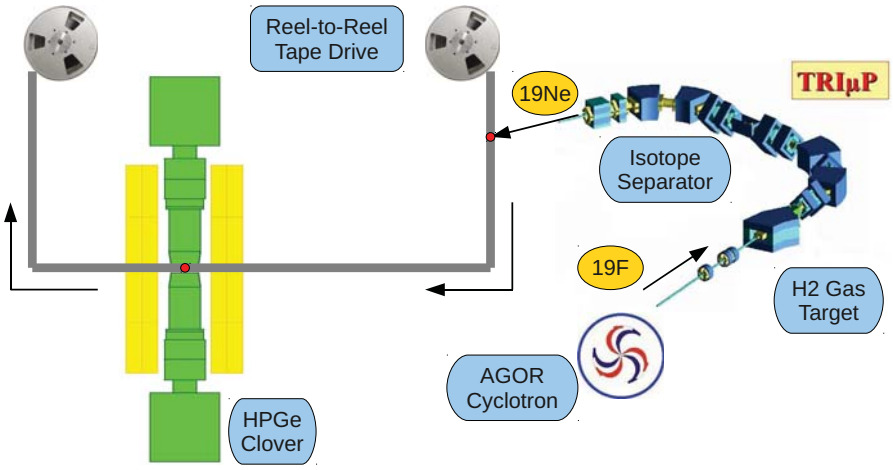

FIGURE 2.1: Overview of the experiment to measure the lifetime of ^{19}Ne.

2.1. A typical measurement cycle consisted of three phases: (1) the production of the ^{19}Ne sample, (2) the transportation of the sample from the separator to the center of the field of view of the detectors, and (3) the detection of the decaying particles. During the first phase, the AGOR cyclotron produced the primary beam of ^{19}F at 10.5 MeV/A. The ^{19}F beam interacted with the H_2 gas target to produce ^{19}Ne via the (p,n) reaction. The ^{19}Ne was then spatially separated from other possible productions in the TRIμP isotope separator, and implanted into an aluminum tape. Once the production phase was complete, a beam stop was activated to block the beam from entering the separator, and a custom tape drive system transported the collected ^{19}Ne sample to a shielded detection system. Finally, two High-Purity Germanium (HPGe) clover detectors counted the collinear annihilation gamma rays from the emitted positrons during the decay-counting phase. The signals from the eight clover segments were digitized and stored by a CAEN V1724 Waveform Digitizer.

Several key systematic effects inherent to this strategy have been identified. The first class of systematics include any effects which alter the efficiency for counting decays. For example, the fraction of events accepted by the energy threshold

cuts depends on a consistent conversion of observed pulse amplitudes to particle energy. To that end, the choice of the HPGe clover detectors, with their excellent energy resolution and very good gain stability, mitigated possible time-dependent and rate-dependent variations, and a continuous pulser along with the 511 keV line was sufficient to monitor the detector response over time. A second effect is due to deadtime of the data acquisition system, during which no events are stored. This effect was limited by the full digitization of the detector signals, and was tracked using the digitizer status flags and the continuous pulser. Finally, at high rates, the probability for accidental pulse coincidences increases, resulting in the loss of real events and gain of false events. We adopted a similar approach to that of the MuLan collaboration, in which pulses were identified by comparing them to a calculated average shape, an artificial deadtime was applied to all resolved events, and the corrections due to event deadtime, accidental coincidences, and energy pile-up were statistically reconstructed.

In the second class of systematics, the counting efficiency may change because the ^{19}Ne population itself is changing. Diffusion has been identified as a potential concern in previous measurements, but no strong limits have yet been placed on this effect. We attempted to directly study diffusion by performing separate precision measurements at several implantation depths and comparing the extracted lifetimes to the expected bias in the presence of diffusion.

Finally, any background events, either due to radiation in the room or contaminant isotopes in the sample, can introduce an effect. The ambient background rate was significantly reduced by using thick shielding and requiring a coincidence between clovers, and was measured frequently over the course of the experiment. Contaminant backgrounds produced with the ^{19}Ne were minimized using the isotope separator. However, characterizing the levels of contamination possibly present in the sample was much more difficult to do precisely. An estimate of the relative con-

taminant levels could be obtained using silicon detectors in the separator, and also by precisely measuring the lifetime for different choices of the implanting period.

2.2 Implantation

Once a clean sample of ^{19}Ne is obtained using the methods outlined in Chapter 3, the particles must be collected and moved to the detection system. Due to the constraints of the experimental area, a tape drive system offered the most economical approach for fast and precise transportation of the target. In this approach, the implantation target must take the form of a tape, which requires additional consideration for the type of material chosen. The particles that exit the separator have kinetic energies of less than 5 MeV/A, and therefore a thin, tape-like material is appropriate to ensure that all particles are fully stopped.

2.2.1 Tape material

The choice of the tape material target must conform to several specifications. First, it must be flexible enough to be guided as a tape and durable enough to be transported quickly. It must be light and low-friction, in order to avoid straining the driving motors; yet still easily gripped to ensure accurate placement. It should not be composed of isotopes that can be activated during implantation. Finally, especially for a noble gas such as neon, it must limit the diffusion of implanted particles.

Two materials were selected as implantation targets. The first material used was a 125 μm thick Mylar, metallized with 500 Å of aluminum on each side, produced by Grafix Plastics. This material was an excellent choice in terms of fast and accurate translation; however the aluminum layer was easily scratched, and some concerns remained over the effect of diffusion. To alleviate these concerns, a second material was constructed by All Foils, Inc., of 100 μm of aluminum, laminated to 0.1 μm of polyester with acrylic adhesive. More care was required during transport in order

to avoid crinkling the aluminum. Each material was slit into 1 inch wide strips and spooled onto 10.5 inch diameter metal reels with NAB (National Association of Broadcasters) style hubs, manufactured by Recordable Media Group International. Each reel was spooled with about 200 meters of tape, which provided about 2–3 hours of run time. A total of about 25 Mylar reels and 30 aluminum reels were available for the measurements. With so much length of tape available, it was never necessary to reuse a reel during the experiments. Therefore, the buildup of long-lived isotopes in the tape was not a concern.

2.2.2 Depth simulation

The requirements for tape thickness were determined by simulating the implantation depth using the SRIM (Stopping and Range of Ions in Matter) software package[87]. The included TRIM (Transport of Ions in Matter) program can be used to simulate the effects of an ion as it travels through complex materials, providing the simulated ion track and also details of kinetic phenomena such as target damage, sputtering,

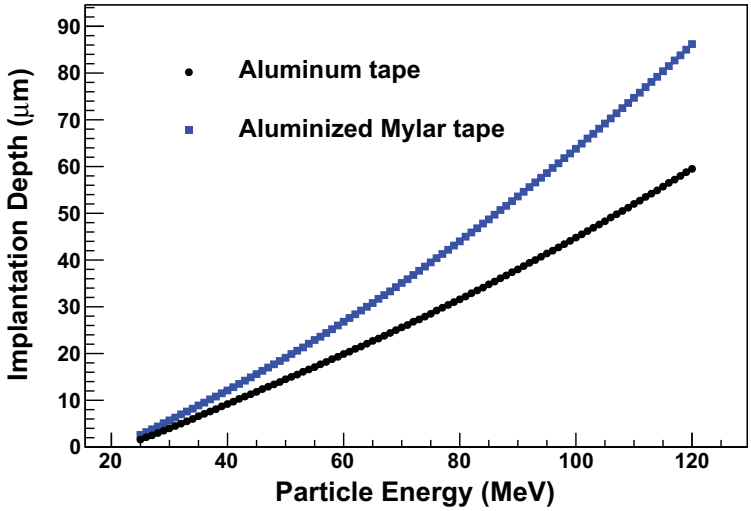

FIGURE 2.2: SRIM simulations of average stopping distance of ^{19}Ne particles after implantation into aluminized Mylar tape and aluminum tape.

ionization, phonon production, and atom cascades. In particular, the three dimensional distribution of ions implanted into a target can be simulated, which can be used to optimize the energy of the beam incident on the tape. Ideally, the particles should be implanted at a depth equal to half the thickness of the tape, so that diffusion out of the tape is minimized.

The actual energy of the particles exiting the separator depends on the energy of the primary beam, separator rigidity, and the material degraders used. Figure 2.2 shows the implantation depths of ^{19}Ne ions in the two targets over the range of energies exiting the isotope separator (before passing through the exit window) that were possible for the accelerator and separator setup used in our measurements. During the high precision measurement, the average energy of the ^{19}Ne particle beam exiting the separator was about 69 MeV, and the particles were implanted into the aluminum tape. Figure 2.3 shows the simulated implantation depth of 10^6 particles of 69 MeV ^{19}Ne into the aluminum tape. Fewer than 0.01% of the particles are

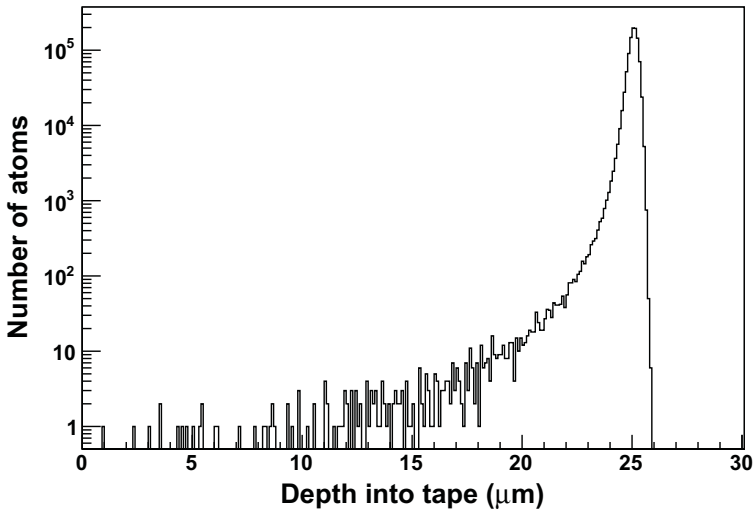

FIGURE 2.3: SRIM simulation of the distribution of ^{19}Ne after implantation into an aluminum target. Initial energy was set to 69 MeV, and 10^6 total particles were simulated.

implanted in the first 15 μm of the tape.

2.3 Tape drive system

At the end of the activation period, the implanted sample must be quickly transferred to the detection system for counting. A reel-to-reel tape drive system was selected as a cost-effective solution for transport. The system was designed to transfer tape originally stored on a "supply" reel to the exit of the isotope separator for particle implantation, then to a detection system to collect decay data, then finally to a "take-up" reel for storage. The most important parameter in the tape motion control is the accuracy and repeatability in the determined tape distance between the isotope separator exit and the center of the detection system. The tape drive system must be able to translate the implanted sample to the same position in the detection system in order to ensure maximum data rates and prevent second order effects such as cycle-to-cycle changes in detection efficiency and changes in the sensitivity of the detection system to contamination and diffusion.

2.3.1 Prototype

The first version of the tape drive system was developed at TUNL in 2007 and was used in the 2008 experiment. The system is modular in design, with each major function handled by its own freestanding component. This approach has many advantages, including ease of development of components, flexibility in setup, and simplified upkeep and repair. However, more care must be taken during setup to ensure alignment of components for proper coupling. The tape drive system uses three main components for tape control: the supply reel system, the driving mechanism, and the take-up reel system. Each of these components is driven by a servomotor, which follows programmed instructions from the central motion control system. The tape drive also includes extra features needed to fulfill experimental

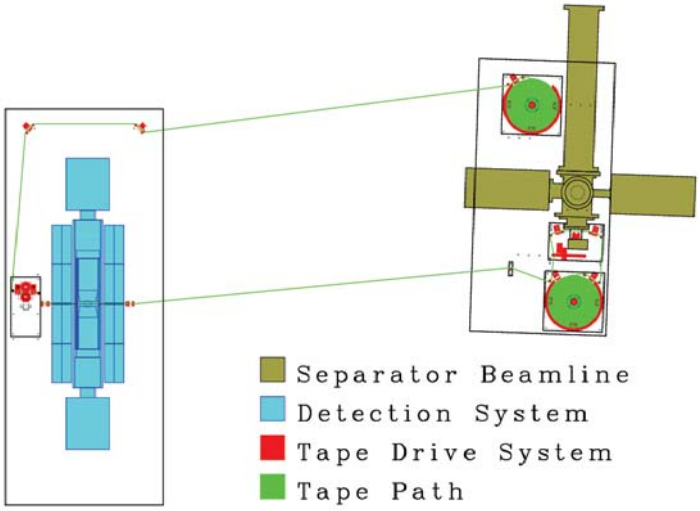

FIGURE 2.4: To-scale schematic of the tape drive system as installed during the 2008 measurement.

requirements, including the coupling to the separator beamline, the guide through the detection system, and a rudimentary position-checking scheme. A schematic of the prototype system is depicted in Fig. 2.4.

The tape motion was controlled by a commercially available system from Galil Motion Control, Inc. The central component of the motion control assembly is the DMC-2133 multi-axis controller. The DMC-2133 defines independent motion profiles for the three motors and maintains precision by continuously monitoring the encoder outputs, and adjusting the motor torque in order to compensate for the error in measured position versus the calculated position from the motion profile. It also monitors motor status for error conditions, and interfaces with the Galil software for user control, the DMC Terminal.

The motors are powered by the AMP-20540 multi-axis brush/brushless amplifier, which can provide up to 500 W of power per axis. The amplifier outputs a current to the motor proportional to a command signal output from the controller, which translates to the output motor torque. The total output power to all motors was

limited by the Mean Well SE-600-48 600 W power supply in use. Three Nema 23 frame, BLM-N23-50-1000 brushless servomotors with indexed, 1000 line resolution, differential quadrature incremental encoders were used for this application. Each motor is capable of 0.32 Nm of continuous torque and 2 Nm peak torque.

The motion control assembly is housed in a cooled electronics box constructed by TUNL, which allows for easy setup of required cabling for motor control, system inputs and outputs, and communication with a computer. The controller includes dedicated TTL (Transistor-Transistor Logic) digital inputs for forward and reverse limit switches for each motor axis, a home switch, and an abort switch. Activation of a limit switch causes a decelerated stop of the motor and prevents motion in the relevant direction until the error condition is reset. The home switch acts as a mechanical reference, and is used in pre-programmed homing routines. The abort input immediately stops current to the motors and cancels all motion programs. These inputs were used during development but not in the final incarnation of the prototype tape drive system. In addition to these inputs, the controller board includes 8 general purpose TTL inputs and 8 general purpose TTL outputs, and the amplifier adds 8 general purpose analog inputs with 12 bit resolution to the assembly. The motion control assembly defined the parameters of the measurement cycles during the experiment. These outputs were used to control various tape drive components, inhibit the beam from the cyclotron during the detection phase to reduce beam-generated backgrounds, and to communicate information about the current state of the system to the data acquisition system.

The driving mechanism is responsible for the motion profile and positioning of the tape (Fig. 2.5). The driving mechanism moves the tape by pressing it firmly between two urethane rollers: the drive roller couples to a servomotor which defines the motion, and the spring-loaded idler roller presses the tape against the driver. To meet the system requirement of precision in positioning, the assembly must be able to

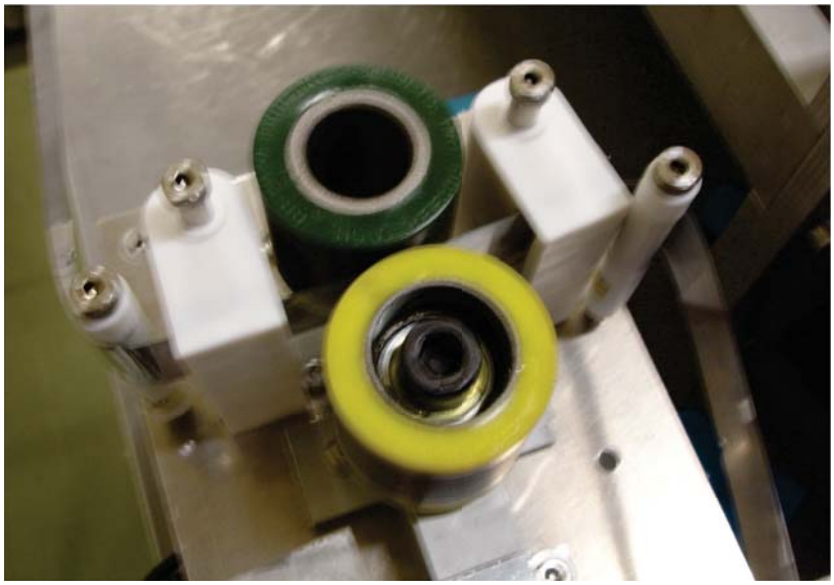

FIGURE 2.5: Prototype driving assembly. The tape is pushed against a drive roller (green) by the idler roller (yellow). Teflon guides (white) constrain the tape's position.

accurately convert the radial position of the motor to linear position along the tape. Error in positioning can arise from either change in radius of the driving roller, or poor coupling of the assembly to the tape. The first concern is addressed by preventing compression of the drive roller by using a a roller with very high durometer, or hardness. Conversely, the second issue is alleviated by using an very low durometer idler to provide superior grip. Also, tape guides mounted very close to the rollers constrained the vertical travel of the tape. During the first measurement, rollers with durometers of 80 A and 35 A, respectively, were used. Under test conditions, the maximum error in positioning due to the phase of the motor was found to be less than 1 mm.

The tape reel assemblies do much more than provide passive storage of tape not currently in use by the system (Fig. 2.6). These components ensure smooth and reliable transport over the duration of the tape reel. The tape reel rests on a custom reel table with a NAB style hub, which couples to the servomotor. The motor

FIGURE 2.6: Prototype tape reel system. The tape reel rested on a motor-controlled reel table. A reel protector contained the tape during unexpected tension loss or motor runaway.

supports the weight of the stored tape in order to ease strain on the driving motor. The reel motors also maintain tension on the tape so that it tracks correctly along the tape path. The tape reel assembly includes a reel protector, which is a metal shield with Teflon insets which rings around the tape reel. The insets act as bumpers which prevent the stored tape on the reel from falling out of the reel and becoming tangled underneath the assembly if the system suddenly loses tension, such as due to an error condition or a break in the tape.

The tape path was demarcated by simple tape guides made of polytetrafluoroethylene (PTFE) rods. Slotted PTFE blocks were also used to constrain vertical position at the entrance to major system components. All surfaces that came into contact with the tape were coated with a very low-friction polyethylene film. Special guides were designed for travel through the detection system, in order to minimize the area required for transport so that the detectors could be placed as close to the sample as possible.

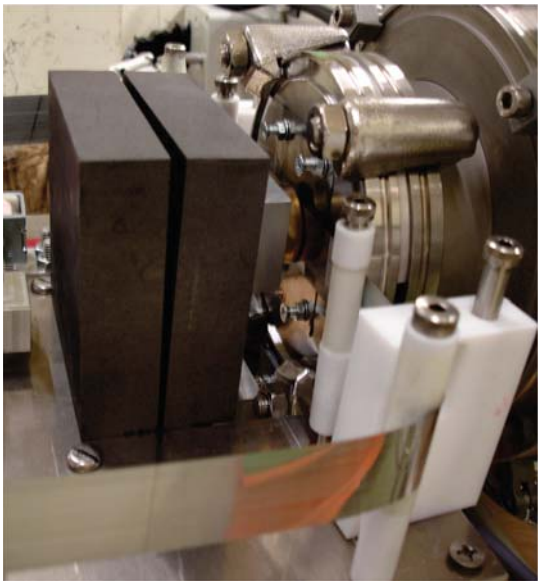

FIGURE 2.7: Tape drive coupling to the exit of the isotope separator. The tape passes near the exit window of the separator, which is protected by aluminum shims. A plunger mechanism pushes the tape onto the shim during implantation. Two graphite blocks immediately behind the plunger serve as the beam stop.

During implantation of isotopes into the tape, the tape drive system used a custom plunger to push the tape against the exit flange of the separator (Fig. 2.7). The exit flange had a 1 cm diameter circular gap drilled through the center for the particle beam to pass through, over which a 10 μm thick Havar foil was glued. To prevent damage to the foil from the tape, an aluminum shim was mounted to the flange which covered the foil edges and prevented the tape from coming into contact with the film. The plunger used a polyurethane cylindrical block to hold the tape against the shim. A control voltage from the DMC-2133 energized a relay to control the 24 V power to a linear solenoid actuator, which moved the plunger against the tape. The plunger had a circular gap which allowed the beam to pass through and stop in graphite blocks placed behind the apparatus.

One of the most important system requirements is that the tape drive must accurately move the implanted sample from the exit of the separator to the center

of the detection region. The detection system is placed over 2 meters away from the separator beamline in order to reduce backgrounds. The tape can sag as it crosses the gap between the systems, which could result in a variation in the length of tape between the detectors and the separator on a cycle-to-cycle basis. To minimize variation, the tape is held under very high tension by the driving mechanism and the supply reel system as the beamline plunger activates. The accuracy in positioning was checked by marking the tape and translating the tape to fixed positions just before and after the detection system, in addition to studies using the observed relative rates of the detector segments. Under optimum running conditions, the error in positioning was less than the accuracy of the measurement, or about 1 mm. A marking scheme was developed in which a marker located downstream of the separator exit was actuated by another linear solenoid after the tape was clamped for implantation, and the marked position was checked by web-camera against a ruler affixed outside of the detection system. This system was only used for about 10-20% of measurement cycles, as the markers quickly dried out and needed to be replaced too frequently to be practical.

The prototype system demonstrated that a tape drive system is capable of meeting system requirements for speed and accuracy in moving the implanted samples. However, the performance of the system degraded severely over time due to use outside of system specifications. The motors gradually weakened over the course of the experiment, and eventually the amplifier had to supply maximum voltage for the motors to be able to pull the tape. In addition, the encoder inputs on two axes of the DMC-2133 failed. Therefore, two motors (chosen to be the reel assembly motors) had to be operated in "open-loop" mode, such that these motors could not undergo any profiled motion, and instead only applied a constant torque to the system. This mode is more dangerous, as when the tape breaks from a reel, the constant torque applied will drive the reel assembly at very high speeds, potentially damaging the

system. As the performance declined, the profiled moves became more spasmodic and jerky. Occasionally, the uneven motion would cause the tape to slip from the drive mechanism, and the implanted samples would fail to reach the center of the detection system.

Several flaws were identified with the system design which contributed to the observed failures. The servomotors had to be operated at near maximum power in order to move the tape at required speeds. Late design changes in the experimental setup resulted in many more tape guides being used than in the test setups, and therefore more friction points for the tape. In addition, the motion control assembly included a few poor electrical connections and needed repair from the manufacturer.

2.3.2 Final design

While the tape drive system was able to be used for a successful preliminary measurement, several areas were identified that had room for improvement. The system had been established as worth a significant investment for improving the precision in the measurement, and many components of the system were upgraded or redesigned. In addition, new features were introduced to the system, including tape clamps at the detection system, tension-absorbing dancer arms, tension feedbacks for the reel mechanisms, and an out-of-tape sensor. A concept sketch of the final tape drive system is shown in Fig. 2.8.

The biggest concern in the prototype tape drive was the reliability of the system over time. This was addressed by upgrading the power of the motion control system. The motors were upgraded to the Nema 34 frame, I3486-197NC brushless servomotors from Motion Control Group, Inc. These motors were capable of up to 2.22 Nm continuous torque and 6.85 Nm peak torque if used at specified input voltage of 325 V. The motors are usable at lower voltages, such as provided by the 48 V Galil AMP-20540 amplifier; however, the available torques are reduced and

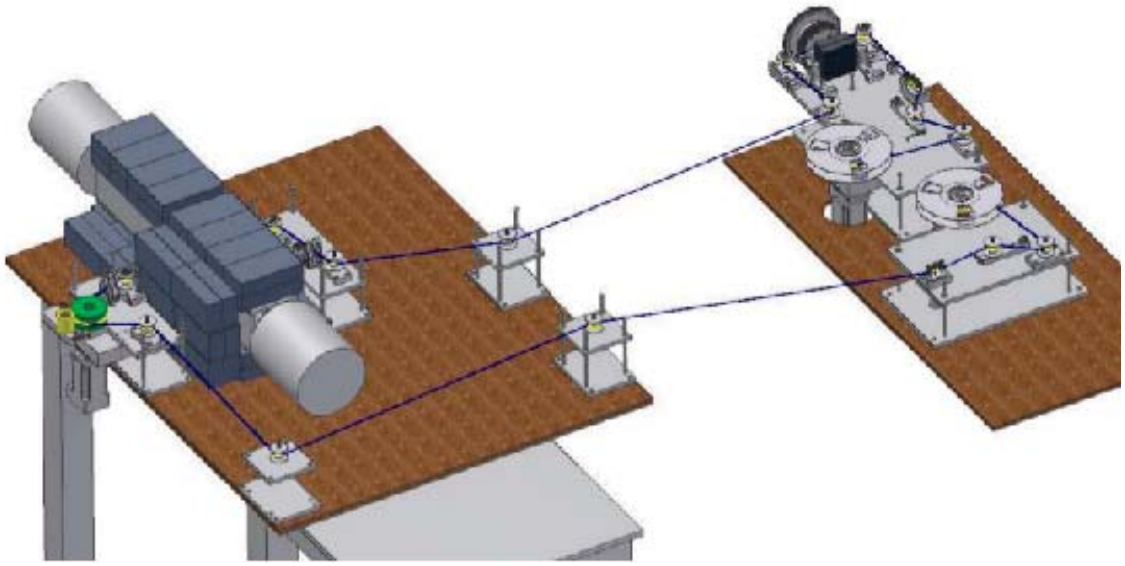

FIGURE 2.8: Schematic of the 2009 tape drive system. System component placement varied somewhat during the actual experiment.

then limited by the current capabilities of the amplifier. With the 7 A continuous and 10 A peak current available, the motors can generate 1.1 Nm continuous and 4.83 Nm peak torque, respectively. These specifications proved more than adequate for our application. The motors were fitted with Pittman indexed, 2000 line resolution, differential quadrature incremental encoders. To support the larger motors, an upgraded power supply was selected, the Mean Well RSP-1000-48, 1 kW supply.

The second major issue was the stability of the tape motion. Sudden acceleration of the tape by the driving mechanism elicited an uneven response from the supply reel mechanism, which could result in severe oscillations. The oscillations are abated by very careful tuning of the servomotor system, but the tuning process is tedious and can be dependent on many factors, including motion profile parameters, tape path, and the weight of the tape on the reels. An alternate solution was to introduce two new components to the system: the dancer-arms and the tension feedback (Fig. 2.9). The dancer-arms address the stability of the system directly by dampening the os-

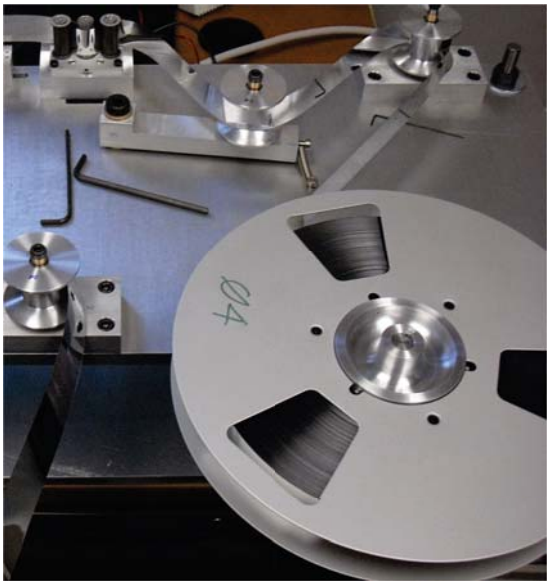

FIGURE 2.9: Upgraded tape supply reel assembly. After exiting the supply reel, the tape passes through a dancer arm, then a tension feedback sensor.

cillating response of the reels. The dancer is a special guide which rests at the end of a rotating arm, held at a fixed angle by a spring. When the driver accelerates the tape, the oscillations are absorbed by the rotating arm, such that the torque on the motor remains nearly constant. The tension feedback system normalizes the response of the motor against the changing radius of the supply assembly due to tape leaving the reel, and guarantees constant tension is applied over the length of the reel. It also improves the response of the reel motor to sudden accelerations. The tape was threaded through a Check-Line TERX-1K-30 tension sensor, and the output tension was read by the analog input on the assembly. The controller then made small adjustments to the applied motor torque until the tension reached the desired level. The rate and magnitude of adjustments did require some tuning for optimum performance.

A new, well-ventilated and fully enclosed electronics housing for the motion control assembly was designed. The power supply was moved outside of the box due to

concerns about the heat output. The housing patched through more of the available inputs and outputs from the assembly to the front panel, with some extra circuitry to handle specific needs of the tape drive system. One new such feature of the tape drive system was an out-of-tape sensor, an optical sensor through which the tape passed, which controlled the limit switch inputs of each motor axis. Another new feature was a set of clamps actuated by SMC SY5120-SLZ-01 pneumatic solenoids which surrounded the detector, so that the tape could be held firmly in place during the detection phase while the motors were turned off, reducing possible electronics noise. The main operation of the tape drive was handled using a new, push-button interface. The START button initiated a sequence of readiness tests and prepared the tape drive system for running after a new tape reel is installed, or after recovering from error. The RESUME button started the series of measurement cycles, or resumed them after a PAUSE. The PAUSE button completed the current measurement cycle, then settled the system into a stand-by mode. Finally, the STOP button immediately aborted all tape drive functions, such that it could only be restarted with a new START request. The abort sequence was also initiated if any system error condition was detected or when the supply reel tape ran out. Adjustment of system parameters, such as changes in the measurement cycle timing, fine-tune of the final positioning of the implanted sample, or tweaks to motor response, still needed to be performed using the DMC Terminal software.

All other components of the system experienced an overhaul in design, to improve overall robustness, simplify maintenance, and refine their performance. The new driving mechanism increased the diameter of the drive roller to 4 inches, which improved resolution and increased the contact surface of the tape (Fig. 2.10). The idler roller was installed on a rotating arm which could be easily moved for tape installation, and then locked in place for tape motion. The tape reel assemblies included simpler reel protectors, which completely surrounded the reel table such

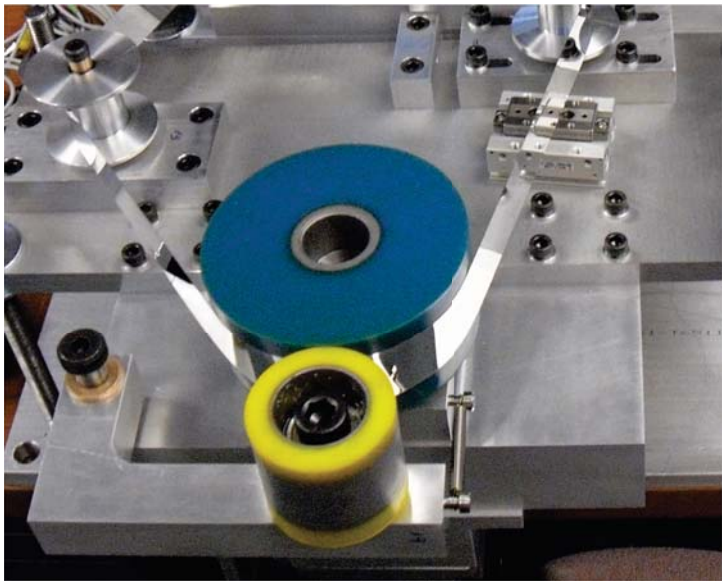

FIGURE 2.10: The upgraded drive mechanism used a spring-loaded idler roller (yellow) to press the tape against the increased-diameter drive roller (blue).

the tape could not fall below the hub assembly. The tape guide system was replaced by freely rotating spools with adjustable flanges for vertical alignment. Finally, the plunger mechanism which held the tape against the separator beamline exit was redesigned to use a two SMC SY5120-SLZ-01 pneumatic solenoid actuators to press the polyurethane block against the tape.

Some maintenance was required throughout the experiment to ensure optimum performance. After heavy use, the springs that supported the dancer-arms and the driving mechanisms would wear out, and needed replacement. Also, the tension feedbacks were easily damaged by operation out of specifications, and one was ruined by incorrect threading of the tape through the tensioner. A few of the general purpose inputs to the motion control assembly eventually failed. Despite these minor setbacks, the redesigned tape drive system was a marked improvement over the prototype system. This system was responsible for driving both the aluminized Mylar tape and the more finicky aluminum tape. The system was able to precisely

position the implanted sample in less than 3 seconds using the aluminized Mylar tape, and in less than 10 seconds using the aluminum tape. The tape motion was nearly free of the jolting behavior which ruined the positioning precision of the prototype system.

2.4 Lifetime measurement

Once the sample of ^{19}Ne isotopes is prepared and positioned, the lifetime measurement can be performed. The lifetime is extracted by measuring the rate of ^{19}Ne decays over time using HPGe detectors mounted in a shielded enclosure. The signals from the detectors are shaped and digitized, and the resulting waveforms are stored. Care must be taken to characterize rate-dependent and time-dependent effects inherent to this system.

2.4.1 Detection system

In this measurement, the ^{19}Ne decays were counted by detecting the two 511 keV gamma rays created when the positron emitted in the decay annihilates with an electron in the material surrounding the sample. The fact that the gamma rays must always be emitted 180 degrees from each other is exploited in the design of the detection system. The gamma radiation is detected by two HPGe clovers which face each side of the tape, mounted as close to it as possible in order to cover a large solid angle. Requiring a coincidence between the detectors significantly reduces events due to backgrounds. An overview of the detection system is shown in Fig. 2.11.

The positron is emitted in ^{19}Ne decay with up to 2.727 MeV energy. A material thickness of 1 cm was determined by PENELOPE simulation of the geometry to be sufficient to ensure that all positrons annihilate before reaching the detector[7]. The stopping material consisted of two 1 cm thick, 10 cm $\times$ 10 cm Delrin blocks, which were designed to also serve as a tape guide. The sample implanted in the

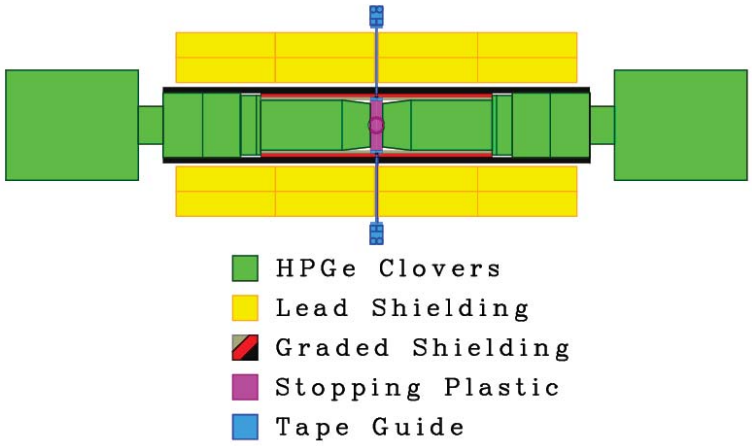

FIGURE 2.11: Detection system used in the ^{19}Ne lifetime measurement. The detectors were mounted in a shielding assembly, which was surrounded by blocks of clean lead.

tape entered the detection system through a specially designed, 5 mm thick guide, in order to minimize the opening through the shielding, then entered the 1 mm aperture between the Delrin blocks. The Delrin also acted as a mount for a customized 1 mm thick, 25.4 mm $\times$ 25.4 mm BC-400 plastic scintillator, embedded in a 1 mm thick, 25.4 mm $\times$ 101.6 mm BC-800 UVT acrylic light guide, developed by Saint-Gobain Crystals. The scintillator system was originally included to detect the positron before it annihilated in order to further reduce background events; however, the assembly gave unreliable results and was not installed in the 2009 ^{19}Ne lifetime measurement.

The HPGe clover segmented detectors, provided by KVI, were selected to detect the annihilation radiation due to their superior energy resolution. The clovers can resolve the energy of events to 2–3 keV. The energy spectra can therefore be inspected for extra peaks due to emitted gamma radiation from contaminant isotopes in the sample. The detector segments are arranged in a cloverleaf formation. Estimates from PENELOPE simulations indicated that the detectors should have a

total efficiency for detection of decay events in the current geometry of about 5%[7]. During the 2008 measurement, one of KVI's detectors failed, and a single crystal germanium detector was provided by Andreas Zilges from the University of Cologne. During the final high precision measurement in 2009, the experiment instead used another HPGe clover detector on loan from the EXOGAM experiment at GANIL.

The detectors were mounted in a custom shielding assembly, which was surrounded by 10 cm of lead. Nearly 100 lead bricks were stacked around the assembly. Each lead brick was screened for radioactivity using a single crystal germanium detector to detect gamma radiation. Each side of the brick was counted for approximately 12 hours, and any brick which had an appreciable rate above background was rejected (Fig. 2.12). The shielding assembly provided extra layers of protection against backgrounds originating from the lead, by surrounding the detectors with 0.25 inches of aluminum, then copper, then steel.

The germanium detectors must first be cooled to liquid Nitrogen temperatures

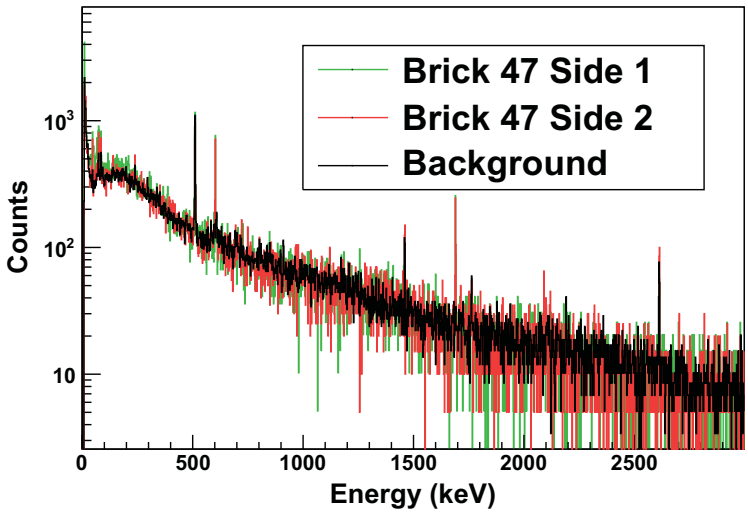

FIGURE 2.12: Gamma ray spectrum from a rejected lead brick. Gamma lines above background were detected at 603 keV, 1690 keV, and 2090 keV.

before biasing with high voltage. The detector assemblies included a cryostat and nitrogen dewar, which hanged freely outside of the shielding assembly. The dewar for the single crystal detector borrowed from Cologne instead served as its mount point, with the crystal simply inserted into the shielding assembly. The detectors were slowly biased using Ortec 459 high voltage supply for the EXOGAM detector and a Canberra 3106D high voltage supply for the KVI detector. These supplies accepted an inhibit signal from the detectors which automatically turned off the bias voltage if the temperature of the crystal increased above the manufacturer's threshold. The temperature of the system was regularly monitored to ensure safe operation. The dewars were filled with liquid nitrogen every 10 hours.

2.4.2 Data acquisition

Each of the germanium detector assemblies provided pre-amplifiers for signal output of each segment. In order to monitor gain and pileup effects, two Berkeley Nucleonics Corporation DB-2 random pulse generators were fed into the test inputs of each clover, which is internally fanned out to all of the clover segments. The pulsers were used in external trigger mode, with the external trigger created by the pulse generator on the CAEN V2718 VME-PCI Optical Link Bridge. The V2718 pulser was observed to have a period stability of better than 10 ns. The pulser gain was such that the pulser energy peak was located at about 1.25 MeV. The pulsers produce signals with rise times of 1 ns and the fall times of 1 ms, and the resulting pulse shapes were very similar to that of true event pulses.

The pre-amplified signals from the eight clover segments were each shaped with a 0.5 μs shaping time and active baseline restoration by one of eight Ortec 572A amplifiers. The shaped signals were read by the CAEN V1724, 8 channel, 14 bit, 100 MHz sampling time digitizer. The resulting digitized waveforms were timestamped and transferred via optical link to the CAEN A2818 PCI optical controller in an

acquisition-dedicated computer.

Though not used in the 2009 production data accumulation run, the plastic scintillator system is described here for completeness. The plastic scintillator light guide assemblies were both coupled to Electron Tubes Enterprises 9111SB photomultiplier tubes (PMT) located at each end of the assembly. The PMTs are biased by the C673A voltage dividers, and powered with -1.3 kV high voltage from an Ortec 556 power supply. The discriminated PMT signals were ANDed and used to create a 2 μs wide gate, which was delayed to overlap with the rise time of the coincident, shaped clover segment signal. The resulting NIM gate was converted to LVDS by a CAEN V1495 General Purpose VME Board, then input into the general purpose inputs available on the V1724 digitizer, which were read at trigger time and included in the data stream. The status signals from the tape drive system were also input in this way. The electronics chain is depicted in Fig. 2.13.

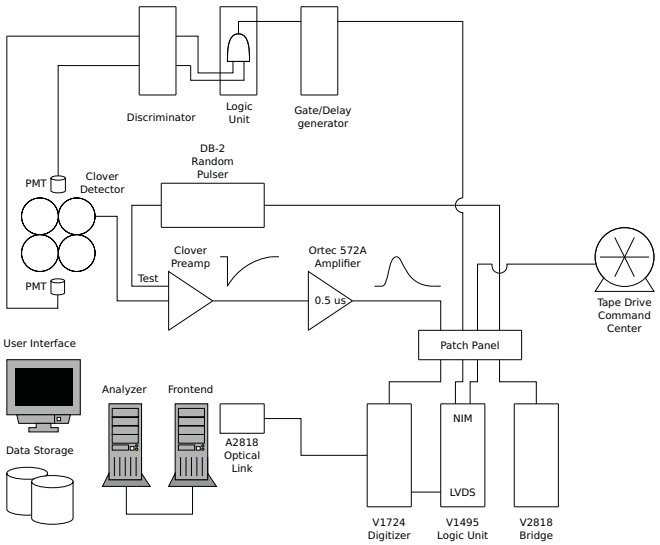

FIGURE 2.13: Electronics diagram of data acquisition system. The signals from the detector and pulser are shaped and digitized by the V1724 digitizer. The state of the digital inputs from the tape drive and scintillator assembly are read at trigger time.

Each channel of the V1724 digitizer has 1 MB Static random-access memory (SRAM), which can be divided into a programmable number of circular memory buffers to store each event. The memory was divided into 1024 event buffers, which stored 512 2-byte samples. The clock was run at the full 100 MHz, such that each event buffer was 5.12 μs long. The digitizer accepts voltage signals in each channel within a dynamic range of 2.25 V, which were individually offset by a programmed 16-bit digital-analog converter (DAC) within the total available range of $\pm$ 2.25 V. The voltage signals are converted to a 14 bit value by the on-board analog-digital converter (ADC). The data stream is continuously written to the active circular memory buffer.

When the voltage level of any channel increases above the set threshold level for a programmed number of samples, that channel generates a trigger which can be propagated to all other channels. On receiving a trigger, the digitizer stores the header information, stores a further number of "post-trigger" samples, freezes the buffers for data-readout, then begins continuously writing on the next available set of circular memory buffers, without deadtime. If a second trigger is generated after less than 512 samples of the first, only the remaining portion of that event is written to the next buffer. Each trigger is associated with a 31-bit counter, incremented with the sampling clock, a trigger event counter, a mask of participating channels, the size of the event, and the mask of the general purpose digital inputs, which are stored in the event header. At read-time, the frozen buffers are scanned to determine if they met criteria for zero suppression. The algorithm used for zero suppression was identical to the trigger criteria; if the signal increased above threshold for the programmed number of samples, the channel was deemed valid and added to the channel mask of the header. Event read-out occurs independently of signal writing, so that the system should be deadtime-free unless the memory buffer becomes full. The Buffers Full status of the digitizer was read along with the event information.

The on-board trigger management was later found to be less than ideal for our application. If the trigger times of multi-channel events were not perfectly aligned, the digitizer considered each channel to have generated a separate trigger. These events would then reserve several extra buffers containing only a few samples each, which unnecessarily reduced the number of available event buffers and limited the maximum achievable data rates. Zero suppression introduced a related issue. If the buffer size was smaller than the requirement for samples above threshold, the buffer was automatically rejected by the zero suppression routine. Some multi-buffer events therefore had small gaps in the waveform. Another issue with the triggering system is that a channel would not produce another trigger until the signal fell below threshold for the programmed number of samples, even if the end of the buffer was reached. This introduced extendable deadtime to the system, such that undetected extra pulses could extend the time the channel required to re-arm. These issues needed to be corrected using the methods discussed in Chapter 4.

The buffers were grouped into "Transfer Blocks" and optically transferred to a front-end computer dedicated to receiving events. The acquisition of events was mediated by the Maximum Integration Data Acquisition System (MIDAS) software[66]. The front-end application pings the digitizer every 1 ms and performs a block transfer, such that many events can be read and transferred in a single system call. The Transfer Block was then transferred over a direct network link to the analyzer application on a back-end computer, which performed simple online ROOT-based[13] analysis of some of the data, and wrote the Blocks to disk in an optimized MIDAS format. The analysis module of the analyzer application created histograms for simple analysis and data checking which were accessed and displayed in real-time by the Roody application's histogram visualizer graphical user interface.

Several parameters were monitored during the experiment to ensure optimum performance of the experiment. The separator gas target pressure and beam cur-

rent from the cyclotron were monitored occasionally using the separator interface. The DMC Terminal reported any minor errors in tape drive operation, and an audible alarm and flashing warning light signaled major concerns with the tape drive that required immediate attention before resuming the measurement, such as the tape reel running out. The data stream itself was continuously monitored using the Roody application. The data rates of the clover segments gave a general overview of the measurement cycle state and performance of the overall system. A drop in rate indicated possible problems with the cyclotron, isotope separator, or tape drive operation. The relative rates of the clover segments could be used to ensure no changes were occurring in tape positioning. Online fits of the data indicated the presence of systematic effects at the few percent level. Finally, the rate and amplitude of the pulser events were monitored for deadtime and gain shifts.

3

Production of ^{19}Ne

One of the primary objectives of the development stage of the experiment was to ensure that ^{19}Ne could be produced in large enough quantities and with minimal contamination in order to perform a precision measurement of the lifetime. The production reaction was evaluated based on optimal production rate of ^{19}Ne relative to contaminant isotopes. The use of the TRIμP separator to further reduce contamination was studied in great detail with simulations and measurements in advance of the experiment.

3.1 Production mechanism

The ^{19}F(p,n)^{19}Ne reaction was selected for its high cross-section for ^{19}Ne production and low contaminant production at low energies. This reaction has previously been used to perform precision studies with this system[6, 15, 47, 64, 70, 83]. The cross section for this reaction has been measured many times in the past, using a variety of techniques. One of the earliest measurements by Blaser et al. bombarded a target of LiF vacuum evaporated onto gold with protons. Energy variation across the length of the target was introduced by an aluminum wedge placed in front of the target. The

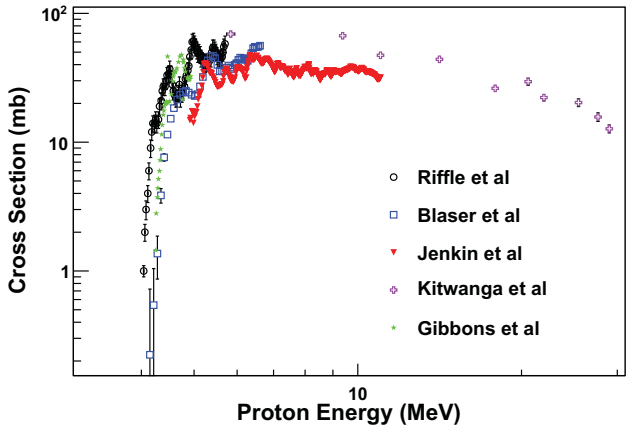

FIGURE 3.1: Compilation of cross section results for production of ^{19}Ne from proton bombardment of a ^{19}F target.

target was then used to expose a photographic plate, such that the blackening across the length of the plate was proportional to the cross section as a function of energy. Absolute cross sections were determined by comparing to the results using known cross sections of ^{63}Cu and ^{62}Ni[11]. Gibbons and Macklin used an alternate method of bombarding a target of $U^{238}F_4$ vacuum evaporated onto a platinum backing with protons, then transferring the target into a large graphite sphere embedded with eight BF_3 neutron counters[38]. Later experiments used NaI(Tl) gamma spectrometers to count the ^{19}Ne decay positron annihilation radiation in coincidence, after irradiating targets of MnF_2 evaporated onto gold (Jenkin et al.[46]), CeF_3 evaporated on gold (Riffle et al.[65]), or LiF powder (Kitwanga et al.[48]) with protons. Kitwanga also noted the production of an ^{15}O contaminant along with ^{19}Ne. The cross section data from these experiments (as taken from the CSISRS library in the NNDC[17]) is shown in Fig. 3.1.

For this measurement, the inverse reaction of 10.5 MeV/A ^{19}F incident on a H_2 target was used. The primary beam of ^{19}F was produced in the AGOR (Accélérateur Groningen-ORsay) cyclotron at KVI. The beam entered a 2 atm H_2 gas target de-

signed by TUNL[82] which was separated from the vacuum system by 4 μm HAVAR foils. After interaction with the target, ^{19}Ne can be emitted in any direction in the center of mass frame with energy of the colliding primary beam and proton, less the reaction threshold of about 4.23 MeV. Only particles emitted narrowly along the separator axis make it through the entrance collimator, defined by a momentum acceptance of about $\pm$2%, such that two populations of ^{19}Ne are created in the lab frame, a forward-directed group with an average energy of 10.2 MeV/A, and backward-directed group with an average energy of 8.7 MeV/A.

Several contaminant isotopes could be produced at the chosen primary beam energy. A significant production of ^{16}O was expected from the ^{19}F(p,$\alpha\gamma$)^{16}O reaction, as well as a small production of ^{20}Ne from ^{19}F(p,γ)^{20}Ne, both of which are stable isotopes. Based on reaction threshold, a possible production of the positron emitters ^{15}O from the ^{19}F(p,nα)^{15}O reaction with threshold at 8.9 MeV, and ^{18}F from the ^{19}F(p,d)^{18}F reaction with threshold at 8.6 MeV, may have been present. ^{15}O has been observed in previous studies of the ^{19}Ne system[6, 48]. Secondary reactions are also possible, notably ^{16}O(p,γ)^{17}F, or ^{16}O(p,α)^{13}N at a threshold of 5.6 MeV.

3.2 TRIμP isotope separator

The TRIμP separator operates on the principle of the Lorentz force (with $\vec{E} = 0$), using dipole magnets to deflect particle beams based on their charge and momentum. The magnetic field introduces a force perpendicular to the particle motion resulting in a circular trajectory, with angular velocity ω and radius of curvature ρ,

$$\frac{d\vec{p}}{dt} = q\vec{v} \times \vec{B}, \tag{3.1a}$$

$$p\omega\hat{\rho} = qvB\hat{\rho} \tag{3.1b}$$

$$B\rho = \frac{p}{q} \tag{3.1c}$$

where generally, $p = \gamma mv$ is the relativistic momentum. The last expression defines the magnetic rigidity of the separator (left-hand side) and the particle (right-hand side). The kinetic energy of a particle with mass A and charge Z can be derived by performing a Taylor expansion.

$$KE = \sqrt{p^2c^2 + m^2c^4} - mc^2 \tag{3.2a}$$

$$= mc^2\sqrt{1 + \left(\frac{qB\rho c}{mc^2}\right)^2} - mc^2 \tag{3.2b}$$

$$= mc^2(1 + \frac{1}{2}\frac{(qB\rho)^2}{m^2c^2} - \frac{1}{8}\frac{(qB\rho)^4}{m^4c^4}\ldots) - mc^2 \tag{3.2c}$$

$$KE = \frac{1}{2}\frac{(qB\rho)^2}{m} - \frac{1}{8}\frac{(qB\rho)^4}{m^3c^2}\ldots \tag{3.2d}$$

The time of flight is also easily derived,

$$p\omega = qvB \tag{3.3a}$$

$$= p\frac{\Delta\theta}{\Delta t} \tag{3.3b}$$

$$\Delta t = \frac{p\Delta\theta}{qvB} \tag{3.3c}$$

$$= \frac{\gamma m\Delta\theta}{ZB} \tag{3.3d}$$

Because the maximum particle energies are relatively low, the nonrelativistic approximation can reasonably be applied, with $\gamma \approx 1$ and $(ZB\rho)^4 = p^4 \ll A^3c^2$. The kinetic energy and time of flight of a particle with mass A and (fully ionized) charge Z is therefore given by

$$KE = \frac{1}{2}\frac{(ZB\rho)^2}{A} \tag{3.4a}$$

$$TOF = \frac{A\theta}{ZB} \tag{3.4b}$$

For a fixed separator rigidity, the result that total energy of the particle beams vary as $\frac{Z^2}{A}$ and times of flight vary as $\frac{A}{Z}$ is obtained.

If the particle is fully stopped in the detector, its total energy is deposited; otherwise, only part of its energy is deposited in the detector. The energy lost by a particle traveling through a medium is governed by the Bethe formula[53],

$$-\frac{dE}{dx} = K\left(\frac{Z}{\beta}\right)^2\left[\ln\left(\frac{W_{max}}{I}\right) - \beta^2\right] \tag{3.5a}$$

$$W_{max} \simeq \frac{2m_e c^2\beta^2}{(1-\beta^2)}, \qquad M \gg m_e \tag{3.5b}$$

where M is the mass of the incident particle and K and I depend on the properties of the medium. In the nonrelativistic limit,

$$-\frac{dE}{dx} \sim \left(\frac{Z^2 A}{E}\right)\left[\ln\left(\frac{2m_e v^2}{I}\right)\right]. \tag{3.6}$$

Removable silicon detectors located after each detector stage are used for online isotope identification and to aid in optimizing separator settings. These detectors register the deposited energy and timing relative to the phase of the cyclotron frequency of each particle. If the particle is fully stopped in the detector, its total

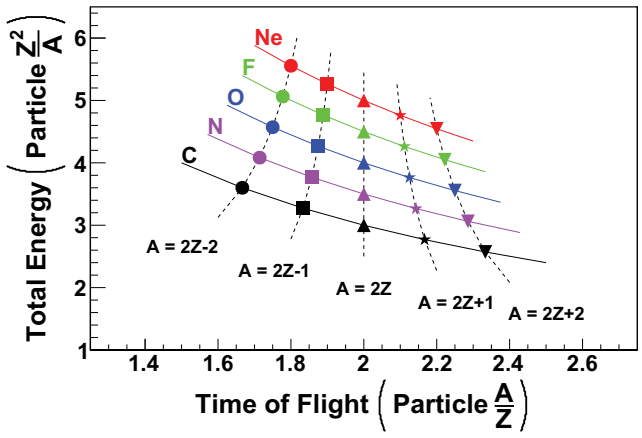

FIGURE 3.2: Expected plot of isotope energies vs. times of flight for particles that are stopped in the detector based on calculated dependence on mass and charge at a fixed separator magnetic rigidity.

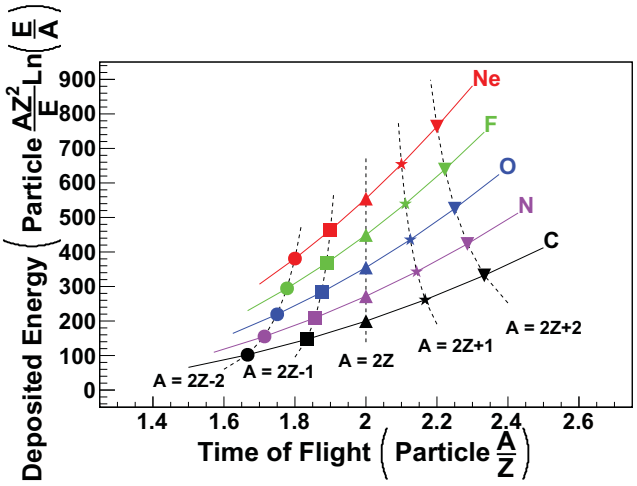

FIGURE 3.3: Expected plot of deposited isotope energies vs. times of flight for particles that pass through the detector based on calculated dependence on mass and charge at a fixed separator magnetic rigidity.

energy is deposited. By forming a 2-D plot of the total energy against time of flight ($\frac{Z^2}{A}$ vs. $\frac{A}{Z}$) of all particles, different isotopes can be visually separated for easy identification (Fig. 3.2). If the particles pass through the detector, the deposited energy is determined from Equation (3.6). The expected plot of deposited energy vs. time of flight for a thin silicon detector is shown in Fig. 3.3.

As the separator rigidity is varied, the separator accepts a different window of particle energies. The detector thickness could be chosen such that as the selected energy increases, the particles transition from being stopped in the detector to passing through the detector. The energy at which this transition occurs for a given detector thickness for each isotope can be simulated using SRIM. This feature provides an additional constraint for identification of observed isotopes.

The TRIμP separator (Fig. 3.4) removes contamination in two stages[82]. In the first, the accepted particle beams are dispersed by the dipole magnets such that only particle beams with magnetic rigidity $\frac{p}{q}$ matching that of the separator $B\rho$ survive, as described previously. In order to separate isotopes with the same rigidity, a degrader

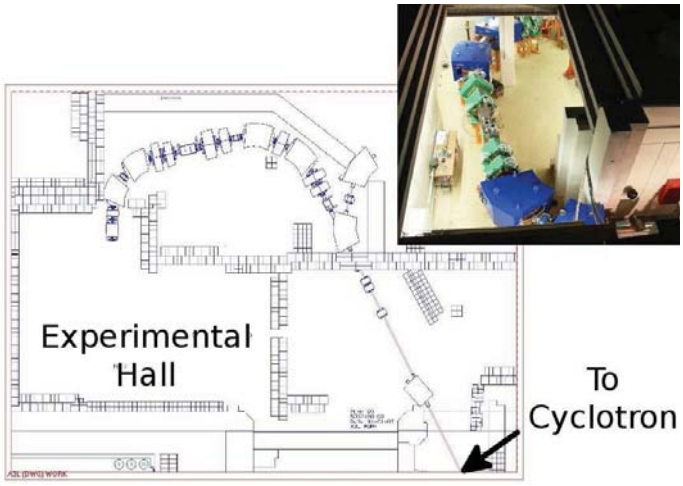

FIGURE 3.4: The TriμP isotope separator purifies reaction products of the primary particle beam from the cyclotron in the H_2 gas target, and delivers them to the experimental hall.

can be installed after the first stage. The degrader is wedge-shaped to preserve achromaticity of the beams. After passing through the degrader, the particle beams lose energy as determined by Equation (3.6), such that their magnetic rigidities no longer match. The second stage of the separator is then tuned to the reduced rigidity of the target isotope, and the other isotopes are no longer accepted.

3.3 LISE++ predictions

The analysis program LISE++ was used to simulate the transport of ^{19}Ne and other particles through the TRIμP separator[78]. LISE++ can simulate most aspects of the separator, including reaction mechanics in the target, energy degradation in the target, vacuum windows, and material degrader, deflection and focusing due to the dipole and quadrupole magnets, and acceptance due to collimators and slits. By loading cross sections for known reactions, the relative production rates of isotopes can be calculated in order to determine optimal separator settings to maximize ^{19}Ne production with respect to contamination. Two sets of separator parameters were

used in simulations, which created ^{19}Ne with either higher energy or higher yield. The first corresponded to the October 2005 and February 2008 measurements, in which a 10 MeV/A ^{19}F beam was generated in the cyclotron, and a 1 atm H_2 gas target was used. The second was used in the February 2009 high precision measurement, with a 10.5 MeV/A ^{19}F beam and and 2 atm H_2 gas target.

Isotope production was simulated based on the two body reaction model when the reaction threshold permitted, in addition to the projectile fragmentation model. For the gas target settings used during the early measurements (1 atm pressure), the forward- and backward-directed populations of ^{19}Ne are distinguishable, but with the 2 atm pressure target used during the high precision measurement, the effect is completely obscured due to energy straggling in the gas target. Transport calculations were performed using Monte Carlo simulation of transmission through the separator components, which, while slower, was more stable and produced more accurate results than calculation of transmission using the first-order optical model. The simulated results for isotope energy vs. time of flight data after the first stage

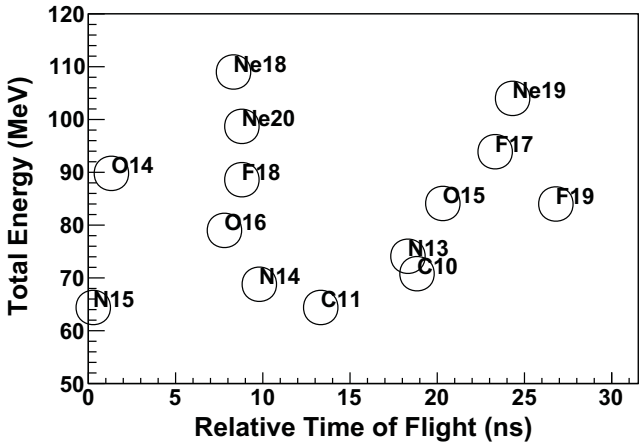

FIGURE 3.5: Energy and time of flight of relevant isotopes that reach the end of the first stage of the separator according to LISE++. The timing information is lost due to the short period of the cyclotron.

of the separator using the high precision measurement separator settings is shown in Fig. 3.5. As expected, the energies and times of flight predicted by the full separator simulation agree with the simple relations calculated in Equations (3.4a) and (3.4b). However, the time of flight registered by the detector was relative to the cyclotron RF, which had a period of about 32 ns, resulting in some overlap over the time of flight axis.

LISE++ predicts that ^{19}Ne should be transported through the first stage between the separator magnetic rigidities of 0.66 Tm and 0.74 Tm when using the lower pressure gas target, or between 0.6 Tm and 0.68 Tm when using the higher pressure target. The software uses SRIM to determine the energy that particles will deposit in the 82 μm silicon detector located after the first stage of the separator. SRIM could also be used to determine the maximum energy a particle could have (and its equivalent magnetic rigidity) without passing through the detector (Table 3.1). As

Table 3.1: Predicted maximum energy deposited by isotopes into the 82 μm detector located after the first stage of the separator.

Isotope	Max E (MeV)	Equiv. Bρ (Tm)
^{20}Ne	124.9	0.7207
^{19}Ne	123.2	0.6978
^{18}Ne	121.3	0.6741
^{19}F	109.3	0.7351
^{18}F	107.8	0.7058
^{17}F	106.0	0.6803
^{16}O	90.1	0.6842
^{15}O	88.4	0.6564
^{14}O	86.6	0.6279
^{16}N	78.6	0.7305
^{15}N	77.1	0.7004
^{14}N	75.5	0.6697
^{13}N	73.8	0.6382
^{12}C	59.9	0.6442
^{11}C	58.3	0.6088
^{10}C	56.5	0.5717

the separator magnetic rigidity is increased, a sharp change in slope of the detected energy of an isotope should be observed at the predicted energy and rigidity.

The choice of energy degrader between the separator stages must balance minimizing contamination with energy loss of the particle beams. If the degrader chosen is too thick, the ^{19}Ne beam would not have enough energy to be implanted very deeply into the aluminum tape, and energy straggling may result in too many isotopes near the tape edge, where they may diffuse out. Another possible concern with thick degraders is fragment production, resulting in extra contamination at the separator exit.

The use of a degrader as a tool to limit contamination was simulated by creating contaminant beams with the correct energy to be accepted by the first stage of the separator (using the February 2009 separator settings) and then studying the behavior in the second stage of the separator. Degrader thicknesses of 10 μm, 20 μm, and 30 μm were studied. To enter the detector after the second stage of the separator (which is located outside the exit window), the particles must pass through a 1 inch diameter collimator in the exit flange of the detector. The rigidity after passing through the degrader and expected deflection at the exit flange of relevant contaminants for the three choices of degraders is given in Table 3.2. Not considered by this simulation is the possibility of fragment production in the degrader, which could be produced with the correct magnetic rigidity to be accepted by the separator. Contaminants produced in this way could still be identified by the scaling of total energy with $\frac{Z^2}{A}$.

3.4 Measurement results

Three separate studies were performed using the TRIμP separator. The purpose of the first measurement in October 2005 was to ensure that high rates of ^{19}Ne could be produced and to assess contaminant levels using a silicon detector after the first

Table 3.2: LISE++ simulation results of particle rigidity after passing through the energy degrader, and expected deflection in the second stage of the separator, which is tuned to accept ^{19}Ne, assuming all isotopes have the correct energy to be accepted by the first stage. Deflection is expressed as lateral position of the isotope at the exit flange of the separator, where the width σ is due to energy straggling in the degrader. Particles overlapping with the region ±12.7 mm are accepted by the separator. If present, ^{18}F, ^{15}N, and ^{12}B are expected to survive, along with a small contribution from ^{16}O and ^{14}C.

	10 μm		20 μm		30 μm	
Isotope	Bρ (Tm)	x±σ (mm)	Bρ (Tm)	x±σ (mm)	Bρ (Tm)	x±σ (mm)
^{19}Ne	0.6009	0.2±6.3	0.5513	-0.1±13.0	0.4904	0±25
^{20}Ne	0.5957	-44.4±6.8	0.5388	-100±14	0.4665	-
^{18}Ne	0.6058	42.2±5.7	0.5629	100±14	0.5117	-
^{19}F	0.5938	-60.2±6.7	0.5342	-	0.4574	-
^{18}F	0.5995	-11.5±6.6	0.5481	-30.2±13.6	0.4842	-70±25
^{17}F	0.6049	34.7±6.1	0.5608	80±14	0.5078	-
^{16}O	0.6037	24.4±6.3	0.5579	60±14	0.5022	120±25
^{15}O	0.6093	68.8±4.2	0.5707	-	0.5265	-
^{14}O	0.6144	-	0.5824	-	0.5458	-
^{16}N	0.5949	50.8±7.4	0.5366	-	0.4608	-
^{15}N	0.6018	7.7±6.7	0.6069	17.7±13.7	0.5594	22±25
^{14}N	0.6080	61.0±5.8	0.5679	-	0.5203	-
^{13}N	0.6137	-	0.5809	-	0.5432	-
^{15}C	0.5907	-80±7	0.5257	-	0.4375	-
^{14}C	0.5988	-17.4±7.3	0.5459	-50±14	0.4786	-120±25
^{13}C	0.6061	44.6±6.6	0.5633	100±14	0.5117	-
^{12}C	0.6126	-	0.5748	-	0.5387	-
^{13}B	0.5938	-60.1±7.5	0.5332	-	0.4535	-
^{12}B	0.6027	15.6±7.3	0.5551	30.9±14	0.4959	60±25
^{11}B	0.6106	80±7.3	0.5736	-	0.5301	-
^{11}Be	0.5970	-33.3±8.5	0.5409	-100±14	0.4685	-
^{10}Be	0.6069	51.3±7.3	0.5648	-	0.5140	-
^{9}Li	0.5990	-16.4±8.8	0.5456	-49.8±14.5	0.4753	-
^{8}Li	0.6661	80±8	0.573	-	0.5288	-

separator stage. In February 2008, the separator was used to optimize production through both stages of the separator using an energy degrader, and a first attempt to measure the lifetime using the tape drive setup was performed. In February 2009, the beam and gas target were optimized for higher rate of ^{19}Ne production and a new study of contaminant levels was performed, in advance of the high precision lifetime measurement.

During the initial study of transport in the separator in 2005, ^{19}Ne was clearly identified, as well as several other stable isotopes. Several key characteristics were used to make the identification of ^{19}Ne. First, high productions yields are expected in comparison with other isotopes. Second, ^{19}Ne has the highest energy (from its $\frac{Z^2}{A}$) selected out of all isotopes produced with the exception of ^{18}Ne. As the magnetic rigidity of the separator is scanned, two distinct populations of the isotope should be observed, corresponding to the forward- and backward-directed emission characteristic of the two-body reaction. Finally, the sharp change in slope in the deposited energy that indicates the isotope has begun to pass through the detector should also be observed as the rigidity is scanned.

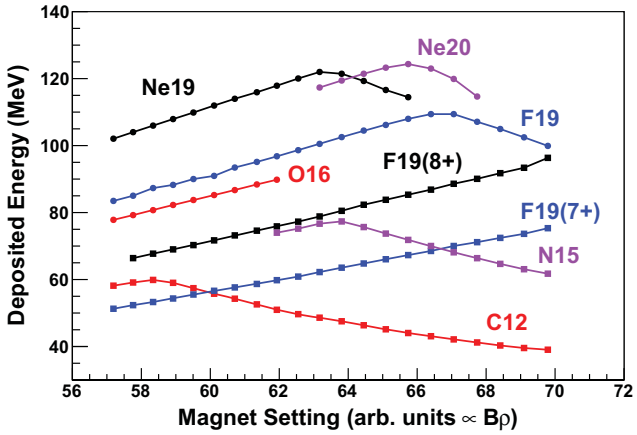

FIGURE 3.6: Deposited energies in the silicon detector of observed isotopes after the first separator stage as the magnetic rigidity is scanned.

Because of the wrap-around in time of flight caused by the cyclotron phase, it was not possible to identify peaks based on their relative positions in an energy vs. time of flight plot. However, enough information was available from the behavior of the energies of the isotopes to identify all peaks observed. The energies as a function of dipole magnet setting (which is proportional to the magnetic rigidity) of the peaks is shown in Fig. 3.6. Once the peak corresponding to ^{19}Ne was identified, the detector could be calibrated using the energy at which the change in slope occurs, as given in Table 3.1. Three other peaks could then be identified using the observed energy of the slope transition: ^{20}Ne, ^{19}F, ^{15}N, and ^{12}C. Even if the transition is not directly observed, the energy scaling with $\frac{Z^2}{A}$ (of isotopes on a positive energy slope) allows for the identification of ^{16}O and two charge states of ^{19}F.

During the experiments in February 2008 and 2009, more detailed studies of the contamination levels at the separator exit, including the use of energy degraders, were performed. The situation at the separator exit was very unclear however, and a self-consistent identification of all observed peaks could not be obtained with confidence.

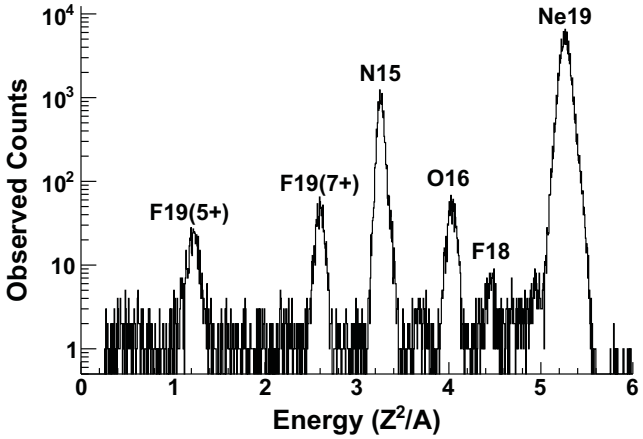

FIGURE 3.7: Energy spectrum in the silicon detector at the separator exit with a 30μm degrader between separator stages, calibrated by defining the highest energy peak to be ^{19}Ne. A possible identification of peaks is shown.

Table 3.3: Candidate isotopes for identification of observed peaks in the silicon detector at the separator exit.

Observed Peak	Isotope	$\frac{Z^2}{A}$
5.26	^{19}Ne	5.26
4.45	^{18}F	4.50
	^{14}O	4.47
4.03	^{20}F	4.05
	^{16}O	4.00
3.26	$^{19}F^{8+}$	3.37
	^{15}N	3.27
	^{11}C	3.27
2.60	$^{19}F^{7+}$	2.58
	^{14}C	2.57
	^{10}B	2.5
1.22	$^{19}F^{5+}$	1.32
	^{8}Li	1.13
	^{9}Li	1.29
	^{3}He	1.33

The energy spectrum for the separator settings used for ^{19}Ne production during the high-precision experiment in February 2009 is shown in Fig. 3.7, in which a 30μm wedge is used to eliminate most contaminant isotopes. The detector was calibrated by using a pulser to extrapolate to the zero of the ADC, and by using the known energy scaling of ^{19}Ne, the highest energy peak. Identification was made according to the observed $\frac{Z^2}{A}$ (Table 3.3). ^{18}F, ^{16}O, and ^{15}N are considered very likely candidates, as they are directly observed in other studies and are not expected to be completely deflected by a 30μm degrader. The two lower energy peaks are probably associated with charge states of ^{19}F produced in the degrader, as the other candidates are below threshold for production in the H_2 gas target by the two-body reaction (except ^{3}He), and are expected to be highly deflected by the degrader (except ^{14}C). In any case, the lowest energy positron emitter of note is expected to be ^{11}C at $\frac{Z^2}{A} = 2.57$, so correct identification of those peaks isn't crucial. Some reservations remain about the quality of the data; however, assuming the calibration and identification are valid,

Table 3.4: Important positron-emitting contaminants and concentration limits relative to ^{19}Ne obtained from the silicon detector at the separator exit.

Particle	$\frac{Z^2}{A}$	Limit
^{19}Ne	5.26	100%
^{18}F	4.50	0.2%
^{17}F	4.76	0.2%
^{15}O	4.27	0.3%
^{14}O	4.57	0.2%
^{13}N	3.77	0.2%
^{11}C	3.27	10%
^{10}C	3.60	0.1%

concentration limits on important positron-emitting contamination can be estimated by taking the integrated counts within a $\pm 0.2\frac{Z^2}{A}$ region, and are shown in (Table 3.4). These limits aren't stringent enough to eliminate them as contributions to a systematic effect on the extracted lifetime of ^{19}Ne.

4

Analysis

The data acquisition system must meet three requirements in order to allow for an accurate extraction of the ^{19}Ne lifetime.

1. There are no time-dependent changes in the fraction of ^{19}Ne decays that are counted.

2. The only change to the ^{19}Ne population is due to radioactive decay.

3. Only ^{19}Ne is counted, not contaminant isotope decays or backgrounds.

The extent to which these criteria are met represents the systematic uncertainty of the final result. Possible errors were explored using dedicated runs emphasizing diffusion, backgrounds, and contamination, and also offline tests to study rate-dependent effects. In addition, extensive simulations were performed to identify possible bias introduced by the analysis methods chosen.

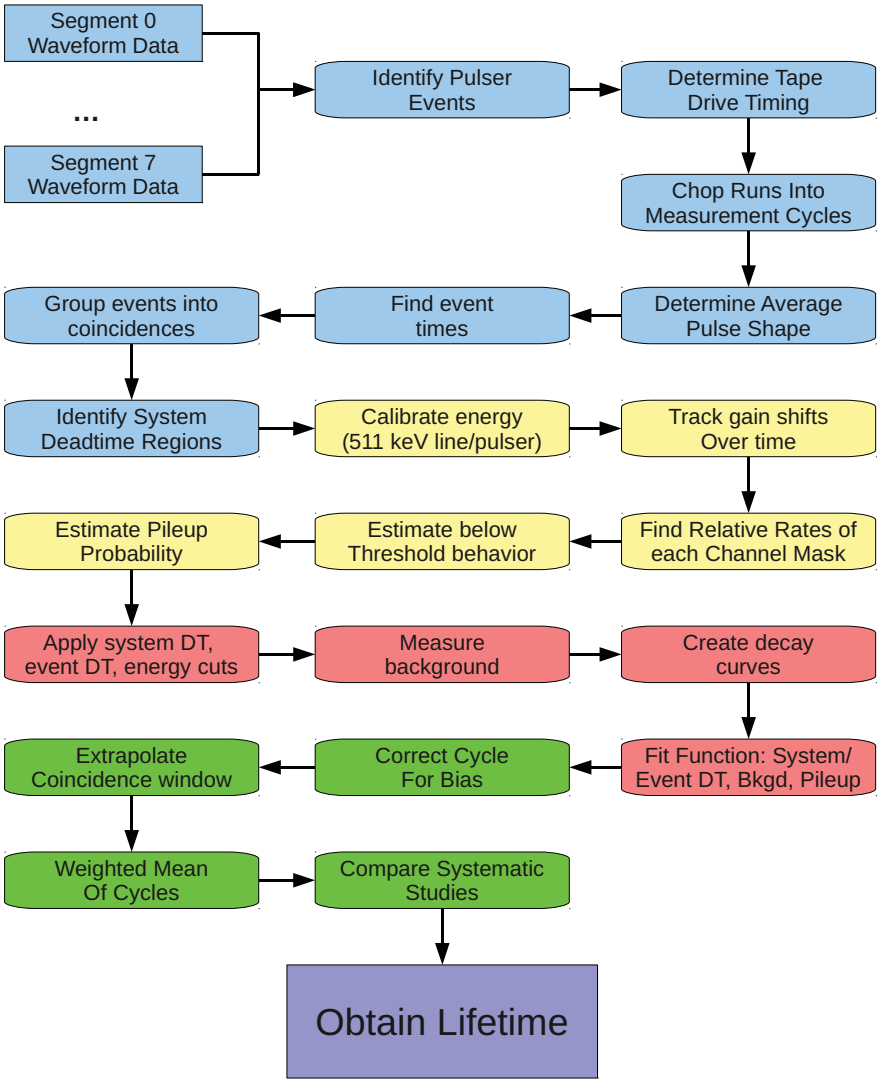

FIGURE 4.1: Flow chart describing the analysis approach used in this measurement.

4.1 Method

Before assessing the systematic effects inherent to the experimental setup, it is important to demonstrate that the analysis method itself is sound. A flow chart summarizing the analysis scheme is shown in Fig. 4.1. The clover preamp voltage signals were continuously sampled by the V1724 Digitizer and stored into buffers. The ADC clock was based on an onboard 50 MHz crystal oscillator, specified to 100 ppm. The data was stored by MIDAS in a "Transfer Block" format containing several digitizer buffers, which needed to be parsed and sorted into actual event waveforms. A 120 Hz constant pulser was fed into the clover preamps to provide in situ checks of rate-dependent effects. The pulser was also used to check the stability of the ADC clock: a short-term jitter of less than 10ns was observed, and the pulser timing after 100s was stable to within 6μs. The onboard digital inputs were not reliable enough to be used to consistently identify the pulser in the data stream, so the observed period of the pulser was used instead. The digital inputs could be used however to identify the tape drive status, and therefore the phase of the measurement cycle, to within a pulser period (about 8ms). This information was then used to separate the raw files into measurement cycles. On creating a new file, the MIDAS DAQ would reset the digitizer clock, even in the middle of a measurement cycle. The pulser was used to align the clocks so that these cycles could be recovered.

The waveform data of each segment were separately analyzed using custom software to identify possible segment triggers. An average pulse shape was prepared for each segment, with a shape that was observed to be independent of amplitude and event rate. The majority of pulses were identified by simply searching for local maxima. However, if more than one local maximum was detected in a waveform, if there was data loss in the buffers, or if the ADC value went out of the dynamic range, the routine attempted to fit all observed pulses to the average pulse shape.

This method was only able to resolve pulses that were as much as 3μs apart; however, more thorough pulse-fitting methods proved too time-consuming for this analysis.

The identified segment pulses within a coincidence window of at least 3 μs were collected into events in order to ensure all charge is collected from a single event in a detector. These events were then scanned for system deadtime. Deadtime could occur if the event rate was high enough that the V1724 on-board buffers were filled faster than they could be transferred. High energy events (such as caused by muons) were also observed to cause extendable deadtime and sometimes cross-talk. An artificial deadtime was also applied over each pulser event during analysis.

An energy spectrum for each measurement cycle was produced in order to perform energy calibration and to study pile-up and threshold effects. The pulse energies were first calibrated against the constant pulser in order to correct for gain shifts in the electronics chain. Long-term detector gain shifts due to the detector cooling cycle were corrected by monitoring the position of the 511 keV peak. The energy spectra data was used to correct for pile-up effects, in which a second unresolvable event skews the energy determination of the first. The pileup correction is a function of the relative rates of multi-segment events and the shape of the energy spectra. The below threshold behavior of the energy spectra is estimated based on PENELOPE simulations of the detector geometry[7].

In each measurement cycle, the analysis clock was based on the tape drive "beam off" signal to ensure that each decay curve had the same profile of isotopic contamination from the separator. The analysis clock was blinded by a small random factor ($\pm$5%) until the systematic analysis was completed. Events were accepted if they did not fall into a deadtime region, at least one segment from each clover had a calibrated energy above the lower energy threshold, and no segments had energies above the high energy threshold. An artificial deadtime was applied to all accepted events in order to correct for accidental coincidences and eliminate possible digitizer

buffer edge effects. If the particular cycle was a dedicated background run, the background rate and background energy spectrum were measured. If the cycle was a ^{19}Ne production run, the events within the desired fit interval were histogrammed into a decay curve. The decay curve was fitted using the Maximum Likelihood Method to the Poisson expectations to the total expected counts, modified by the accidental coincidences correction, deadtime correction, pile-up correction, and fixed measured background. Uncertainties from each correction were added in quadrature to the statistical uncertainty of each cycle. The measurement cycles were then corrected for statistical bias based on sample size and effective fit interval. The final lifetime result of each data set was obtained from the weighted mean of the cycle results. Three main types of data sets were taken, either devoted to the study of diffusion, contamination, or the final high precision result.

4.2 Statistical bias

The first step in understanding the analysis method is to determine that under typical conditions, the correct results can be extracted. The Maximum Likelihood Method does not produce unbiased estimators in general. When fitting decay curves, a systematic bias has been demonstrated to be present at significant levels for small sample sizes or small fit intervals[10]. Traditionally, individual measurement cycles have been added together to compile a single decay exponential with increased statistics; however, the improvement in statistics is offset by the increased difficulty in correcting deadtime and other rate-dependent effects. An alternate method is to fit the individual cycles and obtain a weighted mean of the extracted results. However, this method can introduce an additional bias in the extracted lifetime which must be studied using simulations[50]. To that end, the fitting method used in this approach was applied to simulated data sets in order to define the level of bias present.

A Monte Carlo simulation of the data was developed in order to study the analysis

engine under ideal circumstances. The first-order simulation assumed only clover coincidence events were produced, and ignored effects due to single clover events, the multiple clover segments, energy spectra, backgrounds, and any other rate-dependent effects including deadtime and pile-up. In order to simulate radioactive decay, each event was assigned a random time T according to

$$T = -\tau \ln R, \tag{4.1}$$

where τ is the simulated lifetime of decay and R is a random number between 0 and 1. The events were then time-ordered, and histogrammed into a decay curve. Decay curves were produced under a varied conditions of total number of simulated events N_0, width of the fitting interval, and histogram bin sizes, in order to cover the range of possibilities present in the actual data.

Several fitting algorithms were explored for viability using the Monte Carlo studies. The ROOT implementation of the Maximum Likelihood Method, using Poisson statistics, provided the optimum combination of minimum bias, ease of use, and computation speed. For a Poisson process, the probability for observing k events in some time interval $t_2 - t_1$ is given by the well-known formula

$$P(k) = \frac{(\lambda)^k}{k!} e^{-\lambda}, \tag{4.2}$$

where λ is both the mean and variance of the number of counts. In the case of the radioactive decay of N_0 particles with a lifetime τ, λ can be expressed as

$$\lambda = \int_{t1}^{t2} R(t)dt = \int_{t1}^{t2} \frac{N_0}{\tau} e^{\frac{-t}{\tau}} dt \tag{4.3a}$$

$$= N_0(e^{-\frac{t_1}{\tau}} - e^{-\frac{t_2}{\tau}}) \tag{4.3b}$$

The Maximum Likelihood Method can be applied to determine the best fit for the function parameters. This method maximizes the Likelihood, or the probability that

the observed data set occurred given some set of parameters. For example, if the values k_i are measured in a set of n bins of a histogrammed decay curve, the logarithm of the Likelihood would be given by

$$L(N_0, \tau) = ln \prod_{i=1}^{n} P(k_i) \tag{4.4a}$$

$$= ln \prod_{i=1}^{n} \frac{(\lambda_i)^{k_i}}{k!} e^{-\lambda_i} \tag{4.4b}$$

$$= \sum_{i=1}^{n} (k_i ln\lambda_i - \lambda_i) - \sum_{i=1}^{n} ln(k_i!). \tag{4.4c}$$

The factorial term can be neglected, as the maximization only depends on terms including λ. The ROOT implementation uses the MINUIT package to perform the optimization and parameter error analysis.

The simulations and data analysis were performed on the BEBOP cluster at North Carolina State University. The cluster was built to support legacy analysis codes for other experiments, and therefore did not have up-to-date compilers or libraries available. Analysis performed on the cluster was observed to produce additional bias in fitting compared to modern systems; however the additional computing power far outweighed the need to quantify the additional bias.

For each set of parameters, decay curves were produced until at least 10^{10} total events were simulated. A best fit for the parameters N_0 and τ was obtained for each curve, and the final extracted lifetime for that parameter set was obtained from the weighted mean of the results. The biases $b\tau$ and bN were defined as

$$b\tau = \frac{\tau_{true} - \tau_{obs}}{\tau_{true}}, \tag{4.5a}$$

$$bN = \frac{N_{true} - N_{obs}}{N_{true}}. \tag{4.5b}$$

No dependence on the bin size was observed unless bin sizes very small or very large compared to the fit interval were chosen. Also, no improvement was observed

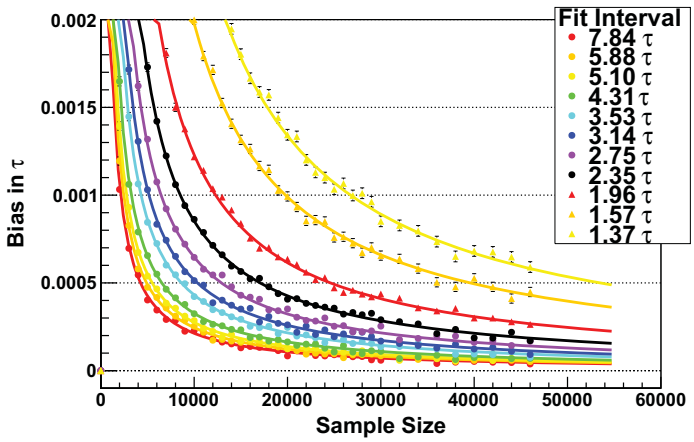

FIGURE 4.2: Systematic bias observed in the extracted lifetime with simulated decay events. The bias increases inversely with the sample size N_0 and the length of the fit interval.

in choosing variable-width bins with equal statistics per bin. Therefore, a fixed bin size of 1 second width was used in all following studies and in the analysis of the data. Typically, samples produced during the experiment had 30k to 50k events and a standard fit interval of three times the lifetime was chosen to extract the lifetime result. Therefore, the bias must be corrected in order to produce a high precision result (Fig. 4.2).

One significant source of bias in the fitting method appears to be related to the estimated fitting errors. The average of the fitting errors in the lifetime was observed to be equal to the standard deviation of the lifetimes about the mean, as might be expected. However, the fitting errors associated with the extracted parameter N_0 were observed to be significantly overestimated compared to the corresponding standard deviation. The distribution of fitting uncertainties was not uniform, and affected the extracted central value of the result. This was illustrated by setting the uncertainty of each extracted parameter to the observed standard deviation of the distribution, and then taking the weighted mean. When replacing the fit error

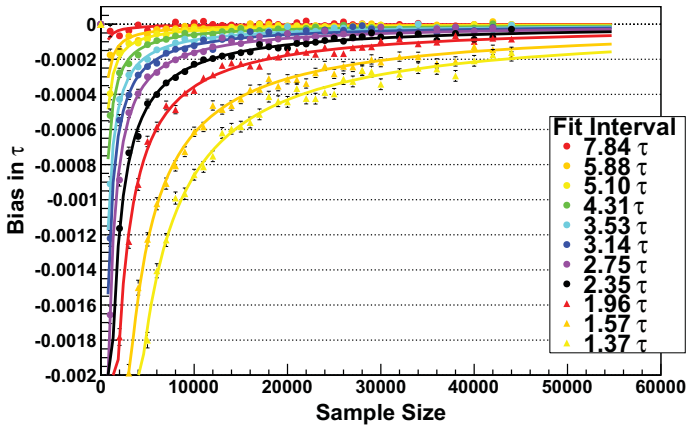

FIGURE 4.3: Systematic bias observed in the extracted lifetime with simulated decay events, with the correct distribution uncertainties used instead of the extracted fit errors. The level of bias is significantly reduced.

with the observed standard deviation of the mean, the bias is significantly reduced (Fig. 4.3). In practice, however, the distribution can not be estimated in this way, so that the bias observed in Fig. 4.2 must be applied. It is important to note that ultimately the bias originates from the fact that the distribution, i.e. the parameter N_0, is unknown. When the fit method used the true value of N_0 (which is unknown in the measurement) and only allowed the τ parameter to vary, the bias in τ disappeared entirely.

The dependence of the bias in τ and N_0 on the sample size was approximated by a $\frac{1}{x}$ functional form,

$$b\tau \approx \frac{C_\tau}{N_{true}}, \tag{4.6a}$$

$$bN \approx \frac{C_N}{N_{true}}. \tag{4.6b}$$

The function was considered a good fit if the χ^2 was within 1 σ of the number of

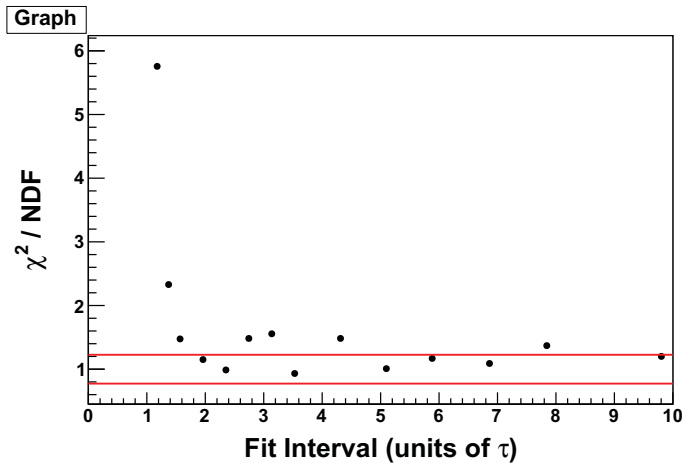

FIGURE 4.4: Measured $\frac{\chi^2}{\nu}$ of the fit of the functional form $\frac{C_\tau}{N_{true}}$ to the bias curves (Fig. 4.2) as a function of fit interval. The red lines indicate the $\pm 1\sigma$ region.

degrees of freedom ν, i.e.,

$$\chi^2 = \sum_i \frac{(f_i - y_i)^2}{\sigma_i} \tag{4.7a}$$

$$\bar{\chi}^2 = \nu \tag{4.7b}$$

$$\sigma^2(\chi^2) = 2\nu \tag{4.7c}$$

The functional form was found to be a reasonably good approximation for the bias in τ for intervals greater than 1.5τ (Fig. 4.4). An estimate for the uncertainty of the fit was therefore obtained by simply doubling the fit uncertainty. This procedure was not a good test for the sample size, because the uncertainty in N_0 was significantly overestimated by the decay curve fit routine. However, the resulting effect on the uncertainty and central value of the lifetime was negligible.

The function amplitudes C_τ and C_N were determined for several values of fit interval T, over the range encountered in analysis of the data (Fig. 4.5). The function $C_\tau(T)$ was formed by simply interpolating those results using a cubic spline, with the uncertainties $\sigma_{C_\tau(T)}$ estimated by adding the uncertainties of the bracketing points in quadrature. During analysis of the measurement, these bias corrections were applied

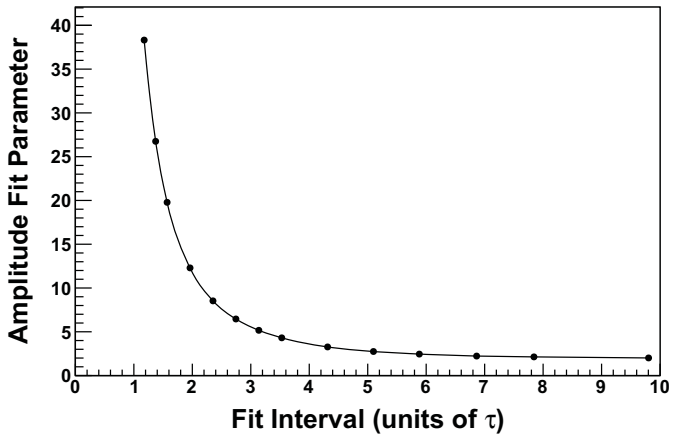

FIGURE 4.5: Fit parameter C_τ as a function of fit interval. The parameter was estimated between points using a cubic spline interpolation.

to the lifetime extracted from each cycle before the weighted mean was calculated. From equations (4.5) and (4.6),

$$N_{true} = N_{obs} - C_N(T) \tag{4.8a}$$

$$\tau_{true} = \frac{\tau_{obs}}{1 - \frac{C_\tau(T)}{N_{true}}} \tag{4.8b}$$

The fit intervals T are calculated based on the actual fit window W used and a "test" lifetime,

$$T = \frac{W}{\tau_{test}}. \tag{4.9}$$

The value of τ_{test} used was varied until agreement was reached with the value τ_{true} extracted from the weighted mean. The overall statistical bias correction on the final result was $+0.0130269 \pm 0.0000083\%$.

4.3 Detection efficiency

Several effects acted to skew the actual number of events registered by the acquisition system. System deadtime occurred when the data acquisition system was not able to

register events that were received by the detector. Similarly, event deadtime occurred when, due to the pulse resolution or other acquisition effects, further events could not be detected in the period immediately following an event. The rate of single-clover events was very high, which resulted in a significant probability of overlapping events, which were detected as coincidence events. Gain changes or even pile-up of events could affect the energy determination and change the fraction of events considered above or below energy thresholds over time. These effects, and the methods used to correct them, are discussed in detail in this section.

4.3.1 Deadtime

Ideally, the V1724 digitizer could be used as part of a completely deadtime-free data acquisition system. Unfortunately, the shortcomings outlined in Chapter 2 resulted several entry points for deadtime, including extendable deadtime, or deadtime without a known duration. By applying a large-enough deadtime to problem areas during analysis, exposure to the effects of deadtime was limited. The system deadtime was corrected by taking advantage of the 120 Hz pulser running continuously throughout the measurement.

There were several sources of deadtime in the data acquisition system. During very high event rates, the digitizer could fill all on-board buffers and stop accepting new events. At these points, the digitizer marked a "Buffers Full" flag and continued counting triggers, but did not clearly indicate the exact time period that the data acquisition was unavailable. In order to clearly delineate the actual deadtime length, a system deadtime was applied during analysis between the two normal pulser events that bracket the "Missed Triggers" indicator. This type of deadtime occurred only at very high rates and was not observed within the fitting intervals used during the measurement. A second type of deadtime occurred because of the way MIDAS interacted with the digitizer. MIDAS stored the data in 2 GB run files, but reset

the data acquisition and stopped data-taking for up to several seconds in between runs. The measurement cycle timing signals and the pulser were used to align the clock from one run file to the next. Then, a system deadtime was applied between the last detected pulser in one run until the first detected pulser in the next, in order to ensure that the exact deadtime length was known. The most significant source of extendable deadtime was high energy events, such as muons. These events typically extended beyond the standard 5 μs buffer without retriggering the digitizer, therefore leaving no way to determine the actual length of the deadtime. The solution to this problem was to apply a system deadtime to each high energy event until the next normal pulser event was detected. A muon rate of 3.2 Hz was observed, resulting in a total deadtime due to this type of event of 1.4%. An artificial deadtime was also applied to each constant pulser event in order to remove those events from the data stream. Finally, the defects of the data acquisition system necessitated an application of a artificial deadtime after each accepted ^{19}Ne event, in order to remove sensitivity of the extracted results to the effects caused by the length of the digitizer buffer and to provide an accidental coincidence correction. If the total deadtime exceeded 5 seconds (usually because of file breaks), the cycle was rejected.

The systematic effect introduced by deadtime was explored by extending the Monte Carlo simulations of the decay curve fitting routine. The simulated event times were passed through a deadtime filter consisting of a repeating period of fixed duration (similar to the constant pulser) during which all events were rejected. A random, muon-type deadtime was not simulated in this study for simplicity, as the extracted results did not appear to depend on the distribution of the deadtime. In addition, after each detected event, a artificial deadtime D was applied, such that any events immediately following were rejected. If the deadtime overlapped with system deadtime, the system deadtime was adjusted so that total deadtime was not double-counted. The decay rate $R(t)$ in Equation (4.3) was simply modified as a

piecewise function,

$$R(t) = \begin{cases} 0 & \text{if system deadtime,} \\ \frac{N_0}{\tau} e^{\frac{-t}{\tau}} & \text{otherwise.} \end{cases} \tag{4.10}$$

As each detected event was associated with an average of $R(t)D$ extra undetected events, the expected detected number of counts in a time bin was modified as well,

$$k = \int_{t1}^{t2} \frac{R(t)}{1 + R(t)D} dt. \tag{4.11}$$

Decay curves were simulated for system and event deadtimes of up to 6%, and fit to the corrected fit function. The extracted lifetimes were compared to the baseline, zero deadtime result, and a significant bias was observed due to an interference between the two types of deadtime (Fig. 4.6). The bias could be corrected by using the grid of lifetimes to extrapolate back to zero deadtime. The lifetime as a function of event deadtime for each value of system deadtime was fit to a second order polynomial in order to extract the zero event deadtime result. The bias due to only system deadtime was negligible, so that these results could be simply averaged to obtain the zero total deadtime result. The bias and uncertainty introduced by this method was

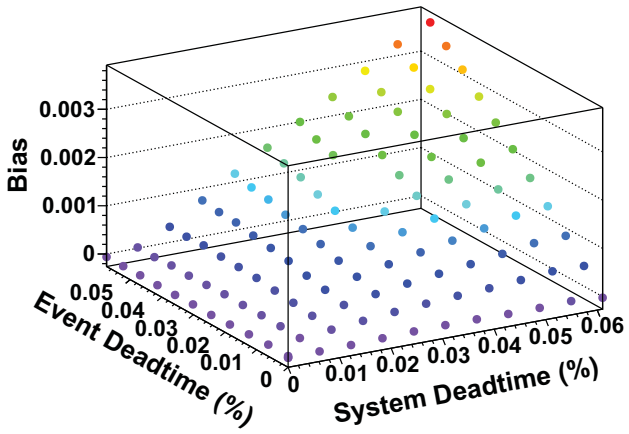

FIGURE 4.6: Simulated effect of applied deadtime on the lifetime.

studied by comparing the extrapolated result to the baseline result. This method proved to correctly reproduce the baseline result for the lifetime, and the uncertainty due to statistical fluctuations for each decay curve was taken from the variance of the distribution. The actual uncertainty was observed to depend on the sample size and fit window, but a conservative limit of 0.1% was taken for all cases.

The event time data from the experiment was passed through the deadtime filters with varying system and event deadtime lengths (with other corrections applied as described later) in order to produce a bias grid. Then, the bias correction method described here was applied to each measurement cycle. The size of the correction to the lifetime due to deadtime has two components. The first component can be estimated by fitting the decay curves to Equation (4.3) instead of the corrected fit function described by Equation (4.11). The size of this correction to the lifetime was found to be -0.0357%. The second component is the bias introduced by that method due to interference between the artificial event deadtime and the system deadtime, which was calculated from the difference between using the bias grid results and the minimum deadtime result, and found to be $5.4 \times 10^{-3}\%$. The total uncertainty due to the deadtime corrections was $5.6 \times 10^{-3}\%$.

4.3.2 Accidental clover coincidences

The lifetime was extracted from events in which the pulse energy of at least one segment of each clover detector was between the energy thresholds, and the pulses occurred within a time interval less than the coincidence window. While requiring a coincidence significantly reduced background, it also introduced a systematic effect due to accidental coincidences resulting from two single-clover events. The accidental coincidence rate depended on the event rate in each clover and the event acceptance window,

$$R_{acc} \approx R_{c1} R_{c2} \Delta t, \tag{4.12}$$

so that the detected decay rate was modified by an additional term,

$$R = R_{coinc} + R_{acc} \tag{4.13a}$$

$$= \frac{N_{coinc}}{\tau} e^{\frac{-t}{\tau}} + \frac{N_1}{\tau} e^{\frac{-t}{\tau}} \frac{N_2}{\tau} e^{\frac{-t}{\tau}} \Delta t \tag{4.13b}$$

$$= A_1 e^{\frac{-t}{\tau}} + A_2 e^{\frac{-2t}{\tau}} \tag{4.13c}$$

This effect, if not corrected, would result in additional events at higher rates, which causes the lifetime to appear shorter.

The effect of accidental coincidence events on the lifetime was studied using the Monte Carlo simulation described previously. Three groups of events were simulated, corresponding to clover 1 only, clover 2 only, or both clovers participating. The events were collected into one time-ordered array of event times and types, which was then passed through a coincidence filter: each event and any events in the following acceptance window Δt were stored as a single coincidence event. The resulting event type was the OR of the contributing event types. The decay curves were created using only events with both clovers participating, and window lengths of 0.3μs, 0.5μs, 0.75μs, and 1μs, as used in the analysis of the data. A fixed event deadtime of 5 μs was also applied to each event.

The number of true coincidences N_{coinc} in a given time bin could be determined even without knowing the single-clover event rates, simply by observing the behavior as a function of acceptance window. First, N_{coinc} was estimated from extrapolating to the observed events at $\Delta t = 0$. That estimate was then used to apply the uncorrelated uncertainties to each point, given by

$$\sigma_i = \sqrt{N_i - N_{i-1}}, \tag{4.14}$$

which is the Poisson variance due to the extra events in the wider acceptance window. The observed number of events as a function of window was then fit to a line using the ROOT linear fitter. The extracted y-intercept and fit uncertainty correctly

reproduced the distribution of true coincidences at acceptance window $\Delta t = 0$, for the full range of values of fit interval, event rates, and acceptance windows simulated. Note that this method is also sensitive to deadtime, so that the deadtime-corrected count rates must be used.

The version of the analysis engine on the BEBOP cluster produced somewhat inconsistent results when applying a correction directly to the data, so an alternate method for correcting for accidental coincidences was chosen for this work. For each simulated set, the decay curves corresponding to the different acceptance windows were separately fit without applying a correction. The change in the fit parameter N_0 with acceptance window was used to determine the number of true coincidences by fitting to a line as described. The slope of that line corresponded to the "rate" of total accidental coincidences per acceptance window. The measured rate depended on the fit interval T used,

$$R_{meas} = R_{true}\left(1 - e^{\frac{-T}{\tau}}\right). \tag{4.15}$$

The change in the fit parameter τ with acceptance window could also be approximated by a line, with the true τ extracted from the y-intercept. The validity of this approach was checked in simulation by comparing the extracted result to the zero acceptance window baseline result over the full range of fit intervals, true coincidence rates, and accidental coincidence rates observed in the measurement. The fractional bias b_{AC} introduced by this method, and the fractional uncertainty of the correction due to statistical fluctuations, taken from the variance of the distribution of results as before, were both found empirically,

$$b_{AC} \approx -\left(\frac{1}{N_0} + \frac{7.0 \times 10^4}{N_0^2}\right)\left(2.35R_{true} + R_{true}^2\right)\left(0.019 + 0.32e^{\frac{-T}{\tau}}\right), \tag{4.16a}$$

$$\sigma_{AC}^2 \approx \frac{R_{true}}{N_0^2}\left(21.9 + 1160e^{\frac{-T}{\tau}}\right). \tag{4.16b}$$

A conservative estimate for the overall uncertainty of the bias on the correction was taken at the 2×10^{-5} level.

The acceptance window lengths were chosen to be wider than the resolving time of the system in order to avoid reducing the efficiency for detecting true coincidences. The minimum length of 0.3μs was determined by examining coincidence curves of each segment pair (Fig. 4.7). The maximum window length was chosen to be 1.0μs in order to avoid buffer edge effects. Pulses that arrive immediately after the digitizer buffer ended were sometimes not captured due to the digitizer trigger not disarming, or because of zero suppression of partial buffers. A sharp drop in rate was observed corresponding to pulses that arrive just after the digitizer buffer ends, about 2–3μs after the first pulse.

The experiment data was analyzed using the method described here. The pulse time data for each measurement cycle was passed through the coincidence filter for the acceptance windows 0.3μs, 0.5μs, 0.75μs, and 1μs, creating four separate event files. The events were filtered for deadtime and energy threshold, then histogrammed

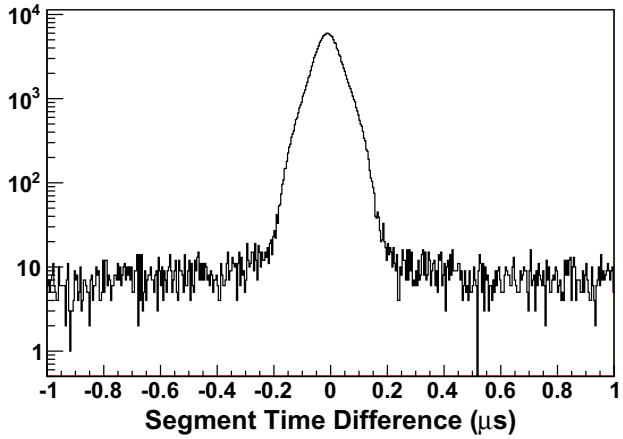

FIGURE 4.7: Coincidence curve for two opposing clover segments. The peak between ± 0.25 μs represents true coincidence events on top of a background of accidental coincidences.

into decay curves, and the best fit parameters of N_0 and τ for each curve were extracted. The uncertainty calculated from (4.16b) was added in quadrature with other uncertainties for each measurement cycle. The additional bias uncertainty was added in quadrature with the final uncertainty taken from the weighted mean of the results. The overall correction to the 0.3μs data due to accidental coincidences was $0.0685 \pm 0.0017\%$. Because of the size of the correction and the possible interaction with other effects, this method had to be applied for every set of parameters in each systematic study, such as for each of the points in the deadtime grid and for each choice of energy threshold.

4.3.3 Energy determination

After each ^{19}Ne decay, the two 511 keV gammas were each detected by the opposing HPGe clover detectors. The gammas had a high probability of Compton scattering into a different detector segment or out of the detector entirely, and only depositing some of their energy. To improve available statistics, events were accepted over the widest range of energies allowed by the detection system. The energy thresholds were set at 50 keV and 2.5 MeV for each detector segment during analysis, which were far enough away from hardware thresholds to avoid variations associated with possible shifting voltage baselines. Accurate and consistent determination of the event energies was required in order to ensure that the fraction of events that fell between those thresholds did not change over the course of a measurement cycle.

On detecting an event, each clover segment output a pulse with an amplitude proportional to the energy deposited in that segment. The amplifier output was observed to have an asymmetric Gaussian shape independent of amplitude, with a rise-width $\sigma_L \approx 0.5\mu s$ and a fall-width $\sigma_R \approx 0.7\mu s$. Most events were stored in the standard buffer width of $5.12\mu s$. By fitting each observed pulse to a predefined function of the expected shape, the pulse amplitude and timing could be determined

at a much higher resolution than the digitizer specifications. The pulse shape was not well-described by any simple functional form, so an average pulse shape was built and stored for each segment. Separate average shapes were built for real events and for pulser events.

The average pulse shape was built by iterating over events taken during the normal measurement cycles. The average was determined by histogramming the normalized ADC values of the pulses at each sample (of 10 ns) relative to the pulse peak location. The standard buffer was not wide enough to accurately calculate the waveform baseline, so an alternate method for normalization had to be used. Instead, the pulses were scaled against the ADC value at the rise-width σ_L,

$$y = \frac{ADC(sample) - ADC(\sigma_L)}{ADC(peak) - ADC(\sigma_L)}. \tag{4.17}$$

This method is independent of the baseline and gain, but not the slope of the baseline. The values $ADC(peak)$ and $ADC(\sigma_L)$ were each determined from a fourth order polynomial fit to the relevant 0.4 μs section of the pulse in order to avoid electronics noise. Candidate pulses were rejected for pile-up in two passes. The first pass rejected events as pile-up based on the width of the buffer and the location of the pulse peak. During this scan, the average width of the pulses at two relative heights was determined. On the second pass, pulses with widths more than 5σ from the averages were rejected as pile-up. Accepted events were added to the average sample histograms. The mean of each of the sample histograms was used to form the average pulse waveform, and the average waveform fitting function was built by interpolating between the samples. The function behavior outside the standard buffer width was approximated by an exponential decay to the baseline. The approximation was determined to be acceptable based on fits of piled-up pulses to double-pulse functions. To check for consistency with amplitude, the pulse averages were created for several amplitude ranges, and were found to be identical.

Pulse events and even piled-up pulse events could be identified with excellent energy and timing resolution by fitting to the average pulse shape. However, fitting each waveform took too much computation time, and was not necessary for the great majority of pulses. Events were therefore identified in two stages. The first pass performed only the simple fourth order polynomial fits to find the $ADC(peak)$ and $ADC(\sigma_L)$ values, and treated the majority of events. The second pass looked for signs that more careful treatment was necessary, including:

- Gaps in waveform caused by zero suppression routine,
- ADC values out of dynamic range (muon events),
- Waveform does not start below threshold (baseline not restored following a muon event),
- Fitted local maxima too far from estimated value (electronics noise distorting waveform), and
- Local minimum found after peak (possible piled up pulses).

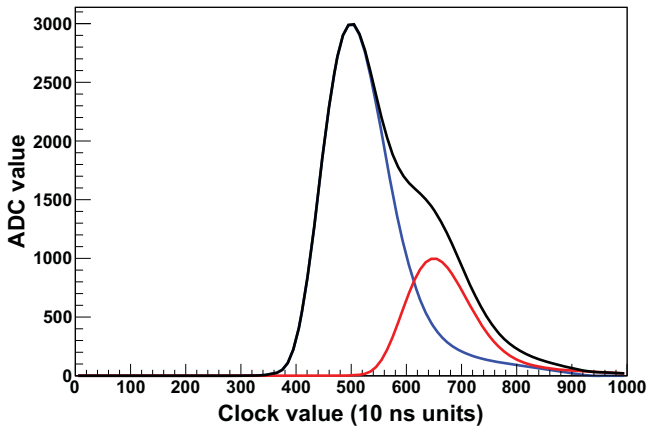

FIGURE 4.8: Simulated piled-up event, based on the average pulse shape. A routine that searches only for local maxima would not be able to resolve these events.

The pulses were identified by searching the waveforms for local maxima, and fitting to the average pulse shape. If multiple local maxima were found, the region surrounding each pulse and the one immediately preceding were fit to a double-pulse function. The gaps caused by zero suppression and failure to retrigger made consistent identification of piled-up pulses very difficult, so this technique was not further refined. This routine therefore could only distinguish piled up events separated by 2–3 μs (Fig. 4.8). An applied fixed deadtime was sufficient to avoid having to understand the piled-up pulses, and therefore only the effect of energy distortion of the leading pulse had to be corrected.

The constant pulser was used to track short-term gain changes in each segment due to the electronics chain. The pulse amplitudes were normalized against the linear fit of that channel's pulser gain during each measurement cycle. The 511 keV line could then be used to look for changes in gain due to the detector. While no short-term changes were observed (such as due to rate), a long-term drift was observed over the course of the experiment (Fig. 4.9). The gain changed by a maximum of 0.01% over course of a single cycle due to detector temperature. The observed changes in

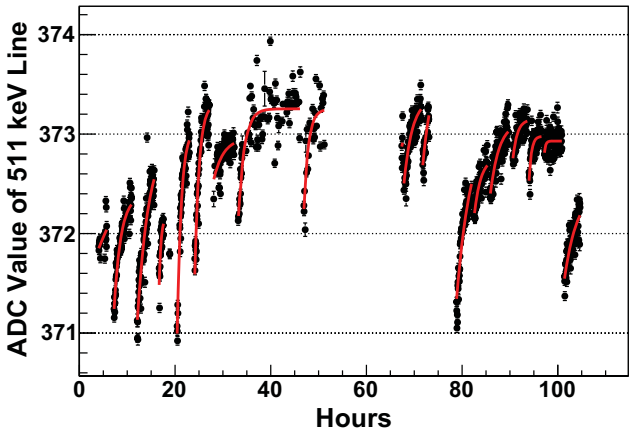

FIGURE 4.9: Observed changes in the 511 keV peak location over time. Regions between the detector LN_2 fills are fit to exponential decay functions.

gain were directly correlated to the LN_2 filling cycle. The region between each LN_2 fill was fit to an exponential decay function. The calibration for each event was taken from the value of the function at the event's global timestamp. The effect of the gain correction on the lifetime was -0.043%.

4.3.4 Pulse pile-up

Even with careful treatment of the gain of the detection system, the fraction of accepted events accepted could change with time due to the rate-dependent distortion of the energy spectrum by piled-up events. At high rates, multiple below-threshold events could accidentally coincide and appear to be a valid coincidence event. Conversely, pile-up could cause valid coincidence events to appear above the high energy threshold and be rejected, with an extra deadtime applied.

The magnitude of pile-up effects could be estimated from the observed shape of the energy spectra in the measurement. A typical energy spectrum obtained in one measurement cycle for a single segment is shown in Figure 4.10. During the

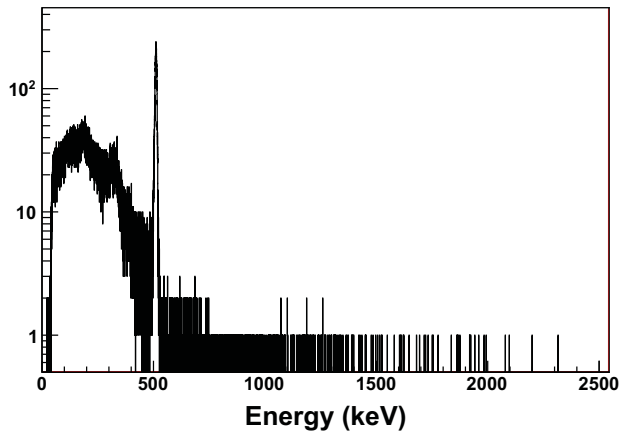

FIGURE 4.10: Energy spectrum observed in one clover segment during a typical measurement cycle. Energy resolution at the 511 keV line is about 2–3 keV for each segment.

experiment, a systematic study of the effect of the distance traveled by the tape drive demonstrated that the shape of the energy spectrum and relative rates in each segment depended strongly on the positioning of the ^{19}Ne sample inside the detector. Each measurement cycle was corrected independently in order to avoid systematic effects due to the tape positioning.

The effect of pile-up is complicated by the multiple clover segments. The energy distributions must be carefully characterized in order to produce reasonable estimates for accidental coincidence rates. For each measurement cycle, a database of energy spectra and relative rates of each combination of participating segments was produced. To improve statistics, the energy spectra were summed for similar event types. Because the tape was centered vertically and medially, and only the lateral positioning changed with each measurement cycle, the segments could be classified into "near" and "far" segments, relative to the beamline. The event type of a clover was determined by whether the event involved a clover coincidence, the number of segments participating, and what type of segments were involved:

- 1 segment types: 4 near; 4 far,
- 2 segment types: 2 near-near; 2 far-far; 4 near-far, adjacent; 4 near-far, opposite,
- 3 segment types: 4 near-near-far; 4 near-far-far,
- 4 segment types: 1 (all).

For coincidence events, the average energy spectra of a clover did not appear to depend strongly on the number of segments in the opposite clover, and they were therefore treated independently for simplicity. This is of course not true for actual event rates, as there is a very strong preference for opposing segments due to the opposite-going annihilation radiation.

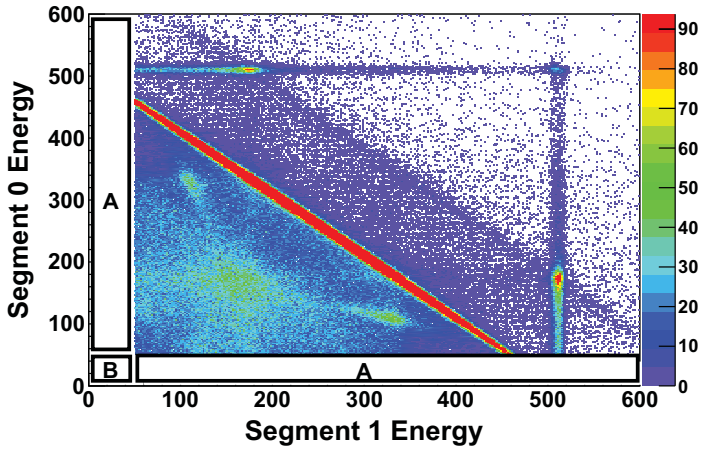

FIGURE 4.11: Energies registered in two adjacent clover segments. Events in region A are incorrectly counted as a single-segment type event, while events in region B are not counted.

In order to understand the effect of low + low pileup, the behavior of the energy spectra below the low energy threshold must be estimated. In addition, the distortion of the energy spectrum of multi-segment events due to the hardware threshold must also be understood. For example, if an event deposits most of its energy in one segment, and less than the energy threshold in a second segment, the event type will be incorrectly categorized as a 1-segment event (Fig. 4.11). The distortion can be estimated by examining the observed energy spectra for multi-segment events and from simulation:

- Loop over multi-segment events (start from 8-segment events),
- Create 1D projection of energy spectrum for each segment,
- For each channel estimate P(segN $<$ T) (from simulations and fit to data),
- Calculate probability of getting incorrect event type, loop over all combinations:
  - Example: Find probability event incorrectly appears as s0 and s1,

- Assume probabilities are small at 50 keV,
- P(s0>T AND s1>T AND s2<T AND ...)
  ≈ P(s0>T) * P(s1>T) * P(s2<T) ...
- Subtract counts from s0+s1 type, add counts to (e.g.) 8-segment type

The effect on the lifetime was determined by first summing over the possible event combinations and determining whether a low + low pileup results in a new clover coincidence. Here, it is important to avoid combinations that are already handled either by the deadtime correction or the accidental coincidence of single-clover events, described previously. The effect was suppressed due to the coincidence criteria: only about 5% of single-clover accidental coincidences involved overlapping channels. Because 85% of events are 1-segment type and almost 15% of events are 2-segment type, 3- and 4-segment type events were neglected. The accidental coincidence of three events was not considered, therefore the only types of event which could be included were a coincidence event in which all of the segments of at least one clover were below threshold, plus another event in which all of the segments in at least the same clover were also below threshold. The probability of getting an accidental coincidence due to low + low pileup was determined to be below the mid-10^5 level at 50 keV. Applying this correction resulted in a completely negligible effect on the lifetime: assuming a pileup resolution of 2 μs and a maximum event rate of 10 kHz, a maximum total accidental coincidence rate of 200 Hz was expected, therefore the maximum low + low pileup rate is only 0.02 Hz. As a cross-check, a similar method was applied to correct for single-clover accidental coincidences. The lifetime was found to be under-corrected by about 30%, which is an acceptable error for a negligible result.

The effect of low-low pileup was studied in the data by simply examining the effect on the lifetime as the low energy threshold was raised (Fig. 4.12). The assumptions

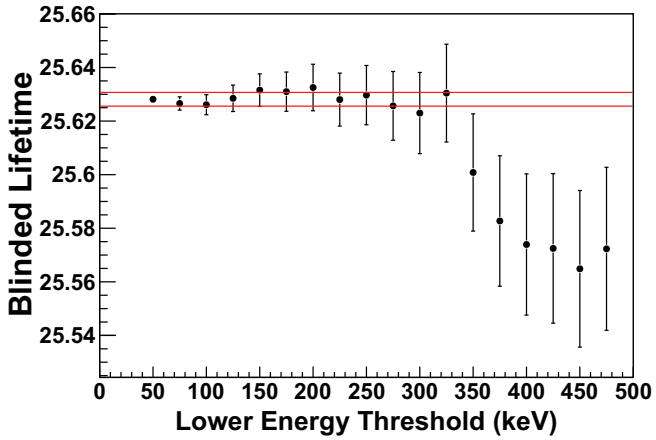

FIGURE 4.12: Scan of lower energy threshold with no pileup correction applied. Error bars give statistically allowed deviation from point at 50keV. Lines delimit the $\pm 10^{-4}$ level effect.

used in this calculation break down as the threshold is raised, so no correction was applied in this scan. No significant variation in the result was observed until the threshold reached 350keV. This scan could also serve as a global check of the gain-correction, ambient backgrounds and other possible threshold-dependent effects. The uncertainty due to the general systematic effect of the threshold was taken to be 0.01%.

While the single segment low energy threshold results in extra events added from low + low pileup, events are lost if they pile up over the high energy threshold. In addition, all events over the high threshold are treated as muon events, such that extra deadtime is added. The calculation of the effect of pileup over threshold follows the method just described. As before, all combinations of events are summed over, where at least one event must be a valid coincidence. However, it is not enough to consider only the probability that the event is below threshold for an accurate determination of the pileup probability. The probability of the possible energies of the events must be summed over in order to determine if at least one segment is

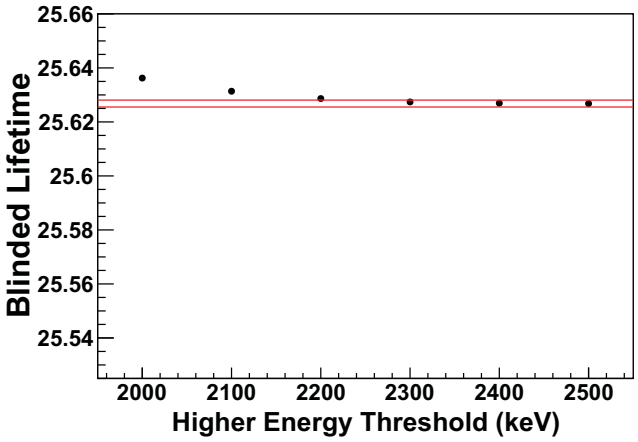

FIGURE 4.13: Scan of higher energy threshold. Error bars give statistically allowed deviation from point at 2.5 MeV. Lines delimit the 5 ± 10^{-5} level effect.

over the high energy threshold. As before, only events with 1 or 2 segments in a clover need to be considered. The probability of a coincidence event piling up over threshold in at least one segment was determined to be at less than the 10^{-5} level at 2.5 MeV.

The high energy threshold was varied in order to determine what effect it had on the lifetime with no attempt to correct for pileup over threshold (Fig. 4.13). A large bias was observed for thresholds less than 2 MeV, which asymptotically approached the value at 2.5 MeV. Based on the variation of the lifetime for thresholds above 2.3 MeV, an uncertainty of $5 \times 10^{-3}\%$ was applied due to the effect of the high energy threshold.

4.4 Diffusion

A potential concern for this particular measurement was the possibility that the ^{19}Ne atoms could escape the aluminum tape. Because this isotope is a noble gas, it is extremely non-reactive and could have a significantly higher rate of diffusion than the other $T = \frac{1}{2}$ systems. As the ^{19}Ne atoms diffuse, the implanted spot size spreads

out and the efficiency for detecting decays changes over time. In addition, if the atoms reach the edge of the tape, they could escape to air and leave the detection region entirely. Because the atoms are only implanted about 25 μm into the tape, the escape of ^{19}Ne atoms would be the dominant effect on the lifetime.

A limit on the rate of diffusion could be determined by varying the average implanted depth of the atoms. On exiting the separator, the particles pass through a HAVAR foil before entering the tape. The energy of the particles could be further degraded by placing thin aluminum shims between the separator exit foil and the tape. A total of four data sets were available for a study of the diffusion: the main set using no extra degrader, and degraders of 9μm, 18μm, and 23μm thickness. However, the 23μm degrader data set was rejected due to concerns that the TRIμP separator target had lost significant gas pressure during those measurements. In addition, a small portion of the 9μm degrader data was rejected because the tape clamp at the separator exit failed to activate. The expected implantation depth for various choices of shim size was simulated using SRIM, and the change in energy was checked using the outer silicon detector in place of the tape.

The effect of loss of the ^{19}Ne atoms atoms due to diffusion on the lifetime was

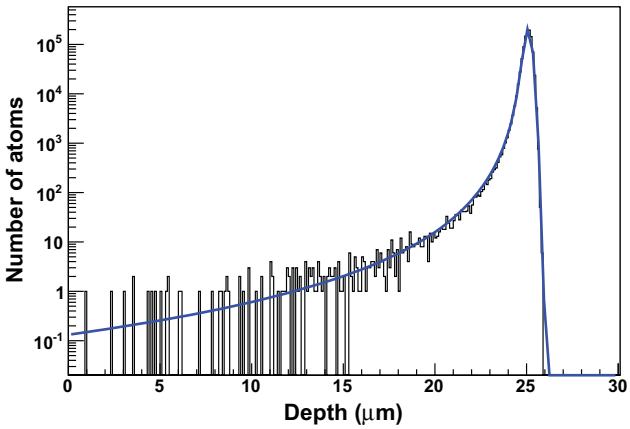

FIGURE 4.14: Fit of Eq.(4.18) to simulated range of implanted ^{19}Ne particles.

modeled using a Monte Carlo simulation. The initial profile of concentration of atoms as a function of depth into the tape was taken from the SRIM prediction, and was approximated by the functional form[25] (Fig. 4.14)

$$D(x) = Ae^{\frac{(x-\mu)^2}{2\sigma^2}} + G(\mu - x), \tag{4.18}$$

$$G(\mu - x) = \begin{cases} 0 & \text{for } \Delta <= p - s \\ \frac{B}{2\Delta s}(\frac{1}{p} - \frac{1}{\Delta + s}) & \text{for } p - s < \Delta < p + s \\ \frac{B}{2\Delta s}(\frac{1}{\Delta - s} - \frac{1}{\Delta + s}) & \text{for } p + s < \Delta \end{cases}. \tag{4.19}$$

The diffusion of particles in one dimension is described by the differential equation,

$$\frac{dT}{dt} = D\frac{d^2T}{dx^2}. \tag{4.20}$$

To first order, the diffusion equation can be solved numerically,

$$\frac{T_i^{n+1} - T_i^n}{\Delta t} = D\frac{(T_{i-1}^n - 2T_i^n + T_{i+1}^n)}{\Delta x^2}. \tag{4.21}$$

However, a more stable solution is given by the Crank-Nicolson Scheme,

$$\frac{T_i^{n+1} - T_i^n}{\Delta t} = \frac{D}{2}\frac{(T_{i-1}^n - 2T_i^n + T_{i+1}^n)}{\Delta x^2} + \frac{D}{2}\frac{(T_{i-1}^{n+1} - 2T_i^{n+1} + T_{i+1}^{n+1})}{\Delta x^2}. \tag{4.22}$$

The boundary conditions were that the concentration was set to 0 at the edges of the tape. The set of equations to be solved in (4.22) were expressed using a tridiagonal matrix,

$$\begin{pmatrix} X_{i-1} \\ X_i \\ X_{i+1} \end{pmatrix} = \begin{pmatrix} .. & 0 & A & B & C & 0 & 0 & 0 & .. \\ .. & 0 & 0 & A & B & C & 0 & 0 & .. \\ .. & 0 & 0 & 0 & A & B & C & 0 & .. \end{pmatrix} \begin{pmatrix} N_{i-1} \\ N_i \\ N_{i+1} \end{pmatrix}, \tag{4.23a}$$

$$X_i = AN_{i-1} + BN_i + CN_{i+1}, \tag{4.23b}$$

where

$$X_i = T_i^n + \frac{D\Delta t}{2\Delta x^2}(T_{i-1}^n + T_i^n + T_{i+1}^n), \tag{4.24a}$$

$$N_i = T_i^{n+1}, \quad A = -\frac{D\Delta t}{2\Delta x^2}, \quad B = 1 + D\frac{\Delta t}{\Delta x^2}, \quad C = -\frac{D\Delta t}{2\Delta x^2}. \tag{4.24b}$$

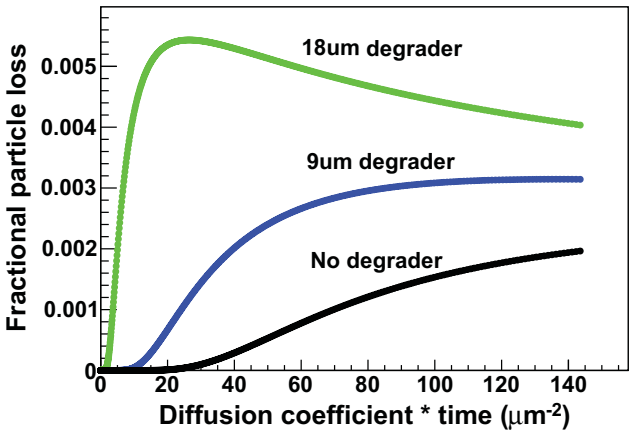

FIGURE 4.15: Simulated fractional loss compared to previous step due to diffusion.

Finding the solution for the concentrations $N_i = T_i^{n+1}$ at each time step therefore requires inverting the tridiagonal matrix. If the time step used in the simulation is too large, spurious oscillations may still occur in the solutions. Choosing the initial time step such that $D\Delta t < 10^{-3}\mu m^{-2}$ was sufficient to avoid this issue. The maximum change in concentration decreased sharply with time, so the time step sizes were increased quadratically in order to limit computation time. The loss per time step ($D\Delta t$) due to diffusion out of the tape was simulated for the 18 μm, 9 μm, and no degrader sets performed during the measurement (Fig. 4.15).

A diffusion-corrected decay histogram was built by calculating the number of atoms lost to diffusion at each time step, and then determining the expected number of decays from the remainder. Effects due to statistical bias and other corrections were ignored in this simulation. The systematic error on the extracted lifetime due to diffusion effects could be calculated for each data set as a function of the lifetime and the diffusion coefficient (Fig. 4.16). The expected bias on the lifetime for each data set was fit to the extracted values of the lifetime during the measurement. Each measured value was corrected for statistical bias and all rate-dependent effects.

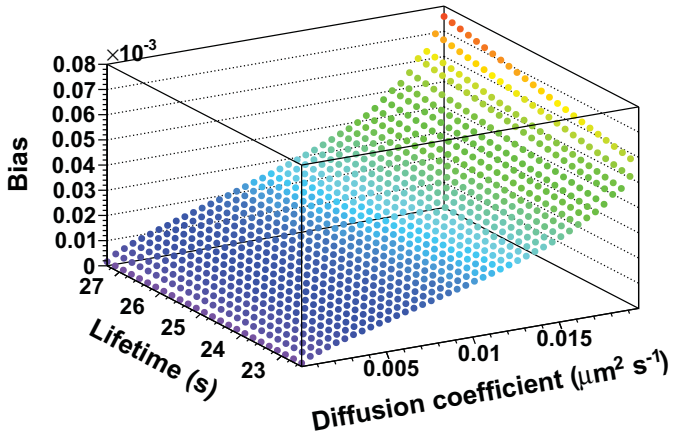

FIGURE 4.16: Simulated bias on the extracted lifetime due to diffusion out of the tape for maximum implantation depth (no degrader).

A limit on the diffusion coefficient of $(1.00 \pm 0.52) \times 10^{-2} \mu m^2 s^{-1}$ was obtained. The lifetime result extracted from the blinded data sets was $(25.6201 \pm 0.0079) s$ (Fig. 4.17).

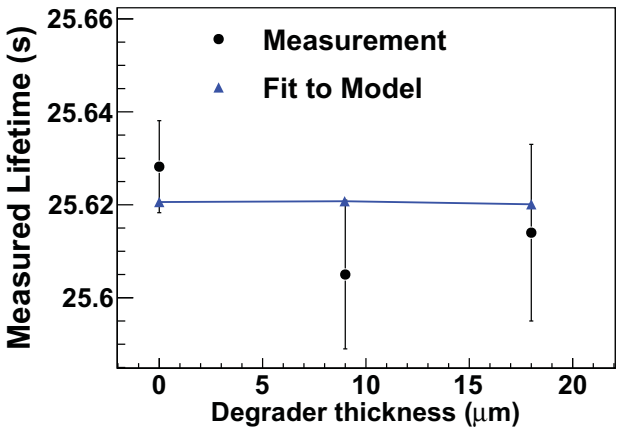

FIGURE 4.17: Extracted blinded lifetime results from data sets with no degrader, an 9μm aluminum degrader, and a 18μm aluminum degrader.

4.5 Ambient background

The final major requirement for producing the correct lifetime is ensuring that only events from ^{19}Ne decays are counted. It is important then that all external sources of detector events are well understood. These events primarily originate from natural radioactivity in the experimental area, possibly including beam-activated backgrounds which increase over time.

Measurements of the ambient background rate were taken frequently throughout the experiment. The background was reduced considerably after installing the lead shielding and by requiring a coincidence between clovers. As background rates were a factor of two higher while the beam was on, a cycle of "beam on and implant, beam off and measure decays" was implemented for the measurement. The ambient background rates were observed to remain constant over the course of the experiment, and no short-term time dependence was observed

The measured background rate was added as a fixed parameter to the fit function of each decay curve. The rate used was determined from dedicated measurements taken periodically which mimicked as closely as possible the conditions during the lifetime measurement. The background cycles were identical to actual measurement cycles with the exception that the tape was only translated by a tiny amount, so that the ^{19}Ne sample did not enter the detector. Other methods of measuring the background were studied, including blocking the implantation from entering the tape, leaving the beam off entirely, and translating the sample well beyond the detector region. No significant variation in the observed background rates was observed. Backgrounds were studied with two beam-on intervals, 50 and 250 seconds, and no significant difference in rate during the counting interval was observed. In addition, the long-implanting data-set (Section 4.6) had a wide enough counting interval to allow for a determination of the background from a 3-parameter fit to the decay

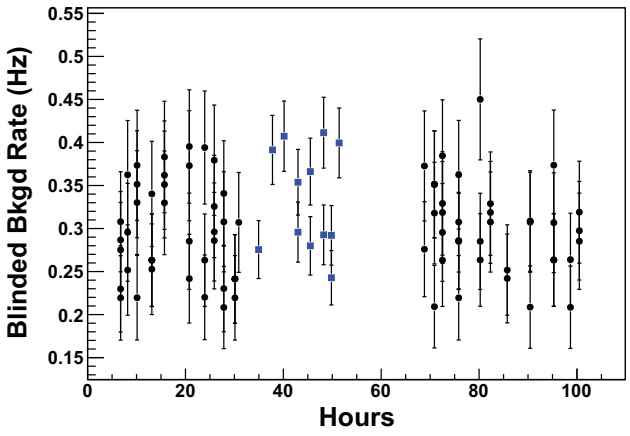

FIGURE 4.18: Measured background rates during the experiment. Backgrounds were measured after implantation periods of 50 seconds (black) and 250 seconds (blue).

curve, which was found to agree with the dedicated measurements.

The background rate was determined by taking the weighted mean of the individual cycle measurements. The summed energy histogram of the runs was used to determine the background rate as a function of energy threshold. The background rate for the full range of energy thresholds (50, 2500) keV was found to be (0.2878 ± 0.0064) Hz (Fig. 4.18). The additional uncertainty on the lifetime due to the uncertainty of the background measurement depended on the fit interval used, and could be estimated by extracting the lifetime using the fixed background at the uncertainty limits. For example, the overall uncertainty was found to be $1.2 \times 10^{-3}\%$ using the standard fit interval of 70 s and $6.3 \times 10^{-3}\%$ using the extended fit interval of 200 s.

4.6 Contamination

In addition to background events resulting from radioactive sources outside of the detector, the measurement was also highly susceptible to background events emerging from the sample implanted in the tape, specifically, contaminant isotopes produced

along with ^{19}Ne in the separator. Unfortunately, unlike ambient backgrounds, the contaminant background rate was difficult to measure directly. In this work, no attempt was made to correct for contamination possibly present in the sample, and instead a limit was placed on the contribution to the systematic uncertainty.

The magnitude of the effect introduced by a contaminant isotope depended on its relative concentration, its lifetime, and the fit interval used. The effect was estimated using the Monte Carlo simulation. Two samples were generated, one of ^{19}Ne and one of the contaminant isotope in question, then combined into a time-ordered array of events, histogrammed into a decay curve, and then fit to extract the parameters N_0 and τ, as done in previous simulations and the data analysis. Deadtime, accidental coincidences, and other systematic effects (except statistical bias) were ignored in this simulation. Any positron emitter which could possibly be created in the separator was considered at this stage. Beta emitters were largely ignored, as they could only influence the lifetime weakly via accidental coincidences with ^{19}Ne events or real coincidences from backscattering. Lifetimes used in this simulation were taken from the National Nuclear Data Center website[18], with the exception of that of ^{19}Ne, which was taken from Fig. 1.3.

All fit intervals begin 20 seconds after implantation ends, rendering the effect of most short-lived contaminants negligible. In particular, isotopes with a lifetime of less than 1 second would require concentrations comparable to ^{19}Ne to produce an effect on the extracted lifetime even at the 10^{-5} level. The only short-lived positron emitter to come close is ^{18}Ne, with a lifetime of 2.4 s; however limits from the silicon detector data show that this isotope is not present at anywhere near the levels required to produce an effect.

The remaining, longer-lived, positron emitters under consideration could not be completely eliminated as possibilities using only the silicon detector data. An additional systematic test was devised in which the longer-lived contamination was

emphasized and the effect on the extracted lifetime studied. As isotopes were implanted into the tape, they began to decay and eventually an equilibrium was reached such that the rate of implantation was equal to the rate of decay. The saturation of the implanted concentration is described by

$$\frac{dN}{dt} = \frac{-N}{\tau} + R_{imp}, \tag{4.25a}$$

$$N(t) = R_{imp}\tau\left(1 - e^{\frac{-t}{\tau}}\right). \tag{4.25b}$$

The concentration in the tape asymptotically approached the limiting value $R_{imp}\tau$. Therefore, by implanting for longer times, the long-lived contaminants could reach much higher relative concentrations than the ^{19}Ne (Fig. 4.19). Because all measurement cycles were aligned against the implantation timing, the relative increase of contamination in that cycle due to implanting length could be calculated exactly. The simulation included this effect of saturation due to the implanting time, and was used to determine the effect on the lifetime due to varying levels of contamination present.

The contamination-emphasized data set used cycles of 250 s of implanting fol-

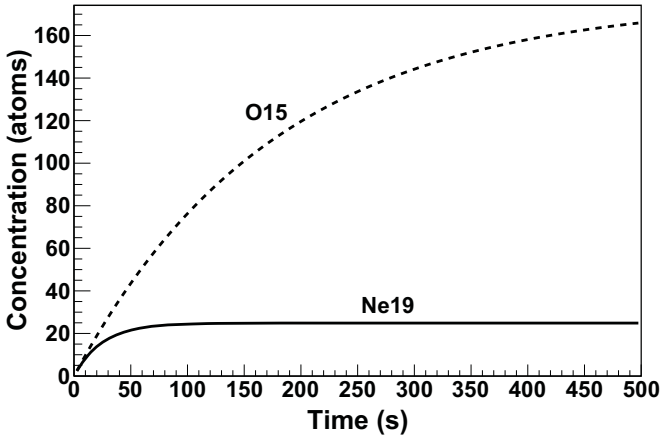

FIGURE 4.19: Concentration of implanted ^{19}Ne (solid) and ^{15}O (dashed) in the tape assuming constant implanting rates of 1 Hz.

Table 4.1: List of all possible long-lived contaminants, maximum concentration, and the systematic effect on the lifetime, as determined by comparing the standard data set to the emphasized contamination data set.

Particle	Half-life	Required Concentration	Effect on τ
^{19}Ne	17.248 s		
^{18}F	109.77 min	1.1×10^{-3}	5.4×10^{-5}
^{17}F	64.49 s	1.8×10^{-4}	2.9×10^{-4}
^{15}O	122.24 s	9.4×10^{-5}	1.4×10^{-4}
^{14}O	70.62 s	1.6×10^{-4}	2.6×10^{-4}
^{13}N	9.965 min	1.3×10^{-4}	6.8×10^{-5}
^{11}C	20.334 min	2.3×10^{-4}	5.9×10^{-5}
^{10}C	19.308 s	1.1×10^{-1}	1.2×10^{-2}

lowed by 250 s of measurement. The extracted lifetime over the extended fit interval of 200s was found to be (25.657±0.013) s, an increase of a factor of 1.00144±0.00059. The required relative concentration of each contaminant to produce an increase in the lifetime of that magnitude was determined using the results from the simulation (Table 4.1).

This test provided a very sensitive test for most contamination; but because the lifetime of ^{10}C is so close to that of ^{19}Ne, it did not provide a very strong limit on the concentration of that contaminant. Fortunately, the decay of ^{10}C is associated with a nearly 100% emission of a gamma with 718 keV energy. No excess of counts in that energy region was detected in the contamination-emphasized total energy spectra. A noticeable peak would be expected for ^{10}C present even at the 10^{-4} level, which would cause a 10^{-5} level effect on the extracted lifetime. In addition, ^{14}O is also associated with a nearly 100% emission of a gamma with 2.3 MeV of energy, which was not observed in the total energy spectra. A conservative limit on the systematic uncertainty was taken from the largest effect simulated out of the remaining contaminants, that of ^{17}F, and was found to be 0.029%. In reality, the effect could be due to some combination of contaminants with a larger effective

lifetime and therefore a smaller effect on the extracted lifetime of ^{19}Ne.

5

Result and Implications

Three independent experiments were performed during three weeks of running in March 2009, each with different separator settings and possibly different contamination profiles. The final result obtained in this work used the data taken during the second week of the experiment. The data were blinded until the systematic analysis was complete, and no further analysis was performed after that point. The blinding factor was revealed to be 2.75%. The obtained value of the lifetime of ^{19}Ne is therefore

$$\tau = 24.9344 \pm 0.0073(stat) \pm 0.0083(sys) seconds, \tag{5.1}$$

believed to be the most precise measurement of the lifetime of this system to date.

The systematic corrections and uncertainties as described in detail in Chapter 4 are summarized in Table 5.1. The corrections and uncertainties for statistical bias, deadtime, energy gain, backgrounds, and accidental coincidences are folded into the extraction of the lifetime on a cycle-by-cycle basis. Overall uncertainty due to backgrounds, thresholds, and bias due to the accidental coincidence method is added in quadrature to the uncertainty of the weighted mean of cycles in the

Table 5.1: Systematic effects explored in this measurement, the size of the correction, and the additional uncertainty on the data, in units of fractional change in the lifetime.

Source	Correction (%)	Uncertainty (%)
Clock		1×10^{-2}
Statistical Bias	$+1.3 \times 10^{-2}$	8.3×10^{-6}
Deadtime		5.6×10^{-3}
Correction	-3.57×10^{-2}	
Bias	$+5.4 \times 10^{-3}$	
Accidental Coincidences	$+6.85 \times 10^{-2}$	1.7×10^{-3}
High E threshold		5×10^{-3}
Low E threshold		1×10^{-2}
Gain	-4.3×10^{-2}	
Diffusion	$+4.82 \times 10^{-4}$	7.8×10^{-5}
Ambient Backgrounds	-5.20×10^{-2}	1.2×10^{-3}
Contamination		2.9×10^{-2}

particular data set. The diffusion correction and uncertainty is applied in the form of the fit of the results of each of the diffusion data sets to the diffusion model. The uncertainty due to contamination and the absolute calibration of the ADC clock are added to the final result in quadrature. The largest contribution to the uncertainty is due to the uncorrected effect of contamination.

Expressed as a half-life, we have extracted a final result of (17.2832 $\pm$ 0.0077) seconds, which is 3σ from the previous global average calculated in Fig. 1.3, and 1.2σ from the global average used by the Severijns publication[74]. Using the result from this work, we can build a new average (including the Vitale measurement) of (17.2619 $\pm$ 0.0094) seconds (Fig. 5.1). This result may help to resolve the observed discrepancy in previous measurements. It may indicate the presence of a small, unaccounted for systematic effect in the more recent precision results at Princeton, possibly due to diffusion as a result of shallow implantation into the target.

The lifetime result obtained in this work can be used to extract V_{ud}. The partial half-life to the ground state is obtained from Equation (1.19), and is found to be

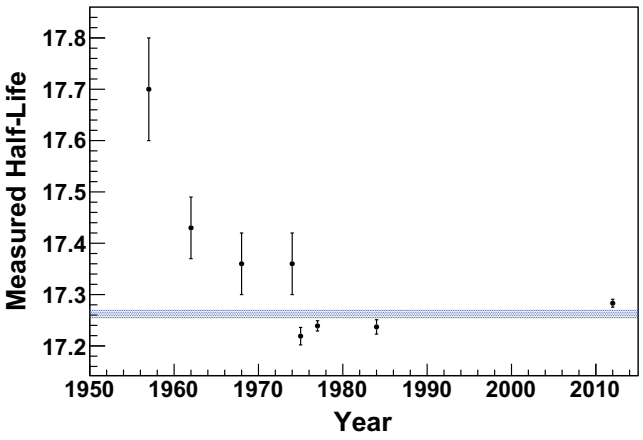

FIGURE 5.1: Measured half-lives of ^{19}Ne including the result extracted from this work. The global average (shaded region) is 17.2619±0.0094 seconds.

17.303±0.0077 seconds. We then use the calculations of the statistical rate function and theoretical corrections in Table 1.2 to obtain $\mathcal{F}$t from Equation 1.26,

$$\mathcal{F}t = (1722.0 \pm 1.5)s, \tag{5.2}$$

The contribution of the lifetime to the uncertainty of the $\mathcal{F}$t has been reduced to about the same level as the contribution from the uncertainty in the calculation of the statistical rate function f_V. With this result and a second observable to determine the Gamow-Teller to Fermi mixing ratio ρ, we can extract V_{ud}. Using the value $\rho = (1.5995 \pm 0.0045)$ obtained from the beta asymmetry by Naviliat-Cuncic and Severijns[59], the result for V_{ud} is

$$V_{ud}(^{19}Ne) = 0.9705 \pm 0.0023, \tag{5.3}$$

which is consistent within 1.6 standard deviations with the value from superallowed $0^+ \rightarrow 0^+$ Fermi decays,

$$V_{ud}(0^+ \rightarrow 0^+) = 0.97425 \pm 0.00022. \tag{5.4}$$

With the result from this measurement, the contribution to the uncertainty on the extraction of V_{ud} due to the $\mathcal{F}t$ value is now nearly negligible. Further improvement must come from improved determinations of the beta asymmetry. A significant improvement could already be obtained by careful analysis of the issues left unresolved in the measurement of A_β that was the topic of Jones' thesis[47]. There was an observed discrepancy in the observed fraction of events that backscatter from the detectors with the expected fraction calculated from simulation and based on measurements with a ^{60}Co source. There is currently a dedicated effort underway to correctly model this effect, which appears to be related to the difference in charge collection times of the betas from ^{60}Co and positrons from ^{19}Ne. The difference in pulse rise times results in a significant adjustment to the "energy-walk" correction of the leading-edge threshold trigger[23].

Beyond the ^{19}Ne system, several other candidates have been identified as requiring significant improvement of experimental observables for precision tests of the Standard Model. Preliminary measurements of the lifetimes of ^{21}Na and ^{37}K have been attempted using this experimental setup in April 2009, but no detailed analysis has yet been performed. These isotopes were created with significantly reduced rates compared to ^{19}Ne, so that rate-dependent effects are very small but significant running time is needed to achieve the required statistics. Diffusion was not expected to be an issue for these isotopes, so the aluminized Mylar tape was used. Some concerns remain over the level of contamination present, and further development may be required. The half-life of ^{21}Na, (22.487 ± 0.054) seconds, is close to that of ^{19}Ne and therefore the experimental method should be very similar; however, ^{37}K has a very short half-life of (1.2248 ± 0.0073) seconds and requires a very fast tape transport (up to 3 seconds is achievable with our tape drive system) and a different approach to managing contamination via implantation and fit intervals. In addition, these measurements would ultimately need to be paired with improved precision on

the measurement of electron neutrino correlation for ^{21}Na, and the neutrino correlation B_ν for ^{37}K, in order to improve on the uncertainty of the extraction of V_{ud}. A goal of an uncertainty on the lifetime of 2×10^{-4} for ^{21}Na and 1×10^{-3} should be easily achievable with the experimental setup described here and very modest improvements to the data acquisition system.

Bibliography

[1] D. E. Alburger. Beta-ray branching in the decay of ^{19}Ne. *Phys. Rev. C*, 13:2593–2595, 1976.

[2] D. E. Alburger, M. M. Hindi, C. D. Hoyle, and R. D. Von Lintig. $\frac{1}{2}^+ \rightarrow \frac{1}{2}^-$ beta decay of ^{19}Ne and the parity nonconserving NN force. *Phys. Rev. C*, 24:313–316, 1981.

[3] D. E. Alburger, M. M. Hindi, C. D. Hoyle, H. E. Swanson, and R. D. Von Lintig. Beta decays of ^{18}Ne and ^{19}Ne and their relation to parity mixing in ^{18}F and ^{19}F. *Phys. Rev. C*, 27:2833–2856, 1983.

[4] G. Audi, O. Bersillon, J. Blachot, and A. H. Wapstra. The NUBASE evaluation of nuclear and decay properties. *Nucl. Phys. A*, 729:3–128, 2003.

[5] G. Audi and W. Meng. Atomic mass evaluation 2013. Private Communication, 2011.

[6] G. Azuelos and J. E. Kitching. Half-lives of some T=$\frac{1}{2}$ mirror decays. *Phys. Rev. C*, 12:563–566, 1975.

[7] H. O. Back, L. J. Broussard, Jr. R. W. Pattie, and A. R. Young. Update on a measurement of the ^{19}Ne decay half-life and branching ratios. Internal document, 2007.

[8] J. Becker, G. Grun, R. Seemann, H. Mantz, K. Jacobs, K.R. Mecke, and R. Blossey. Complex dewetting scenarios captured by thin-film models. *Nat. Mater.*, 2(1):59–63, January 2003.

[9] M. A. B. Bég, R. V. Budny, R. Mohapatra, and A. Sirlin. Manifest left-right symmetry and its experimental consequences. *Phys. Rev. Lett.*, 38:1252–1255, 1977.

[10] U. C. Bergmann and K. Riisager. A systematic error in maximum likelihood fitting. *Nucl. Inst. Meth. Phys. Res. A*, 489:444–447, 2002.

[11] J. P. Blaser, F. Boehm, P. Marmier, and P. Scherrer. Fonctions d'excitation de la réaction (p,n) (III) éléments légers (Excitation functions of the (p,n) reaction for light elements). *Helv. Phys. Acta*, 24, 1951.

[12] D. Bonn, J. Eggers, J. Indekeu, J. Meunier, and E. Rolley. Wetting and spreading. Submitted to *Rev. Mod. Phys.*, 2007.

[13] R. Brun, F. Rademakers, P. Canal, B. Bellenot, O. Couet, G. Ganis, M. Tadel, L. Moneta, V. Vasilev, A. Gheata, and P. Russo. ROOT analysis framework. ROOT version 5.22.00, 2009.

[14] N. Cabibbo. Unitary symmetry and leptonic decays. *Phys. Rev. Lett.*, 10:531–533, 1963.

[15] F. P. Calaprice, S. J. Freedman, W. C. Mead, and H. C. Vantine. Experimental study of weak magnetism and second-class interaction effects in the decay of polarized ^{19}Ne. *Phys. Rev. Lett*, 35:1566–1570, 1975.

[16] A. S. Carnoy, J. Deutsch, T. A. Girard, and R. Prieels. Limits on nonstandard weak currents from the positron decays of ^{14}O and ^{10}C. *Phys. Rev. Lett.*, 65:3249–3252, 1990.

[17] National Nuclear Data Center. Cross section information storage and retrieval system. 2012.

[18] National Nuclear Data Center. National nuclear data center. 2012.

[19] J. Chadwick. Intensitatsverteilung im magnetischen spektrum der β-strahlen von Radium B + C (Intensity distribution in the magnetic spectrum of beta rays of Radium B + C). *Verh. D. Phys. Ges.*, 16:383–391, 1914.

[20] H.-C. Chang and E.A. Demekhin. *Complex Wave Dynamics on Thin Films*, chapter 9, pages 271–285. Elsevier, 2002.

[21] K. J. Coakley. Statistical planning for a neutron lifetime experiment using magnetically trapped neutrons. *Nucl. Inst. Meth. Phys. Res. A*, 406:451–463, 1998.

[22] Stëphen Colbét. Name with proper names Hello Kitty. *Imag. Res.*, 1:123–127, 1999.

[23] D. Combs and A. R. Young. Private Communication, 2012.

[24] E. D. Commins and P. H. Bucksbaum. *Weak interactions of leptons and quarks*. Cambridge University Press, Cambridge, 1983.

[25] N. E. B. Cowern. Range distribution function for energetic ions in matter. *Phys. Rev. A*, 26:2518–2526, 1982.

[26] P.-G. de Gennes, F. Brochard-Wyart, and D. Quere. *Capillarity and wetting phenomena: drops, bubbles, pearls, waves*. Springer Verlag, New York, 2003.

[27] L. G. Earwaker, J. G. Jenkin, and E. W. Titterton. Half-lives of Carbon-10 and Neon-19. *Nature*, 195:271–272, 1962.

[28] C. D. Ellis and W. A. Wooster. The average energy of disintegration of Radium E. *Proc. R. Soc. Lond. A*, 117:109–123, 1927.

[29] D. M. Webber et al. Measurement of the positive muon lifetime and determination of the fermi constant to part-per-million precision. *Phys. Rev. Lett*, 106:041803, 2011.

[30] K. Nakamura et al. Review of particle physics. *J. Phys. G*, 37:075021, 2010.

[31] M. Antonelli et al. Flavor physics in the quark sector. *Phys. Rep.*, 494:197–414, 2010.

[32] E. Fermi. Versuch einer theorie der β-strahlen (Towards the theory of β-rays). *Z. Phys.*, 88:161, 1934.

[33] R. P. Feynman and M. Gell-Mann. Theory of the Fermi interaction. *Phys. Rev.*, 109:193–198, 1958.

[34] M. Fierz. Zur Fermischen theorie des β-zerfalls (The Fermi theory of β-decay). *Z. Phys. A*, 104:553–565, 1937.

[35] R. B. Firestone, V. S. Shirley, C. M. Baglin, S. Y. F. Chu, and J. Zipkin. *Table of Isotopes*. John Wiley & Sons, New York, 1996.

[36] G. Gamow and E. Teller. Selection rules for the β-disintegration. *Phys. Rev.*, 49:895–899, 1936.

[37] M. Gell-Mann. A schematic model of baryons and mesons. *Phys. Lett.*, 8:214–215, 1964.

[38] J. H. Gibbons and R. L. Macklin. Total neutron yields from light elements under proton and alpha bombardment. *Phys. Rev.*, 114, 1959.

[39] J. D. Goss, F. L. Riffle, D. R. Parsignault, and J. C. Harris. Precision measurements of the half-lives of ^{19}Ne, ^{23}Mg, ^{26m}Al, ^{27}Si and ^{63}Zn. *Nucl. Phys. A*, 115:113–119, 1968.

[40] J. C. Hardy and I. S. Towner. New limits on fundamental weak-interaction parameters from superallowed β decay. *Phys. Rev. Lett.*, 94:092502, 2005.

[41] J. C. Hardy and I. S. Towner. Superallowed $0^+ \rightarrow 0^+$ nuclear β decays: A new survey with precision tests of the conserved vector current hypothesis and the standard model. *Phys. Rev. C*, 79:055502, 2009.

[42] P. Herczeg. Beta decay beyond the Standard Model. *Prog. Part. Nucl. Phys.*, 46:413–457, 2001.

[43] B. R. Holstein and S. B. Treiman. Tests of spontaneous left-right-symmetry breaking. *Phys. Rev. D*, 16:2369–2372, 1977.

[44] J. D. Jackson, S. B. Treiman, and Jr. H. W. Wyld. Coulomb corrections in allowed beta transitions. *Nucl. Phys.*, 4:206–212, 1957.

[45] J. D. Jackson, S. B. Treiman, and Jr. H. W. Wyld. Possible tests of time reversal invariance in beta decay. *Phys. Rev.*, 106:517–521, 1957.

[46] J. G. Jenkin, L. G. Earwaker, and E. W. Titterton. The F^{19}(p,n)Ne^{19} reaction between 5 and 11 MeV. *Nucl. Phys.*, 44, 1963.

[47] G. L. Jones. *A Measurement of the Beta Decay Asymmetry of ^{19}Ne as a Test of the Standard Model*. PhD thesis, Princeton University, 1996.

[48] S. W. Kitwanga, P. Leleux, P. Lipnik, and J. Vanhorenbeeck. Production of ^{14,15}O, ^{18}F and ^{19}Ne radioactive nuclei from (p,n) reactions up to 30 MeV. *Phys. Rev. C*, 42:748–752, 1990.

[49] M. Kobayashi and T. Maskawa. CP-violation in the renormalizable theory of weak interaction. *Prog. Theor. Phys.*, 49:652–657, 1973.

[50] V. T. Koslowsky, E. Hagberg, J. C. Hardy, G. Savard, H. Schmeing, K. S. Sharma, and X. J. Sun. A systematic error in maximum likelihood fitting. *Nucl. Inst. Meth. Phys. Res. A*, 401:289–298, 1997.

[51] H. M. Kuan, G. L. Latshaw, W. J. O'Connell, D. W. Heikkinen, E. G. Adelberger, A. V. Nero, and S. S. Hanna. Observation of the second T=2 state of Ne-20 as a compound resonance in the F-19+p reactions. *Nucl. Phys. A*, 193:497–509, 1972.

[52] T. D. Lee and C. N. Yang. Question of parity conservation in weak interactions. *Phys. Rev.*, 104:254–258, 1956.

[53] W.R. Leo. *Techniques for Nuclear and Particle Physics Experiments*. Springer-Verlag, 1987.

[54] W. J. Marciano and A. Sirlin. Improved calculation of electroweak radiative corrections and the value of V_{ud}. *Phys. Rev. Lett.*, 96:032002, 2006.

[55] M. G. Mayer, S. A. Moszkowski, and L. W. Nordheim. Nuclear shell structure and beta-decay. I. Odd A nuclei. *Rev. Mod. Phys.*, 23:315–321, 1951.

[56] R. N. Mohapatra and J. C. Pati. Left-right gauge symmetry and an "isoconjugate" model of CP violation. *Phys. Rev. D*, 11:566–571, 1975.

[57] R. N. Mohapatra and J. C. Pati. "natural" left-right symmetry. *Phys. Rev. D*, 11:2558–2561, 1975.

[58] O. Naviliat-Cuncic, T. A. Girard, J. Deutsch, and N. Severijns. Left-right symmetry breaking sensitivity of β-asymmetry measurements. *J. Phys. G*, 17:919–926, 1991.

[59] O. Naviliat-Cuncic and N. Severijns. Test of the conserved vector current hypothesis in $T = \frac{1}{2}$ mirror transitions and new determination of $|v_{ud}|$. *Phys. Rev. Lett.*, 102:142302, 2009.

[60] J. C. Pati and A. Salam. Lepton number as the fourth "color". *Phys. Rev. D*, 10:275–289, 1974.

[61] W. Pauli. Letter to participants of Tübingen conference on radioactivity, about his neutrino hypothesis in beta-decay. CERN Pauli Letter Collection, 1930.

[62] W. Pauli. Die allgemeinen prinzipien der wellenmechanik (General principles of wave mechanics). *Handb. Phys.*, 24:83–272, 1933.

[63] J. R. Penning and F. H. Schmidt. Radioactive decay of Ne^{23}. *Phys. Rev*, 105:647–651, 1957.

[64] L. E. Piilonen. *A Measurement of the Beta Spectrum of ^{19}Ne to search for heavy neutrino mixing and to test the Conserved Vector Current hypothesis.* PhD thesis, Princeton University, 1984.

[65] F. L. Riffle, J. D. Goss, D. R. Parsignault, and J. C. Harris. Measurement of the absolute total cross section for the reaction ^{19}F(p,n)^{19}Ne. *Nucl. Phys. A*, 115:120–128, 1968.

[66] S. Ritt, K. Olchanski, and P. Amaudruz. Maximum Integration Data Acquisition System. MIDAS version 2.0.0 rev. 4446, 2009.

[67] B. M. Rustad and S. L. Ruby. Correlation between electron and recoil nucleus in He^6 decay. *Phys. Rev.*, 89:880–881, 1953.

[68] E. R. J. Saettler, F. P. Calaprice, A. L. Hallin, and M. M. Lowry. Beta asymmetry of the first forbidden $\frac{1}{2}^+ \rightarrow \frac{1}{2}^-$ transition in ^{19}Ne and its relationship to the parity nonconserving nucleon-nucleon interaction. *Phys. Rev. C*, 48:3069–3077, 1993.

[69] J. E. Schewe, P. A. Voytas, and P. A. Quin. Measurement of the polarization-asymmetry correlation for ^{21}Na with novel target and polarimeter. *Nucl. Inst. Meth. Phys. Res. A*, 390:274–278, 1997.

[70] D. F. Schreiber. *The beta asymmetry of ^{19}Ne: An experimental test for second-class currents.* PhD thesis, Princeton University, 1983.

[71] G. Senjanovic and R. N. Mohapatra. Exact left-right symmetry and spontaneous violation of parity. *Phys. Rev. D*, 12:1502–1505, 1975.

[72] N. Severijns, M. Allet, K. Bodek, B. A. Brown, J. Camps, P. De Moor, J. Deutsch, M. Ferro-Luzzi, F. Gimeno-Nogues, J. Govaerts, B. R. Holstein, R. Kirchner, J. Lang, R. Mller, S. Navert, O. Naviliat-Cuncic, T. Otto, I. Pepe, R. Prieels, P. A. Quin, P. Schuurmans, J. Sromicki, E. Stephan, E. Thomas, A. Van Geert, L. Vanneste, B. Vereecke, and J. Zejma. Helicity structure in low- and intermediate-energy weak interaction. *Nucl. Phys. A*, 629:423–432, 1998.

[73] N. Severijns, M. Beck, and O. Naviliat-Cuncic. Tests of the standard electroweak model in nuclear beta decay. *Rev. Mod. Phys.*, 78:991–1040, 2006.

[74] N. Severijns, M. Tandecki, T. Phalet, and I. S. Towner. $\mathcal{F}$t values of the $T = \frac{1}{2}$ mirror β transitions. *Phys. Rev. C*, 78:055501, 2008.

[75] R. Sherr and J. Gerhart. Experimental evidence for the Fermi interaction in the β decay of O^{14} and C^{10}. *Phy. Rev.*, 91:909, 1953.

[76] R. Sherr, H. R. Muether, and M. White. Radioactivity of C^{10} and O^{14}. *Phy. Rev.*, 75:282–292, 1949.

[77] E. C. G. Sudarshan and R. E. Marshak. Chirality invariance and the universal Fermi interaction. *Phys. Rev.*, 109:1860–1862, 1958.

[78] O. B. Tarasov and D. Bazin. LISE++: Radioactive beam production with in-flight separators. *Nucl. Inst. Meth. B*, 266:4657–4664, 2008.

[79] E. Thomas, R. Prieels, M. Allet, K. Bodek, J. Camps, J. Deutsch, F. Gimeno-Nogues, J. Govaerts, J. Lang, O. Naviliat-Cuncic, I. Pepe, P. Quin, N. Severijns, and J. Sromicki. Positron polarization in the decay of polarized ^{12}N: a precision test of the Standard Model. *Nucl. Phys. A*, 694:559–589, 2001.

[80] I. S. Towner and J. C. Hardy. The evaluation of V_{ud}, experiment and theory. *J. Phys. G*, 29:197, 2003.

[81] I. S. Towner and J. C. Hardy. The evaluation of $V_u d$ and its impact on the unitarity of the cabibbo-kobayashi-maskawa quark-mixing matrix. *Rep. Prog. Phys.*, 73:046301, 2010.

[82] E. Traykov, A. Rogachevskiy, M. Bosswell, U. Dammalapati, P. Dendooven, O. C. Dermois, K. Jungmann, C. J. G. Onderwater, M. Sohani, L. Willmann, H. W. Wilschut, and A. R. Young. Production of radioactive nuclides in inverse reaction kinematics. *Nucl. Inst. Meth. Phys. Res. A*, 572:580–584, 2007.

[83] T. M. Vitale. A new measurement of the half-life of ^{19}Ne. Undergraduate Thesis, 1977.

[84] S. Weinberg. Charge symmetry of weak interactions. *Phys. Rev.*, 112:1375–1379, 1958.

[85] D. H. Wilkinson and D. E. Alburger. Half-lives of ^{6}He, ^{19}Ne, and $^{42}Sc^{m}$. *Phys. Rev. C*, 10:1993–1995, 1974.

[86] C. S. Wu, E. Ambler, R. W. Hayward, D. D. Hoppes, and R. P. Hudson. Experimental test of parity conservation in beta decay. *Phys. Rev.*, 105:1413–1415, 1957.

[87] J. F. Ziegler, J. P. Biersack, and M. D. Ziegler. The stopping and range of ions in matter. SRIM version 2010.01, 2010.

[88] G. Zweig. An SU_3 model for strong interaction symmetry and its breaking. CERN-TH-401/CERN-TH-412, 1964.

Biography

Leah Jacklyn Broussard was born in Kaplan, Louisiana on June 3, 1982. She graduated Magna Cum Laude from Tulane University with a bachelor of science in computer science, and with majors in math and physics, in May 2004. She went on to earn a Master in the Art of physics from Duke University in 2007 for her work on the development of the experiment to measure the lifetime of ^{19}Ne, and finally a Ph.D. in 2012 for the high precision measurement. During her tenure at Duke, she also contributed significantly to the development, data-taking, and online analysis of the UCNA experiment in Los Alamos, New Mexico, which has produced a very precise measurement of the beta asymmetry in neutron-decay using ultra-cold neutrons. In addition, she held a leading role in the development of the UCNB experiment, which will attempt a precision measurement of the neutrino asymmetry in neutron-decay.